M.Sc. Thesis

Dielectric Loss Measurements at Sub-K Temperatures and Terahertz Frequencies

K. Kouwenhoven

Delft University of Technology

M.Sc. Thesis

Dielectric Loss Measurements at Sub-K Temperatures and Terahertz Frequencies

by

K. Kouwenhoven

to obtain the degree of Master of Science
at the Delft University of Technology,
to be defended publicly on Thursday August 15, 2019 at 10:00 AM.

Student number:	4222849	
Project duration:	November 12, 2018 – July 18, 2019	
Thesis committee:	prof. dr. ir. J.J.A Baselmans,	TU Delft, supervisor
	dr. A. Endo,	TU Delft
	dr. ir. S. Vollebregt,	TU Delft

TU Delft

Abstract

On-chip spectrometers, such as DESHIMA and SuperSpec, require transmission lines with very low loss of $\tan\delta < 10^{-4}$ to achieve sufficient system efficiency. Transmission lines with higher loss would introduce too much signal attenuation in the line from antenna to filter and in the filters themselves. Data regarding the losses of transmission lines at THz frequencies and sub-K temperatures is severely lacking. In this report an on-chip Fabry-Pérot resonator concept is demonstrated that can be used to measure the losses of a transmission line with high sensitivity at high frequencies. To create the in-line Fabry-Pérot resonator, a transmission line of certain length is coupled to a THz source via a twin-slot lens antenna on one side and to an Al-NbTiN hybrid MKID on the other side.

The goal of this work is to measure the losses of microstrip lines at frequencies $>$ 300 GHz, at a temperature of about 250 mK, with dielectric dominated loss in the range of $10^{-3} > \tan\delta > 10^{-5}$. There are several experimental challenges for measuring $\tan\delta$. The first challenge is the limited frequency resolution of the source, due to which resolving low $\tan\delta$ can become impossible. Secondly it was experimentally found that there is stray light coupled to the detector which causes a spurious response with a level of -30dB with respect to the peak (unity) transmission of the Fabry-Pérot resonator. Taking these experimental challenges into account results in a Fabry-Pérot resonator design where the length, the mode number, and the coupler quality factor Q_c of the resonator are optimized. Furthermore multiple resonators on a single chip are used, each coupled to a separate antenna and detector, with different Q_c values. This design method is applicable for different dielectric materials and different transmission line configurations. Using this method a chip was designed and fabricated for a microstrip line based Fabry-Pérot resonator fabricated from sputter deposited superconducting NbTiN metal and a PECVD deposited a-Si layer. Using this chip a $\tan\delta \approx 10^{-4}$ @ 350 GHz was measured, which represents the lowest loss values of a microstrip line at frequencies $>$ 10 GHz ever measured.

Acknowledgements

I would like to thank my great supervisor Jochem Baselmans. I'm grateful that I got the to do my master's thesis under your supervision and I'm looking forward to working with you during the coming years. I have learned a lot from you the past year. I'm especially grateful that you gave me the opportunity to visit a scientific conference during my master's thesis.

I want to thank Akira Endo for his passion when it comes to experimental astronomy. Your article in Maxwell, presentations on DESHIMA, and course on Terahertz astronomical instrumentation inspired me to pick the Experimental Astronomy group for my master's thesis.

I want to especially thank Sebastian Hähnle, my daily supervisor. I've learned a lot from you the past year and I'm grateful that you took the time to explain the intricate details of the MKIDs, the measurement set-up, and the cryostats. You were always available for questions and motivated me to get the best out of this project. You're the best supervisor one could wish for!

I want to thank Kenichi Karatsu, Juan Bueno, and David Thoen for all the support you've given me during the measurements of my chips. I've learned a lot from all of you when it comes to the measurement set-up and the cryostat system.

I want to thank Cyrus and Sander, for mercilessly criticizing my work, presentation slides, and conference poster. The quality of my work improved thanks to you. Furthermore I want to thank you, and all other students in our track, for all the fun we had during the master's programme the last two years. I look forward to working alongside you the coming years, Sander. To Cyrus, the best of luck in Rennes!

I'm grateful that I got to spend the last year in the Terahertz Sensing group. I really enjoyed the lunches, coffee breaks, Christmas dinner, and group outing.

Last but not least I want to thank the people closest to me: Karlijn, my family, and my friends. You've made sure that I spent enough time on activities besides my master's thesis. I want to thank you all for the support you've given me during my bachelor's and master's. I would not have gotten this far without you.

K. Kouwenhoven
Delft, July 2019

Contents

1 Introduction 1
- 1.1 Terahertz astronomy 2
- 1.2 Superconducting astronomical instrumentation and Microwave Kinetic inductance detectors. 4
  - 1.2.1 DESHIMA 4
  - 1.2.2 MOSAIC 5
- 1.3 Problem statement 6
- 1.4 Proposed solution 6
- 1.5 Aim of this project and thesis outline 8

I Theory 9

2 Superconductivity 11
- 2.1 Cooper pairs and quasiparticles 11
- 2.2 Complex conductivity 12

3 Transmission Lines 15
- 3.1 Microstrip 15
- 3.2 Coplanar waveguide 18

4 Half wave in-line resonator 21

5 Q-factors 23
- 5.1 Coupler quality factor Q_c 23
- 5.2 Dissipative losses Q_i 24
  - 5.2.1 Fill fraction 25
- 5.3 Describing resonators by Q-factors 26

6 Microwave Kinetic Inductance Detector (MKID) 27
- 6.1 Response 28
- 6.2 Hybrid MKID 29

II Experimental overview 31

7 Experiment description 33
- 7.1 Dielectric loss tangent experiments 33
- 7.2 Experimental concept 33
  - 7.2.1 Terahertz source 34
  - 7.2.2 Beam splitter 34
  - 7.2.3 Cryostat 34
  - 7.2.4 Chip 34
  - 7.2.5 Lens antenna 34
  - 7.2.6 Polariser grid 35
  - 7.2.7 Resonator 35
  - 7.2.8 KIDs 35
- 7.3 Spurious response 36
- 7.4 Two lens set-up 36
- 7.5 Measuring Q_i 38
  - 7.5.1 Q_i limited approach 38
  - 7.5.2 Ql(Qc,Qi) curve approach 39
  - 7.5.3 Full $|S_{21}|$ curve approach 40

8 Detailed design **43**
8.1 Design space 43
8.2 Couplers 45
8.2.1 Designed vs. fabricated coupler 46
8.3 Design of the polyimide chip 47
8.4 Design of the amorphous silicon chip 49
8.5 Fabrication 52

III Measurements **55**

9 Polyimide proof of concept measurements **57**
9.1 Chip overview. 57
9.2 Data 57
9.3 Analysis 59
9.4 Secondary resonances. 61
9.5 Conclusion 63

10 a-Si measurements **65**
10.1 Chip overview. 65
10.1.1 DC chip 66
10.1.2 SEM results 66
10.1.3 Corrected overview 67
10.2 Analysis 67
10.2.1 Raw response 67
10.2.2 Corrected response 68
10.2.3 Individual peaks 69
10.2.4 Q values 70
10.2.5 Averaged Q_i values. 72
10.2.6 $Q_l(Q_c,Q_i)$ curve 73
10.2.7 Full curve 73
10.3 Results and discussion. 74

11 Conclusion **75**

12 Recommendations **77**
12.1 Oscillation in FP peak height. 77
12.2 Spurious response floor 77
12.3 Chip improvements. 77

References **79**

A The scattering (S) matrix **85**

B The transmission (ABCD) matrix **87**

C Conversion between S and ABCD parameters **89**

D Unmeasured devices **91**
D.1 PI chip design for Q_c = 20,000. 91
D.2 Amorphous silicon chip design for 650 and 850 GHz. 91

List of Figures

1.1 A brief history of the telescope. **a)** the first gigantic telescope, built by Herschel. It was completed in 1789. Image from [1]. **b)** The first radio telescope, built by Bell Telephone Laboratories engineer Karl Guthe Jansky. This array of dipoles was built to find the source of static interference present in radio and telephone services. Image from [2]. **c)** The first parabolic dish radio telescope built by Grote Reber in his backyard in Illinois. Image from [3]. 1
1.2 Excluding the radiation CMB, the universe is filled with radiation from galaxies. A significantly large fraction of this radiated power lies in the terahertz (THz) frequency band. CIB stands for the Cosmic Infrared background and COB for the Cosmic Optical Background. Adapted from [4]. 2
1.3 The Andromeda galaxy (M31) in optical, infrared (orange) and X-ray (blue) with the resulting composite image. The infrared image is obtained from data of the SPIRE and PACS instruments on the Herschel space observatory. Image from [5]. 3
1.4 Hubble space telescope image of ”dusty” galaxy Arp 220. The dust (red) in this galaxy obscures part of the visible-light radiated by Arp 220. Arp 220 is defined as an Ultraluminous Infrared Galaxy (ULIRG). Image from [6]. 3
1.5 The galaxy redshift survey. The axis from the centre show the the redshift z, and the distance from us. This axis is also time since it indicates how long ago a galaxy existed, i.e. how long ago the signal arriving on earth was transmitted. Note that there is a change in the distribution of galaxies visible when looking inwards. Image from [7]. 4
1.6 An overview of the proposed MOSAIC instrument. The instrument consists of multiple stacked spectrometers each realising a pixel on the sky. MOSAIC is capable to create a 2D image and resolve the redshift of all sourced in this 2D image. The result is a 3D image of the night sky. Image from [8] 5
1.7 Structure of a flat-plate Fabry-Pérot resonant cavity. Image from [9]. 7
1.8 Example of the expected Fabry-Pérot interferometer response. Each resonance peak gives a measurement of the dielectric losses. How the dielectric losses are obtained from the resonance peaks is explained in chapter 5. 7

2.1 lattice distortion creating a region of positive charge. 11
2.2 The quasiparticle n_qp density in a superconductor as a function of the temperature T. T_c is the critical temperature of the superconductor. The quasipartcicle density n_qp drops rapidly for temperatures below the critical temperatures T_c of the superconductor. 12
2.3 Superconducting film modelled as a resistive component (σ_1) and an inductive component (σ_2). 12

3.1 Two port reperesentation of a transmission line section 15
3.2 Microstrip geometry: h is the height of the dielectric, W is the width of the microstrip line and t is the thickness of the line. **(inset)** Electric field distribution of a microstrip transmission line, note the ’fringing fields’ at the edges of the strip. 15
3.3 CPW geometry: S is the width of the central conductor, G is the gap between the central conductor and the ground plane on both sides and t is the thickness of the film. **(inset)** Electric field distribution for **a)** the differential mode and **b)** the common mode. 18

4.1 In line resonator. The resonator section of the transmission line is described by it’s length (l), characteristic impedance (Z_0) and complex propagation constant (γ). The couplers are modelled as in-line capacitors with capacitance C_k. 21

4.2 First two modes $n = 1$ and $n = 2$ for an open-open half wave resonator. The end points of the line at $z = 0$ and $z = l$ are voltage anti-nodes, at which point the amplitude of the voltage standing wave in the resonator is maximum. 22

4.3 Example of a resonator curve using the model of Fig. 4.1 and (4.4) and (4.7). 22

5.1 Each of the resonance peaks in the transmission curve of an in-line resonator has a lorentzian shape. The lorentzian shape is defined by the resonance frequency f_0 and the $3dB$ bandwidth BW_{-3dB}. The loaded Q factor Q_l of the resonator is then given by f_0/BW_{-3dB}. 25

6.1 A quarter wave resonator coupled to the readout line (top). In this case the resonator and readout line are created using CPW lines. 27

6.2 The MKIDs response to different quasiparticle densities n_{qp}. For higher quasiparticle densities the resonance frequency ω_0 shifts to lower frequencies and the dip depth $|S_{21,min}|$ decreases. 29

6.3 Hybrid MKID with in blue aluminium and in green NbTiN. The thin aluminium section is shorted at one end and connects to the wide NbTiN section at the other end. 29

7.1 Simplified view of the experimental set-up. Power from the toptica source is coupled to the antenna of the chip trough a beam splitter, the filter stack, and the polariser grid to the chip inside the cryostat. The beam splitter **(1)** reduces the power transmitted into the cryostat, the power not transmitted into the cryostat is absorbed in the absorber. The filter stack **(2)** at the opening of the cryostat creates a bandpass filter. The polariser grid **(3)**, located at the outside of the vacuum window, allows transmission of one polarisation and rejects the other polarisation. The chip is placed in the 120 mK stage of the cryostat. 34

7.2 Simplified version of the resonator chip. The grey area indicate the contact area with the chip holder. The dotted lines indicate the lenses placed on the twin slot antennas. The broadband KIDs are not shown in this figure but would be positioned on the blue terahertz line just before the start of the FP resonator. 35

7.3 Graphical representation of the spurious response contribution. Part of the power arriving at the chip is not coupled to the antenna but travels along the chip as stray light which can be absorbed in the MKID line giving rise to the spurious response of the MKID. . . . 36

7.4 Simplified view of the two lens set-up. The opening angle of the cryostat θ_o is determined by the size of the aperture at the 50K stage. The two lenses create a collimated beam increasing the coupling efficiency between the toptica source and the twin slot lens antenna on the chip. 37

7.5 The farfield patterns in E-plane and H-plane for the twin slot lens antenna configuration. The pattern is given for the 350GHz and the 650 GHz design. The pattern is given in the farfield of the lens-antenna system. 37

7.6 Polyimide microstrip resonator (7 mm) with $Q_c = 2000$ couplers. 38

7.7 Q_l vs. Q_c for different values of Q_i. Three curves are shown for $Q_i = 10^3$, $Q_i = 10^4$ and $Q_i = 10^5$. note that, for $Q_i = 10^3$, $Q_l \approx Q_i$ for high values of Q_c i.e. $Q_c \gg Q_i$. 39

7.8 Example of the spurious response dominated resonator curve. The spurious response limit is estimated around at $-30dB$. As the resonance peaks drop below $-30dB$ the response of the kid is dominated by the spurious response in the system instead of the direct response from the FP resonator. 40

7.9 $|S_{21}|$ resonator curve using the model of Fig. 4.1, and (4.4) together with $|S_{21,min}|$ from (7.7). 41

7.10 Two different resonators with different resonator lengths l_{res} but equal Q_c. The shorter resonator, $l_{res} = 3mm$, requires a lower C_k to obtain the same Q_c since the mode numbers of the peaks are lower compared to the longer resonator (5.6). The lower C_k results in a lower minimum transmission $S_{21,min}$ (7.5). 42

8.1 Example of the change in $|S_{21}|$. **(a)** Increase in Q_c by decreasing the capacitance in the model of Fig. 4.1. The decrease in Q_c decreases $|S_{21,max}|$ and, since C_k decreases, $|S_{21,min}|$ **(b)** As the length of the resonator decreases the frequency spacing of the peaks f_0 increases. As discussed in table 8.1 this decreases Q_c which is visible in the slightly wider peak for the $l = 2mm$ resonator. 44

8.2 CPW to CPW coupler. Metal is indicated in blue. The coupling strength can be varied by changing l_1 and l_2. 45

8.3 microstrip coupler. CPW layer is indicated in blue, microstrip layer in red and dielectric layer in yellow. The coupling strength can be varied by changing the overlap between the two lines ($l_overlap$). 45

8.4 Effect of the microstrip width on $|S_{21}|$. w is the width of th overlapping micorstrip, S the width of the CPW central line and G the width of the CPW gaps. At $s = W$ the microstrip and the CPW central line have the same width, for $w = S + G$ the microstrip extends halfway unto the gaps of the CPW and for $w > S + 2G$ the microstrip extend unto the ground planes of the CPW. The figure shown is for 350 GHz, $S = 2\mu m$, $G = 2\mu m$ and a $1\mu m$ thick dielectric 46

8.5 Expected Resonance curves for the 300-400 GHz polyimide FP resonators. Note that the pure CPW line, which does not include any polyimide in the line geometry, is excluded in this figure since the Q_i of this resonator is not determined by the dielectric losses. . . 48

8.6 The selected Q_c values for the microstrip resonators. The lowest Q_c value is selected such that the difference between the curves can be resolved. The highest Q_c is selected as 30.000 49

8.7 Resonance curves for the 300-400 GHz microstrip FP resonator. 51

8.8 Fabrication process referred to as the ”normal” approach. In this fabrication process the NbTiN microstrip line is deposited on top of the a-Si layer. A protection layer is used to protect the NbTiN ground plane during the NbTiN line etching step. This fabrication process is similar to the current process plan for the DESHIMA 2.0 chips, one of the project which requires the high Q_i dielectrics. 52

8.9 Fabrication process referred to as the ”inverted” approach. In this case the NbTiN microstrip line is buried beneath the a-Si dielectric layer and the NbTiN ground plane is deposited on top of the a-Si layer. This process flow removes the need for a protection layer during the last NbTiN etching step since the microstrip line is completely covered by the dielectric layer. 53

9.1 Measured response for the $Q_c = 2000$ polyimide chip. **top)** The response for all four FP KIDs. **bottom)** The response normalised to the response of the blind KID. The numbering in the legend of this figure corresponds to the numbering in table 9.1. 58

9.2 Corrected response of FP KID 1. This KID is connected to the bare CPW FP resonator which does not contain any polyimide. The couplers for this chip are designed for $Q_c = 2000$. 59

9.3 Corrected response of FP KID 2. This KID is connected to the CPW covered with polyimide FP resonator. The couplers for this chip are designed for $Q_c = 2000$. 60

9.4 Corrected response of FP 4. This KID is connected to a 3mm long microstrip FP resonator. The couplers for this chip are designed for $Q_c = 2000$. Note that the fit in this plot focusses on the primary peak in the presence of the additional response. 61

9.5 The influence of the secondary resonance on the FP resonance peaks can be modelled trough the ABCD matrix approach by including an extra section of transmission line before the first FP Coupler, see 9.5a. Filtering the secondary resonance from the signal reduces the effect the secondary resonance has on the FP resonance peaks but the resulting peaks still differ from the real FP peaks, see Fig. 9.5b. Note that this approach is not a realistic approach since it requires a-priori knowledge on the exact FP curve. . . 62

10.1 Image from the a-Si chip fabricated using the inverted process from Fig. 8.9. Craters are clearly visible in the a-Si layer around the meandering NbTiN microstrip line. 66

10.2 The raw response of the four FP KIDs and the blind KID. For the a-Si experiment the measured frequency range is 320 GHz to 380 GHz with a resolution of 10 MHz. The chip is cooled to 40 mK. 67
10.3 Overview of the response of all four FP KIDs normalised to the response of the blind KID. The minimum and maximum mode number are given in table 10.4 68
10.4 A single FP resonance peak in the response of FP 0 analysed over seven measurement runs with identical measurement settings. The peaks show small deviations between the different measurements. 69
10.5 An overview of Lorentzian fits of the FP peaks in the response of the FP KIDS. FP naming is consistent with table 10.3. **(a)** Good Lorentzian fit of FP 0. **(b)** Bad lorentzian fit of FP 0 due to the asymmetrical nature of the FP peak. 69
10.6 Mean fitted $Q_l(f)$ with standard deviation over seven measurement for each peak. The values of Q_l are plotted against the resonance frequency f_n of the corresponding peaks. A linear fit through Q_l is plotted to show the trend in Q_l vs. frequency. As expected from the simulated Q_c of the coupler and assuming a Q_i constant over frequency, Q_l of the peaks decreases with frequency. The linear fit of Q_l is a first order check and does not represent an assumption on the actual frequency behaviour of Q_l. 70
10.7 The fitted Q_l values for the FP peaks in the response of FP 3. There is a clear correlation between the change in peak height and the change in fitted Q_l value, i.e. when the peak height peaks the fitted Q_l values of that peak drops. This indicated that the additional resonance, the source of the change in peak height, affects the fitted Q_l values. The dotted line is plotted to make the frequency behaviour of the fitted Q_l clearer. 71
10.8 Using the simulated S_{21} of the couplers and the mode number of the FP peaks of each resonator, the frequency dependent $Q_c(f)$ of each FP resonator can be estimated. The difference in Q_c between the different FP resonators is due to the difference in frequency spacing f_n and thus mode numbers of each FP resonator. The $Q_c(f)$ value is an estimate since the radiation losses of the coupler (section 5.2) and the exact film parameters at the coupler are unknown. 71
10.9 Mean $Q_i(f)$ calculated from the fitted $Q_l(f)$ values of Fig. 10.6 and the corrected Q_c 10.8 for all three FP resonators. The given Q_i values include the fill factor and are thus the Q_i values of the dielectric material and not of the transmission line (section 5.2). The linear fit of Q_i is a first order check and does not represent an assumption on the actual frequency behaviour of Q_i. 72
10.10 Plotted Q_l vs. Q_c for different values of Q_i. For each resonator the averaged fitted Q_l of each peak averaged over multiple measurements is plotted against the expected Q_c value of that peak. The averaged Q_l is taken over the peaks in the frequency range from 320 GHz to 380 GHz for FP 0 and FP 1 and 320 GHz to 380 GHz for FP 3. Note that the given Q_i is of the dielectric, taking the fill factor of the microstrip geometry, 67.7%, into account. 73
10.11 The response of KID 0 together with the modelled FP response. The FP response is modelled for the expected Q_c of 1660 at 350 GHz and the averaged Q_i of 2355. 73

A.1 Representation of the scattering parameters. 85

B.1 **a)** A two-port network. **b)** A cascade connection of two-port networks. 87

D.1 Resonance curves for the 600-700 GHz microstrip FP resonator. 92
D.2 Resonance curves for the 800-900 GHz microstrip FP resonator. 93

List of Tables

7.1 Overview of the expected dielectric Q_i factors and the measurement frequencies. 33

7.2 Aperture sizes for the first null and the $-3dB$ point of the lens antenna pattern. The angle θ is with respect to 0, see Fig. 7.4 and 7.5. d is the diameter of the required aperture in mm. 37

8.1 Design space. The coupling quality factor Q_c can be changed by changing the mode number trough the resonator length l_{res}, or by changing the capacitance of the coupler C_k. 44

8.2 Selected resonator lengths for all three resonator types: the Bare CPW, the CPW covered with a polyimide dielectric layer and the microstrip with a polyimide dielectric. . . . 47

8.3 Overview of the CPW FP and coupler parameters for the bare CPW and the CPW covered with a ployimide (PI) layer. Coupler dimensions are given as in Fig. 8.2. 47

8.4 Overview of the CPW to microstrip coupler geometries. Coupler dimensions are given as in Fig. 8.3. 47

8.5 Overview of the expected a-Si dielectric Q_i factor and the measurement frequencies. . . 49

8.6 Overview of the a-Si FP resonator transmission line properties. The a-Si layer is 250 nm thick, the micorstrip is 2 µm wide and the CPW is 2-2-2 µm. 50

8.7 Overview of the microstrip FP resonator design for the a-Si experiment. Each frequency band f is a different chip with four resonators. Coupler dimensions are given as in Fig. 8.3. 50

9.1 Overview of the FP resonators on the $Q_c = 2000$ polyimide chip. Together with these 4 FP KIDs the chip contains 4 broadband KIDs, a blind KID and a pure NbTiN KID. Fill factor is as defined in section 5.2 57

9.2 Overview of the results of polyimide chip. The Q_l and Q_i factors are given as a mean with a standard deviation, this mean is taken over the fitted Q_l of multiple peaks within the frequency window of 330 GHz to 365 GHz. The simulated Q_c uses the DC and SEM measurements to model the coupler as accurately as possible. The designed Q_c for this chip is 2000. The fill fraction (FF) is obtained as discussed in section 5.2. 60

10.1 Overview of the designed FP resonators for the a-Si chip as presented in section 8.4. The chip contains four identical microstrip FP resonators and a blind KID. The couplers used for all four FP resonators are identical, the only difference between the resonators is the length $l_{resonator}$ 65

10.2 Results of the a-Si DC chip. This chip contains several simple lines created in the different layers present on the chip. The superconducting properties of the different layers, such as the critical temperature T_c and the sheet resistance R_s can be measured. Using the measured film properties an accurate estimation of the kinetics inductance L_k can be made. The DC chips are measured in a adiabatic demagnetization refrigerator (ADR) cryostat at SRON Utrecht. The NbTiN GND (a-Si) layer has the a-Si layer on top and the NbTiN line layer (a-Si) has the a-Si layer below. 66

10.3 Corrected overview of the Q_c and frequency spacing f_n for the a-Si microstrip FP resonators and their corresponding KID ID. The given Q_c values are for the centre frequency of the band $f = 350GHz$. 67

10.4 The corrected expected frequency spacing $f_{corrected}$ vs. the observed frequency spacing $f_{observed}$. The minimum n_{min} and maximum n_{mode} mode number of the peaks between 320 GHz and 380 GHz is given. 68

10.5 The weighted average Q_i, first for each FP assuming constant frequency behaviour (Fig. 10.9) and second over all three FP KIDs. The average is weighted with the error bars of Fig. 10.9 72

B.1 ABCD of commonly used two-port circuits. $\gamma = \alpha + j\beta$ 88

C.1 Conversion between ABCD and S parameters. $\mathbf{Z_{01}}$ is the impedance of the source. $\mathbf{Z_{02}}$ is the impedance of the load. 89

D.1 Overview of the CPW FP and coupler parameters for the bare CPW and the CPW covered with a ployimide (PI) layer. Coupler dimensions are given as in Fig. 8.2. 91
D.2 Overview of the CPW to microstrip coupler geometries . Coupler dimensions are given as in Fig. 8.3. 91
D.3 Overview of the microstrip FP resonator design for the a-Si experiment. Each frequency band f is a different chip with four resonators. Coupler dimensions are given as in Fig. 8.3. 91

1

Introduction

In 1608 German-Dutch lens maker Hans Lippershey patented the first refractive telescope, although he referred to it as a 'Dutch perspective glass'. This telescope consisted of two lenses and reached a magnification of up to three times. In 1610 Galileo was the first to use the 'Dutch perspective glass' for astronomical purposes and with it discovered the four largest moons of Jupiter: IO, Ganymede, Callisto, and Europa. The term telescope was coined in 1611 by Greek mathematician Giocanni Demisiani.

Dutch astronomer Christian Huygens, inspired by Galileo, greatly improved the performance of the optical telescope. In 1655 he built a 12 foot (3.7 meters) telescope with which he made detailed observations of Saturn. In 1688 Sir Isaac Newton built the first reflecting telescope using mirrors instead of lenses. Newton's mirror based telescope had a number of advantages over the existing lens based telescopes, it was cheaper and simpler to build, it was more compact, it had a wider field of view, and it did not suffer from chromatic aberration. In 1789 William Herschel build the first gigantic telescope. The gigantic telescope was based on newtons reflecting telescope and had a length of 40 foot (12 meters).

In 1933 Bell Telephone Laboratories engineer Karl Guthe Jansky built the first radio telescope. Jansky's telescope, or "merry-go-round", had a diameter of 30 meters. Where the previous telescopes where all designed for optical signals Jansky's telescope was designed to receive a signal of around 20.5 MHz. His goal was to find the source of static interference in radio and telephone services. Using his "merry-go-round" he found a curious constant background "faint hiss". Jansky correctly suspected that this signal originated not from earth but from outside the solar system.

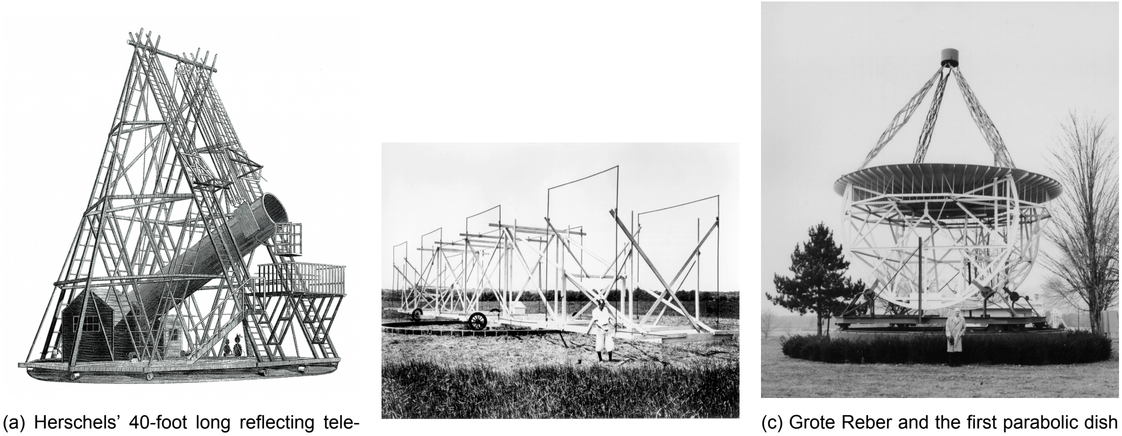

(a) Herschels' 40-foot long reflecting telescope (1789).

(b) Jansky's merry-go-round (1933).

(c) Grote Reber and the first parabolic dish telescope (1937).

Fig. 1.1: A brief history of the telescope. **a)** the first gigantic telescope, built by Herschel. It was completed in 1789. Image from [1]. **b)** The first radio telescope, built by Bell Telephone Laboratories engineer Karl Guthe Jansky. This array of dipoles was built to find the source of static interference present in radio and telephone services. Image from [2]. **c)** The first parabolic dish radio telescope built by Grote Reber in his backyard in Illinois. Image from [3].

Inspired by Jansky's work, amateur radio enthusiast Grote Reber built the first parabolic dish telescope in his backyard in Illinois in 1937. The telescope had a dish with a diameter of 9 meters and served as the only radio telescope in the world until after World War II. Repeating Jansky's work he identified the Milky Way as the first astronomical radio source. Reber's telescope and research was the beginning of the research field known as radio astronomy.

Since Reber's work the sky has been observed at a huge range of frequencies, ranging from radio frequencies of a few MHz up to gamma rays with ground breaking observatories such as LOFAR and ALMA. Still there remains one largely unexplored frequency band at the boundary between optical and radio astronomy, the Terahertz frequency range.

1.1. Terahertz astronomy

The terahertz (THz) frequency range, taking the widest definition, ranges from 0.1-10 THz. Above 1 THz this frequency band is often referred to as Far Infrared (FIR). Although the THz frequency band contains a significant part of the radiation from galaxies (Fig. 1.2) it has remained largely unexplored.

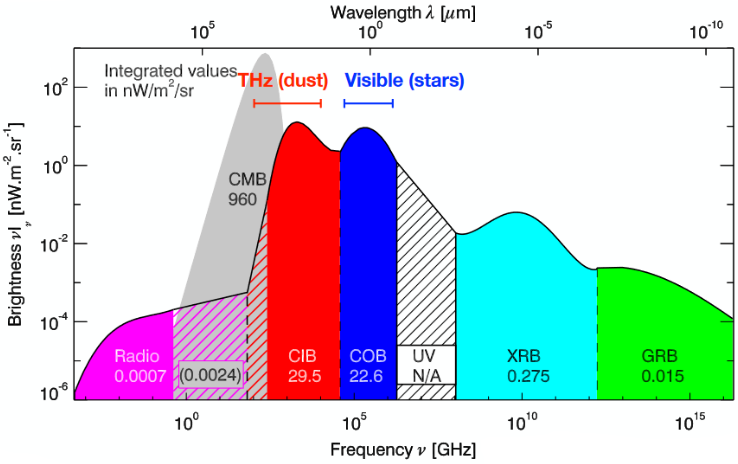

Fig. 1.2: Excluding the radiation CMB, the universe is filled with radiation from galaxies. A significantly large fraction of this radiated power lies in the terahertz (THz) frequency band. CIB stands for the Cosmic Infrared background and COB for the Cosmic Optical Background. Adapted from [4].

This frequency band remained unexplored since it was assumed that the sources visible in the THz/FIR band are the same sources that are visible in the optical regime. It was thus assumed that observations in the THz/FIR band would yield no additional information compared to optical observations. This changed with IRAS (Infrared Astronomical Satellite), which observed from 12 - 100 micron. The infrared observations of the Andromeda galaxy by the SPIRE and PACS instruments on the Herschel space observatory are a good example of how different a galaxy looks at IR wavelengths compared to optical wavelengths. The infrared images from Andromeda are given in Fig. 1.3 together with optical and X-ray observations. These images showed that the infrared radiation from galaxies is not from the hot stars, which completely disappear in the infrared images, but from the dust in the galaxies. This dust is heated by the hot stars and re-emits energy in the THz/FIR frequency range.

The virtue of THz astronomy lies in the observation of "dusty" star forming galaxies in the early universe. these "dusty" galaxies are all but invisible in the optical regime since the dust clouds in the galaxy obscures the stars, but appear very bright in the THz frequency due to the thermal radiation from the heated dust. Terahertz astronomy thus allows astronomers to examine these young and active galaxies. An example of such a "dusty" galaxy is Arp 220 (Fig. 1.4) which appears bright in the THz/IR frequency range.

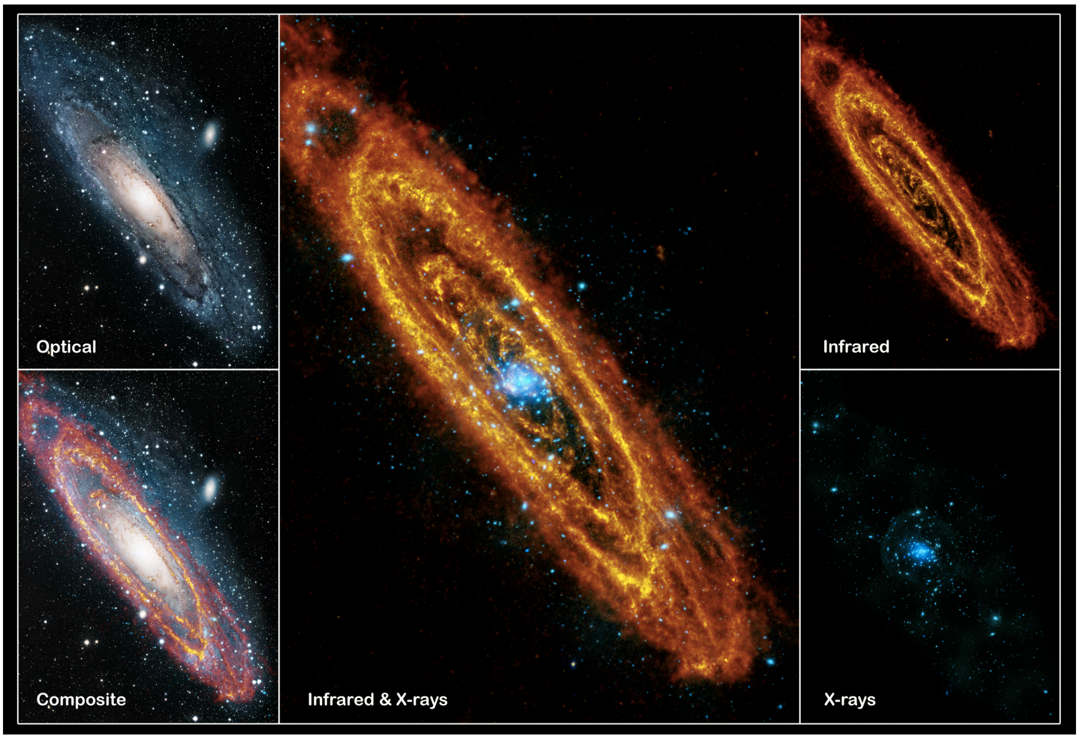

Fig. 1.3: The Andromeda galaxy (M31) in optical, infrared (orange) and X-ray (blue) with the resulting composite image. The infrared image is obtained from data of the SPIRE and PACS instruments on the Herschel space observatory. Image from [5].

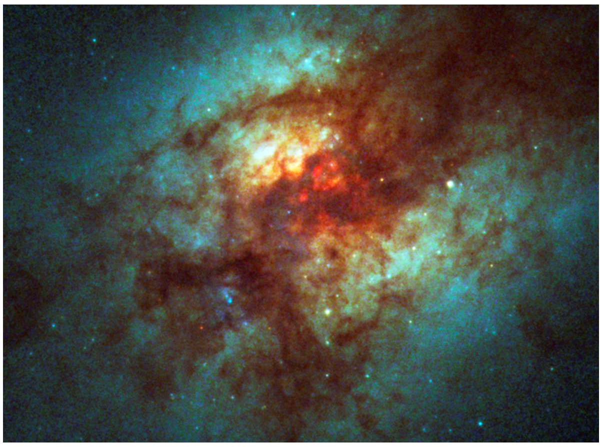

Fig. 1.4: Hubble space telescope image of ”dusty” galaxy Arp 220. The dust (red) in this galaxy obscures part of the visible-light radiated by Arp 220. Arp 220 is defined as an Ultraluminous Infrared Galaxy (ULIRG). Image from [6].

1.2. Superconducting astronomical instrumentation and Microwave Kinetic inductance detectors.

The Herschel space observatory was one of the first space missions to carry superconducting detectors (HIFI) for THz astronomy. These detectors use the principle of superconductivity as discovered by Heike Kamerlingh Onnes in 1911 and they proved to extremely well suited for THz astronomy. A short theoretical introduction on superconductivity is given in chapter 2 of this thesis. There are numerous superconducting THz detector technologies. The heterodyne Superconductor-Insulator-Superconductor (SIS) and Hot Electron Bolometer (HEB), and the direct Transistion Edge Sensors (TES) and Microwave Kinetic Inductance Detectors (MKID). The Terahertz Sensing group works on MKID detectors and two MKID based instruments: The DESHIMA on-chip spectrometer for the Japanese ASTE telescope, and the AMKID camera for the ESO-German APEX telescope, both located in Chile. The group is also working on the successor of DESHIMA: MOSAIC.

1.2.1. DESHIMA

DESHIMA, Deep Spectroscopic High-redshift Mapper, uses the detection of the bright atomic carbon ($[C_{II}]$) line to determine the redshift of a submillimeter (”dusty”) galaxy. The $[C_{II}]$ line has a rest frequency of roughly 1.9 THz, but during the time the signal travels from the distant galaxy to the detector it is redshifted due to the expansion of the universe. The redshift causes the $[C_{II}]$ line to be observed at a different frequency than it’s rest frequency as given by

$$f_{obs} = \frac{f_{rest}}{(1+z)} \tag{1.1}$$

where z is a measure of the redshift in terms of frequency shift. The redshift z is proportional to the distance between us and the observed galaxy, the larger the distance the longer the signal travels in the expanding universe before it reaches us which results in a larger redshift. This information allows one to construct a 3D map of the universe. Furthermore, since the redshift is related to the time the signal has travelled to reach us the redshift is a measure of how long ago the signal was transmitted. This gives the 3D map a time component where an increasing redshift corresponds to an earlier universe. Using this map the evolution of the large scale structure of the universe can be studied. A slice of such a map is given in Fig. 1.5 in which each dot represents a different galaxy with a redshift z.

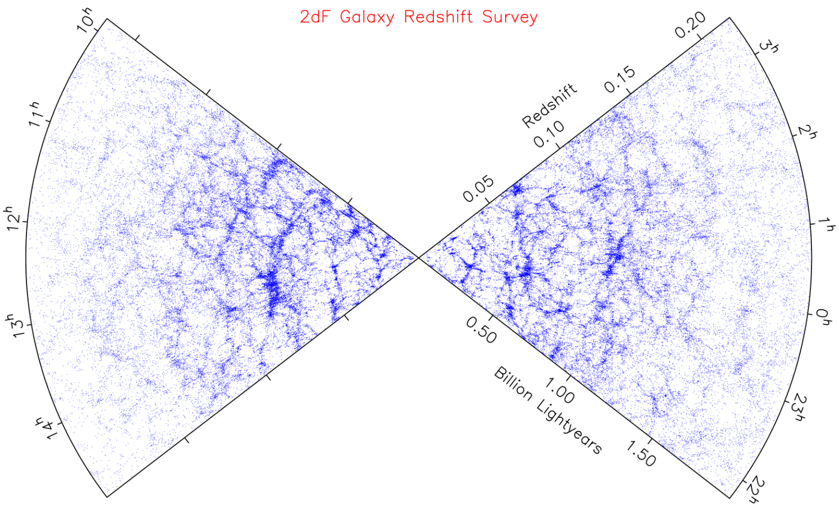

Fig. 1.5: The galaxy redshift survey. The axis from the centre show the the redshift z, and the distance from us. This axis is also time since it indicates how long ago a galaxy existed, i.e. how long ago the signal arriving on earth was transmitted. Note that there is a change in the distribution of galaxies visible when looking inwards. Image from [7].

To measure a large range of redshifts you need an ultra-wideband spectrometer with enough resolution to resolve the emission lines. DESHIMA is the first of this class of spectrometers aiming for a bandwidth from 220 GHz to 440 GHz which corresponds to a redshift z of 7.6 to 3.3 when targeting the $[C_{II}]$ line.

The Deshima spectrometer is created using multiple MKIDs and filters. Each filter, designed for a different frequency, is coupled to a separate MKID. In this way each MKID is sensitive to a different frequency component of the astronomical signal. By reading out and combing all MKIDs the spectrum of the received astronomical signal can be reconstructed. By finding the $[C_{II}]$ line in this reconstructed spectrum the astronomical redshift z can be determined.

1.2.2. MOSAIC

MOSAIC, multi object spectrometer with an array of superconducting integrated circuits, is a proposed upgrade to the DESHIMA instrument. Although DESHIMA is really efficient in resolving the $[C_{II}]$ and thus the depth/distance of the galaxy it is a single pixel instrument and thus not suitable for mapping large sections of the sky. MOSAIC consists of an array of multiple, DESHIMA like, spectrometers effectively realising multiple spectrum resolving pixels. With multiple pixels MOSAIC can create a 2D map of the sky and at the same time, trough the spectrometers, resolve the redshift of each galaxy found in the 2D map creating a 3D map with a single instrument. An example of what the MOSAIC instrument might look like is given in Fig. 1.6.

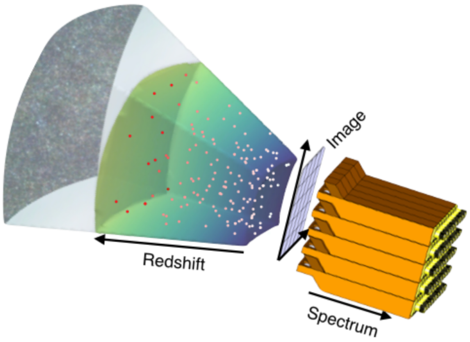

Fig. 1.6: An overview of the proposed MOSAIC instrument. The instrument consists of multiple stacked spectrometers each realising a pixel on the sky. MOSAIC is capable to create a 2D image and resolve the redshift of all sourced in this 2D image. The result is a 3D image of the night sky. Image from [8]

1.3. Problem statement

The instruments described above, DESHIMA and MOSAIC, require low loss transmission lines to achieve sufficient system efficiency. The current version of DESHIMA [10, 11] uses the coplanar waveguide (CPW) geometry for the transmission lines, which can support a common mode. When this common mode is exited in the transmission line, which happens for example at the filters, the power on the line is radiated away from the line instead of transmitted along the line. This causes a huge loss of signal which decreases the system efficiency drastically.

An alternative to the CPW, which does not suffer from the common mode, is the microstrip line. The microstrip line requires a dielectric layer as separation between the signal line and ground plane. This dielectric layer introduces dissipative losses in the transmission line. From [12] DESHIMA requires transmission lines with losses $Q_i > 10^4$ to achieve sufficient system efficiency. Normally this would be impossible due to the ohmic losses in the metal. However for a superconducting metal these losses drop to zero when the metal is cooled to below it's critical temperature. In recent work [13] it is shown that the losses in superconducting coplanar waveguides is limited by radiation loss only and can be as low as Qi > 20.000. Hence, the dominant loss mechanism for microstrip lines is given by the dielectric material. The best losses at GHz frequencies are given by Nb-SiO2 based microstrip lines [14] with $Q_i \; 2000$ at 110 GHz.

The problem is that data regarding the losses of dielectric materials at sub-K temperatures and THz frequencies is severely lacking. The aim of this project is to design a ”lab on chip” platform which can be used to measure the dielectric losses in different dielectric materials. The requirements for this ”lab on chip” are:

- The dielectric loss should be measurable at frequencies ranging from 300 GHz to 1.1 THz.
- Dielectrics with an intrinsic loss quality factor ranging from 100 to 10^5. These values originate from the sparse data that exist for polyimide and amorphous sillicon. The data that is available for these dielectrics is either measured at room temperature, low frequencies or under specific device conditions [15]-[18].
- The dielectric loss should be measured at sub-Kelvin temperatures. DESHIMA and MOSAIC are superconducting detectors which operate at sub-K temperatures, therefore data regarding the dielectric losses are required at sub-K temperatures.
- Suitable for different dielectric materials with different thickness's and different dielectric constants ε_r.

1.4. Proposed solution

The proposed solution is an on-chip Fabry-Pérot (FP) interferometer for which the resonance behaviour depends on the properties of the dielectric material used in the interferometer. The Fabry-Pérot interferometer has a long history in dielectric measurements and has been used, for example, by NASA in 1969 [9]. For these measurements the interferometer is constructed on an optical table with two reflectors in between which a dielectric sample can be placed (Fig. 1.7).

The example given in Fig. 1.7 is suitable for E-band (60 to 90 GHz) at room temperature. For this experiment the Fabry-Pérot interferometer is created on-chip using the same materials and deposition methods as in the DESHIMA and MOSAIC projects. The experiment can be performed with the measurement equipment available in the Terahertz sensing group at the TU Delft.

The expected output of the on-chip Fabry-Pérot interferometer is a resonance curve as given in Fig. 1.8. The shape of each of the peaks in this resonance curve depends on the dielectric losses.

The response of the interferometer is measured using the microwave kinetic inductance detectors, MKIDs, which allow for measurements at sub-Kelvin temperatures and a frequency range of roughly 90 GHz to 1.1 THz. This proposed solution satisfies the requirements as given in section 1.3.

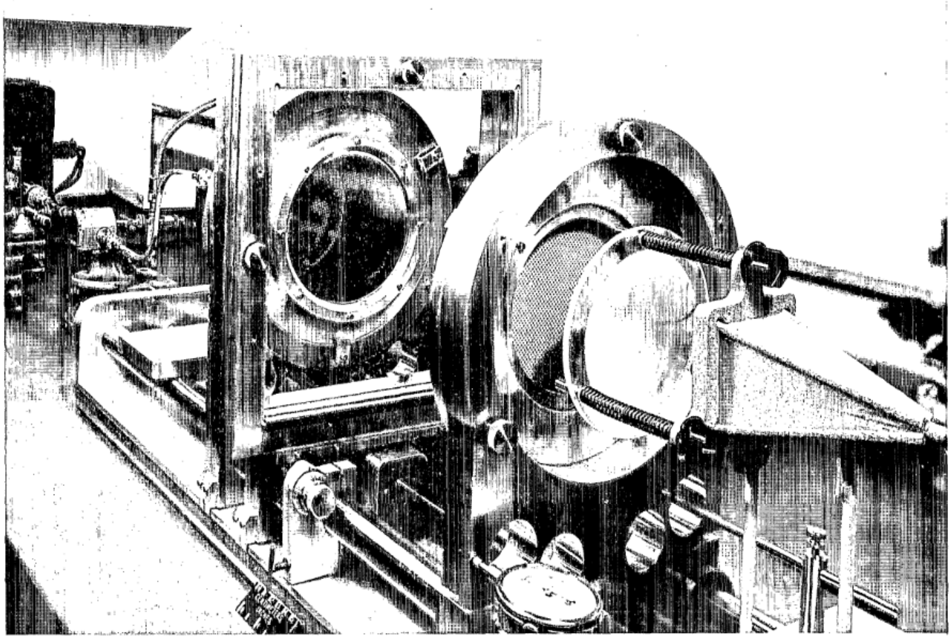

Fig. 1.7: Structure of a flat-plate Fabry-Pérot resonant cavity. Image from [9].

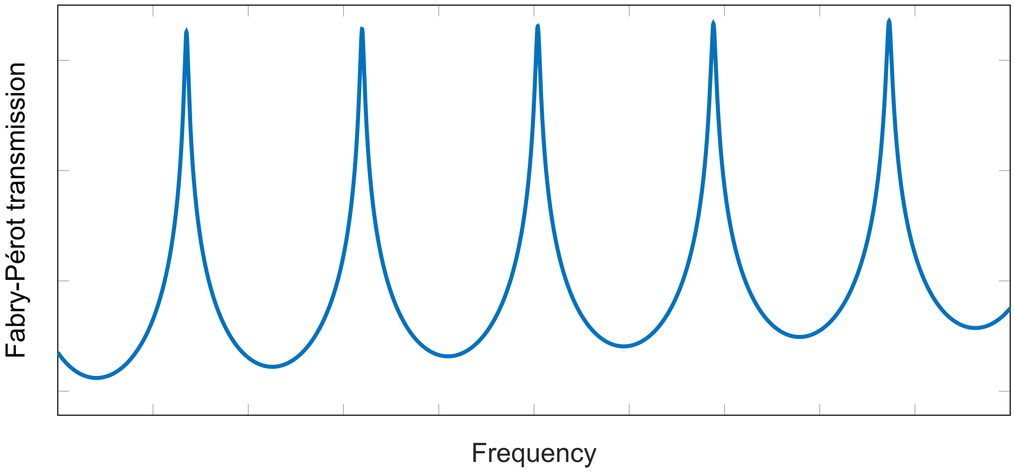

Fig. 1.8: Example of the expected Fabry-Pérot interferometer response. Each resonance peak gives a measurement of the dielectric losses. How the dielectric losses are obtained from the resonance peaks is explained in chapter 5.

1.5. Aim of this project and thesis outline

The aim of this project is to provide a design ”toolbox” for the on-chip Fabry-Pérot interferometers and to validate the concept by measuring the dielectric loss in two materials: polyimide (PI) and amorphous silicon (a-Si). This thesis is therefore divide into three parts. Part I provides the theoretical background required to model and design the Fabry-Pérot interferometer. Part II discusses the general design procedure and the design of a polyimide and amorphous silicon chip. Part III gives an overview of the measurements, analysis, and results of both chips. The thesis is concluded with recommendations for improvements and future work.

The outline of the thesis is as follows:

Part I: Theory This part gives the required theoretical background required to model superconducting transmission lines and the Fabry-Pérot interferometer. Furthermore it discusses how the resonance peaks of the interferometer depend on the losses of the resonator. It ends with a short introduction to the microwave kinetic inductance detector (MKID).

Chapter 2: Superconductivity Introduces the concept of kinetic inductance which is required to model superconducting transmission lines.

Chapter 3: Transmission lines Together with Appendix A and B this chapter introduces the transmission line, ABCD-matrix, and S-parameters concepts. The second part of this chapter gives the mathematical expressions used to model the superconducting microstrip and coplanar waveguide.

Chapter 4: Half wave in-line resonator Introduces the half wave in-line resonator which is used to realize the on-chip Fabry-Pérot interferometer. Using the concepts introduced in chapter 3 the transmission curve of such a resonator is modelled.

Chapter 5: Q-factors Gives the relation between Q-factors and the resonator curve of the Fabry-Pérot interferometer.

Chapter 6: Microwave Kinetic Inductance Detectors (MKID) A short introduction of the MKID.

Part II: Experimental overview This part describes the concept of the experiment and the design methodology. It includes the design of a polyimide and amorphous silicon chip.

Chapter 7: Experiment description The concept of the experiment is introduced including the measurement set-up and how to obtain the dielectric loss from the interferometer's resonance curve. It then introduces the design methodology for the on-chip Fabry-Pérot interferometer.

Chapter 8: Detailed design This chapter gives the design of the polyimide and amorphous silicon chip including the couplers required to create the half wave resonator.

Part III: Measurements This part gives an overview of the measurements performed with the polyimide and amorphous silicon chips.

Chapter 9: Polyimide proof of concept measurements The polyimide chip measurement and analysis act as a proof of concept for the lab-on-chip FP interferometer. It is focussed on qualitative statements regarding the measurement set-up and the obtained results.

Chapter 10: a-Si measurements Using the lab-on-chip FP interferometer the losses in an a-Si based microstrip line are measured.

Chapter 11: Conclusion

Chapter 12: Recommendations

I

Theory

2

Superconductivity

On April 8, 1911, Kamerlingh Onnes found that the resistance of a mercury wire vanished when cooled down to temperatures close to 0 Kelvin. He named this phenomenon ”supraconductivity” but later adopted the term ”superconductivity”. It took until 1957 for Bardeen, Cooper and Schiefer to introduce BCS theory [19] which explains the phenomenon Kamerlingh Onnes found with a net attraction between electrons in the metal. When the net attraction between electrons overcomes the coulomb repulsion between the electrons they form a cooper pair.

2.1. Cooper pairs and quasiparticles

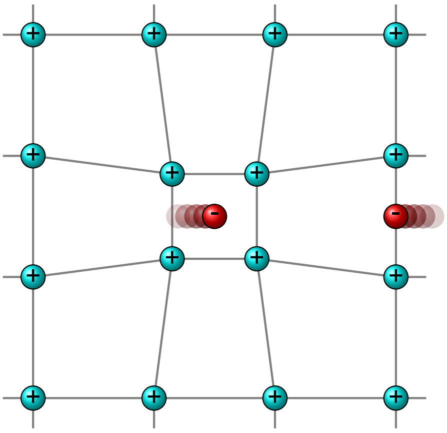

Fig. 2.1: lattice distortion creating a region of positive charge.

When superconductors are cooled below their critical temperature T_c a pair of electrons can form a Cooper pair. Normally two electrons have a repulsive coulomb interaction creating a repulsive force between the electrons. However when cooled below the critical temperature the electrons will distort the lattice creating a region of net positive charge. This region with net positive charge can attract another electron (Fig. 2.1) if it overcomes the coulomb repulsion between the electrons. In this case electrons can pair up and form a Cooper pair. At $T << T_c$ the binding energy of a cooper pair is given by

$$2\Delta \approx 3.5 k_B T_c \tag{2.1}$$

where k_B is Boltzmann’s constant (1.38×10^{-13} J/K or 8.617×10^{-5} eV/K). For NbTiN, with a T_c of 15 K, Δ is given by 0.194 meV.

The electrons that do not pair up to form a cooper pair are referred to as quasiparticles. The density of the remaining quasiparticles in the superconductor is temperature dependent and is given by

$$n_{qp} \approx 2N_0\sqrt{2\pi k_B T\Delta}\exp\left(-\Delta/k_B T\right) \tag{2.2}$$

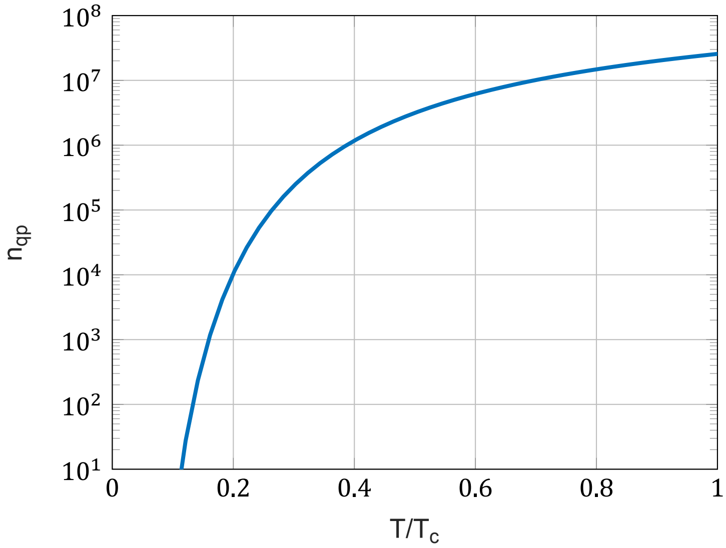

Fig. 2.2: The quasiparticle $n_q p$ density in a superconductor as a function of the temperature T. T_c is the critical temperature of the superconductor. The quasipartcicle density $n_q p$ drops rapidly for temperatures below the critical temperatures T_c of the superconductor.

where N_0 is the density of states of the metal. The approximation in (2.2) is only valid for a thermal quasiparticle distribution and $k_B T << \Delta$. The number of quasiparticles in a system (N_{qp}) is then given by

$$N_{qp} = n_{qp} V \tag{2.3}$$

where V is the volume of the superconductor. The remaining quasiparticles in the superconductor will cause ohmic losses but (2.2) and Fig. 2.2 show that these losses will drop to zero for temperatures well below the critical temperature T_c.

2.2. Complex conductivity

For this experiment it is sufficient to describe superconductors by their complex conductivity as introduced in mattis-bardeen theory [20]

$$\sigma = \sigma_1 - i\sigma_2. \tag{2.4}$$

The real part of the complex conductivity (σ_1) is due to restive losses of the normal electrons (quasiparticles). The imaginary part (σ_2) has an inductive nature and is due to the inertia of the Cooper pairs.

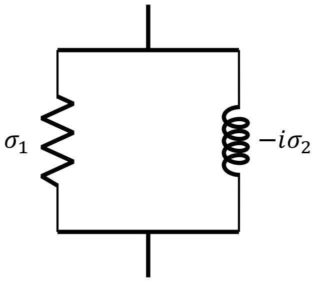

Fig. 2.3: Superconducting film modelled as a resistive component (σ_1) and an inductive component (σ_2).

The cooper pairs in the superconductor will have a certain velocity due to the electromagnetic field at the surface of the superconductor. When the electromagnetic field changes (AC) the Cooper pairs will be accelerated. The change in velocity of the Cooper pairs is opposed by the inertia of the Cooper pairs. This is similar to the behaviour of an electric inductor which opposes a change in the current flowing through it.

The real part of the complex conductivity (σ_1) and the imaginary part (σ_2) can be evaluated for $kT, \hbar\omega < 2\Delta$ [21]-[23]

$$\frac{\sigma_1}{\sigma_N} = \frac{4\Delta}{\hbar\omega} \exp\left(-\Delta/k_B T\right) \sinh\left(\frac{\hbar\omega}{2k_B T}\right) K_0\left(\frac{\hbar\omega}{2k_B T}\right), \tag{2.5}$$

$$\frac{\sigma_2}{\sigma_N} = \frac{\pi\Delta}{\hbar\omega}\left[1 - 2\exp\left(-\Delta/k_B T\right) \sinh\left(\frac{-\hbar\omega}{2k_B T}\right) I_0\left(\frac{\hbar\omega}{2k_B T}\right)\right], \tag{2.6}$$

where Δ is the energy gap of the superconductor and T is the temperature of the superconductor in Kelvin. K_0 and I_0 are the modified Bessel functions of the first and second kind.

In the dirty limit, where the superconducting coherence length ξ is smaller than the penetration depth λ ($\xi << \lambda$), σ_1 and σ_2 are related to the surface impedance by [21],[24],[25]

$$Z_s = \sqrt{\frac{i\mu_0\omega}{\sigma_1 - i\sigma_2}} \coth\left(d\sqrt{i\omega\mu_0\sigma}\right) = R_s + i\omega L_s \tag{2.7}$$

with d the thickness of the superconducting film.

The inductive part of the complex surface impedance is referred to as the kinetic inductance as it originates from the inductive behaviour of the Cooper pairs. The sheet kinetic inductance of a superconducting film can be calculated easily using the Mattis-Bardeen result [26]

$$L_s = \frac{\hbar R_s}{\pi\Delta}. \tag{2.8}$$

The penetration depth of the superconducting film is given by

$$\lambda = \frac{L_s}{\mu_0}. \tag{2.9}$$

3

Transmission Lines

In this section the microstrip and coplanar waveguide transmission lines are mathematically described. This description is based on the concept of two-ports where every device, lumped element and transmission line can be described by a simple "building block".

The two-port of a transmission line section is given in Fig. 3.1 in which the transmission line is described by its length, characterstic imepdance (Z_0) and complex propagation constant (γ)

$$\gamma = \alpha + j\beta. \tag{3.1}$$

The attenuation constant α characterizes the loss per unit length and the phase constant β characterizes the change in phase per unit length.

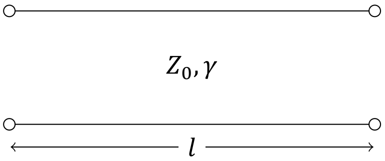

Fig. 3.1: Two port reperesentation of a transmission line section

3.1. Microstrip

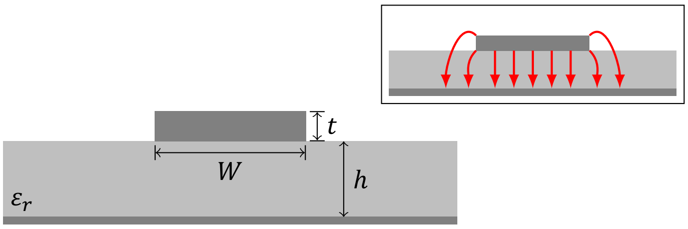

Fig. 3.2: Microstrip geometry: h is the height of the dielectric, W is the width of the microstrip line and t is the thickness of the line. **(inset)** Electric field distribution of a microstrip transmission line, note the 'fringing fields' at the edges of the strip.

A typical microstrip consists of a conducting line, or strip, seperated from the ground plane by a dielectric layer as in Fig. 3.2. The effective dielectric constant of a microstrip is not simply the avarage of the media above and below the line, typically air and the dielectric layer respectively, but is given by [27]

$$\varepsilon_{eff} = \frac{\varepsilon_r + 1}{2} + \frac{\varepsilon_r - 1}{2} \frac{1}{\sqrt{1 + 12h/W}} \tag{3.2}$$

which takes the field distribution of the microstrip into account. The propagation constant is then given by

$$\beta_m = k_0\sqrt{\varepsilon_{eff}} \tag{3.3}$$

where k_0 is the wave number in free space. The characteristic impedance of the line is given by

$$Z_m = \begin{cases} \dfrac{60}{\sqrt{\varepsilon_{eff}}}\ln\left(\dfrac{8h}{W}+\dfrac{W}{4h}\right) & \text{for } W/h \leq 1 \\ \dfrac{120\pi}{\sqrt{\varepsilon_{eff}}\,[W/h+1.393+0.667\ln(W/h+1.444)]} & \text{for } W/h \geq 1. \end{cases} \tag{3.4}$$

Equation (3.3) and (3.4) are not sufficient to describe superconducting microstrips. Currently the best model to describe superconducting microstrips is given by Yassin in [28]. This model uses the modal values calculated in (3.4) and (3.3) together with the penetration depth from (2.9) to calculate the propagation constant β and the characteristic impedance Z_0 for the superconducting microstrip

$$\begin{pmatrix}\beta\\ Z_0\end{pmatrix} = \begin{pmatrix}\beta_m\\ Z_m\end{pmatrix}\left(1+2\chi\frac{\lambda}{h}\right)^{1/2}. \tag{3.5}$$

Calculating the penetration factor χ requires conformal mapping techniques [29] and evaluating integrals in the presence of singularities. Yassin [28] gives the resulting analytical expression

$$\chi = \begin{cases} \dfrac{Is1+Is2+Ig1+Ig2+\pi}{2\ln[rb/(ra)]} & \text{for } W/h < 2 \\ \dfrac{Is1+Is2+Ig1+Ig2+\pi}{2\ln[2rb/(ra)]} & \text{otherwise,} \end{cases} \tag{3.6}$$

which includes the contributions from the bottom surface of the line

$$Is1 = \ln\left(\frac{2p-(p+1)ra+2(pRa)^{1/2}}{ra(p-1)}\right) \tag{3.7}$$

$$Ra = (1-ra)(p-ra), \tag{3.8}$$

the top surface of the line

$$Is2 = -\ln\left(\frac{(p+1)rb-2p-2(pRb)^{1/2}}{rb(p-1)}\right) \tag{3.9}$$

$$Rb = (rb-1)(rb-p), \tag{3.10}$$

and the ground plane

$$Ig1 = \ln\left(\frac{(p+1)rb+2p+2(pRb')^{1/2}}{rb(p-1)}\right) \tag{3.11}$$

$$Rb' = (rb+1)(rb+p) \tag{3.12}$$

$$Ig2 = \ln\left(\frac{(p+1)ra+2p+2(pRa')^{1/2}}{ra(p-1)}\right) \tag{3.13}$$

$$Ra' = (ra+1)(ra+p). \tag{3.14}$$

ra is given by

$$\begin{aligned}\ln(ra) = -1 - \frac{\pi w}{2h} - \frac{p+1}{p^{1/2}}\tanh^{-1}\left(p^{-1/2}\right) \\ - \ln\left(\frac{p-1}{4p}\right),\end{aligned} \tag{3.15}$$

and rb is given as

$$rb = rbo \tag{3.16}$$

for $w/h \geq 5$ and

$$\begin{aligned} rb = rb0 &- [(rb0-1)(rbo-p)]^{1/2} \\ &+ (p+1)\tanh^{-1}\left(\frac{rbo-p}{rbo-1}\right)^{1/2} \\ &- 2p^{1/2}\tanh^{-1}\left(\frac{rbo-p}{p(rbo-1)}\right)^{1/2} + \frac{\pi w}{2h}p^{1/2} \end{aligned} \tag{3.17}$$

otherwise, where

$$rbo = \eta + \frac{p+1}{2}\ln\Delta \tag{3.18}$$

with

$$\eta = p^{1/2}\left\{\frac{\pi w}{2h} + \frac{p+1}{2p^{1/2}}\left[1+\ln\left(\frac{4}{p-1}\right)\right] - 2\tanh^{-1}p^{-1/2}\right\} \tag{3.19}$$

$$\Delta = \max(\eta, p) \tag{3.20}$$

$$p = 2b^2 - 1 + 2b(b^2-1)^{1/2} \tag{3.21}$$

$$b = 1 + t/h. \tag{3.22}$$

Note that the expressions given by Yassin are valid when the thickness of the film is much greater than the penetration depth, this is not the case for the microstrips geometries used for this experimented. However the deviation between the line parameters found by using SONNET [30] and Yassin [28] for films thinner than the penetration depth are small. The equations from Yassin can thus be used as a first order approximation of the microstrip line parameters. For the design of the FP chips the line parameters found with SONNET are used.

3.2. Coplanar waveguide

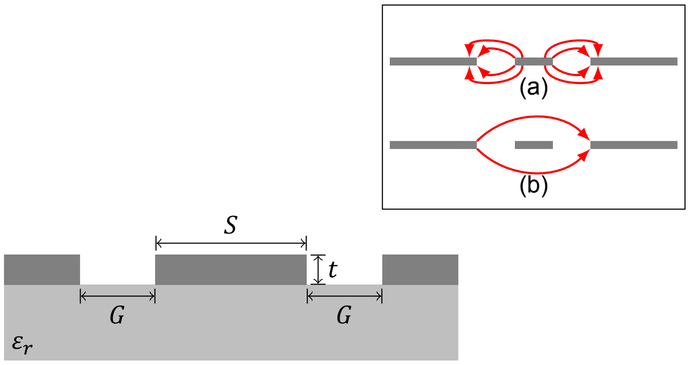

Fig. 3.3: CPW geometry: S is the width of the central conductor, G is the gap between the central conductor and the ground plane on both sides and t is the thickness of the film. **(inset)** Electric field distribution for **a)** the differential mode and **b)** the common mode.

For the Coplanar waveguide (CPW) structure the geometric and kinetic inductance can be calculated separately.

For a standard CPW the geometric inductance per unit length can be calculated as

$$L_{g,l} = \frac{\mu_0}{4}\frac{K(\sqrt{1-k^2})}{K(k)} \tag{3.23}$$

and the capacitance per unit length as

$$C_l = 4\varepsilon_0\varepsilon_{eff}\frac{K(k)}{K(\sqrt{1-k^2})} \tag{3.24}$$

with

$$\varepsilon_{eff} = \frac{1+\varepsilon_r}{2}, \tag{3.25}$$

$$k = \frac{S}{S+2G}, \tag{3.26}$$

and K the complete elliptical integral of the first kind. For the non-superconducting CPW the inductance of the line is equal to the geometric inductance ($L_{g,l}$). When the CPW line becomes superconducting the inductance of the line is not just the geometric inductance but includes the contribution from the kinetic inductance L_k (2.8).

Using conformal mapping techniques [31] the kinetic inductance contribution can be calculated as a geometric contribution from the central line (g_c) and the ground plane (g_g).

For the contribution of the central line

$$g_c = \frac{1}{4S(1-k^2)K^2(k)}\left[\pi + \ln\left(\frac{4\pi S}{d}\right) - k\ln\left(\frac{1+k}{1-k}\right)\right] \tag{3.27}$$

and for the contribution of the ground plane

$$g_g = \frac{1}{4S(1-k^2)K^2(k)}\left[\pi + \ln\left(\frac{4\pi(S+2G)}{d}\right) - \frac{1}{k}\ln\left(\frac{1+k}{1-k}\right)\right]. \tag{3.28}$$

The kinetic inductance per unit length is then the sum of the two geometric contributions times the kinetic sheet inductance

$$L_{k,l} = L_{k,s}\cdot(g_g + g_c). \tag{3.29}$$

The total inductance of the CPW transmission line is then given by the sum of the geometric inductance ($L_{g,l}$) and the kinetic inductance ($L_{k,l}$)

$$L_l = L_{g,l} + L_{k,l}, \tag{3.30}$$

with the kinetic inductance fraction

$$\alpha_k = \frac{L_{k,l}}{L_{g,l} + L_{k,l}}. \tag{3.31}$$

The line impedance and the phase velocity of the CPW then follow as

$$Z_0 = \sqrt{\frac{L_l}{C_l}}, \tag{3.32}$$

$$v_{phase} = \sqrt{\frac{1}{C_l L_l}}. \tag{3.33}$$

The effective dielectric constant, ε_{eff}, of the CPW line is given by

$$\varepsilon_{eff} = \left(\frac{c_0}{v_{phase}}\right)^2. \tag{3.34}$$

4

Half wave in-line resonator

The FP resonators consist of half wave in-line resonators A half wave in-line resonator can be modelled as a section of transmission line with length l, referred to as the resonator line, capacitively coupled to the feed network on both sides as in Fig. 4.1.

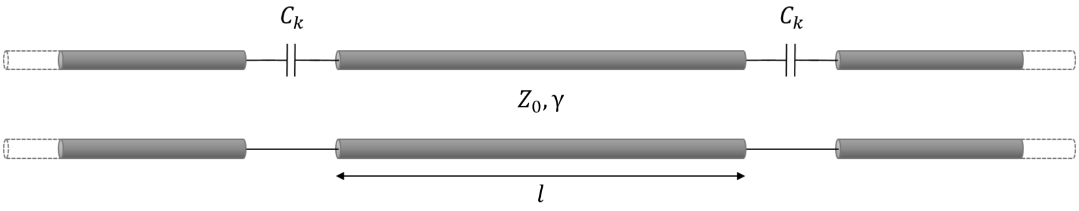

Fig. 4.1: In line resonator. The resonator section of the transmission line is described by it's length (l), characteristic impedance (Z_0) and complex propagation constant (γ). The couplers are modelled as in-line capacitors with capacitance C_k.

The first resonance frequency f_0, or lowest order resonance, of this resonator depends on the length and the effective dielectric constant (ϵ_{eff}) of the resonator line

$$f_0 = \frac{c_0}{2l\sqrt{\varepsilon_{eff}}} \tag{4.1}$$

or, in terms of the capacitance and impedance of the line

$$f_0 = \frac{1}{2l}\frac{1}{\sqrt{L_l C_l}}. \tag{4.2}$$

The higher order modes are then given by

$$f_n = nf_0 \quad n = 1, 2, 3, ... \tag{4.3}$$

where n is the mode number and f_0 is the first resonance frequency as well as the frequency spacing between resonance peaks. The first two modes of a half wave resonator, $n = 1$ and $n = 2$, are given in Fig. 4.2.

The response of a resonator can be described by the scattering parameters of the resonator. An introduction to scattering parameters is given in Appendix A. The magnitude of transmission trough the resonator is given by $|S_{12}|$ and $|S_{21}|$ while reflection at the ports of the resonator is given by $|S_{11}|$ and $|S_{22}|$.

The full transmission curve $|S_{21}|$, including higher order resonances, can be calculated by cascading the ABCD matrices of the different circuit elements to obtain the ABCD matrix of the complete resonator. The concept of ABCD matrices is introduces in appendix B and [32]. For the half wave resonator as modelled in Fig. 4.1 the total ABCD matrix is given by

$$\begin{bmatrix} A & B \\ C & D \end{bmatrix} = \begin{bmatrix} 1 & \frac{1}{j\omega C_k} \\ 0 & 1 \end{bmatrix} \begin{bmatrix} \cosh(\gamma l) & Z_0 \sinh(\gamma l) \\ Y_0 \sinh(\gamma l) & \cosh(\gamma l) \end{bmatrix} \begin{bmatrix} 1 & \frac{1}{j\omega C_k} \\ 0 & 1 \end{bmatrix} \tag{4.4}$$

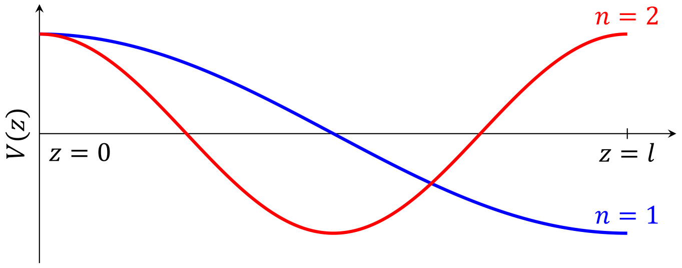

Fig. 4.2: First two modes $n = 1$ and $n = 2$ for an open-open half wave resonator. The end points of the line at $z = 0$ and $z = l$ are voltage anti-nodes, at which point the amplitude of the voltage standing wave in the resonator is maximum.

where

$$\gamma = \alpha + j\beta \tag{4.5}$$

the complex propagation constant of the line and

$$Y_0 = \frac{1}{Z_0} \tag{4.6}$$

the admittance of the line, and C_k is the capacitance of the coupler as in Fig. 4.1.

The ABCD matrix can than be converted to the S-parameters (Appendix C) by taking the impedance of the feed network lines into account. Assuming the feed line on both sides of the resonator is identical, the transmission trough the resonator, $|S_{21}|$ is given by

$$|S_{21}| = \left|\frac{2}{A + Z_l/B + Z_lC + D}\right|. \tag{4.7}$$

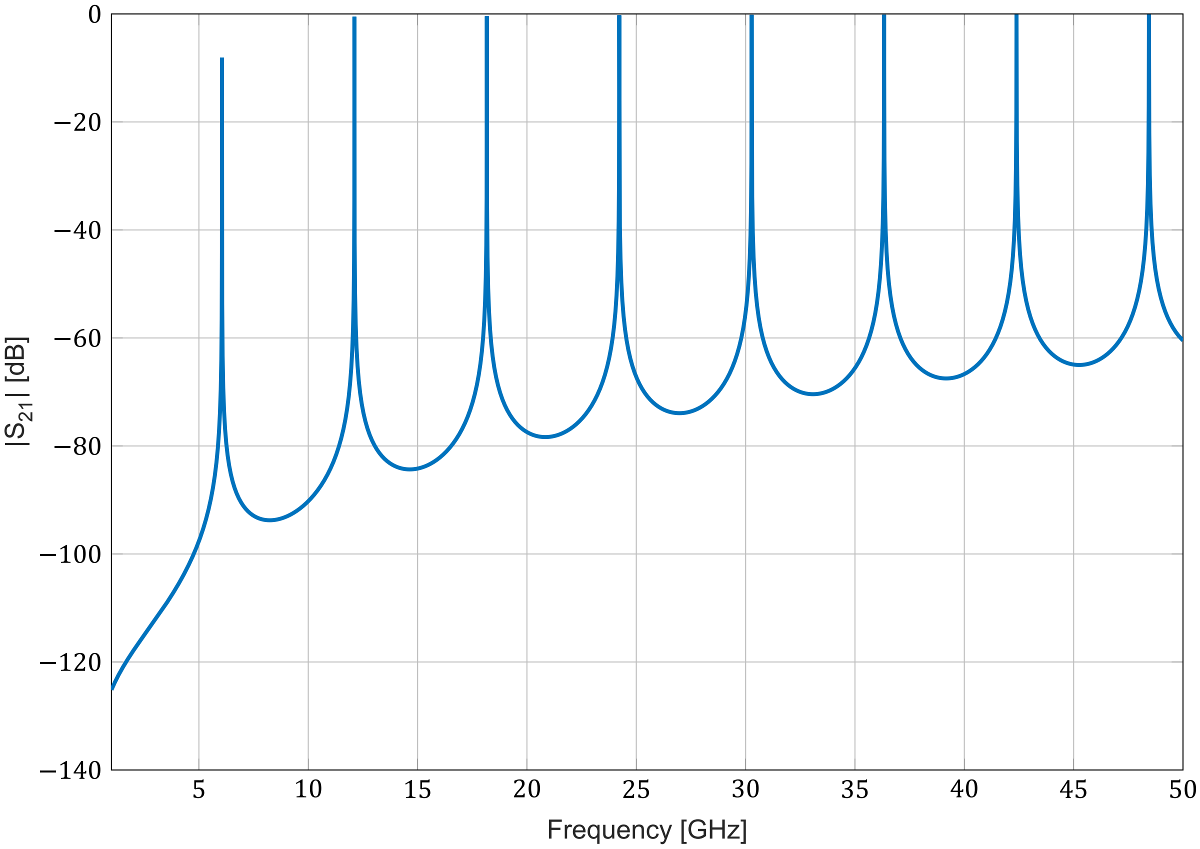

Fig. 4.3: Example of a resonator curve using the model of Fig. 4.1 and (4.4) and (4.7).

5

Q-factors

Resonator circuits are often described in terms of quality factors Q. The quality factor of a resonance circuit is defined as the energy stored in the resonator E_{stored} over the power lost per cycle P_{loss}

$$Q = \frac{\omega E_{stored}}{P_{loss}}. \tag{5.1}$$

The resonator circuit loses energy due to dissipative losses Q_i and coupling to the external circuitry Q_c. The total, or loaded, quality factor of the circuit Q_l is given by the combination of these two terms

$$\frac{1}{Q_l} = \frac{1}{Q_i} + \frac{1}{Q_c}. \tag{5.2}$$

5.1. Coupler quality factor $\mathbf{Q_c}$

The coupler quality factor Q_c describes the strength of the coupling to the external circuit e.g. the feed or readout lines. In the context of Q-factors coupling is seen as energy leaking out of the resonator, a high Q_c thus requires weak coupling to the external circuitry.

Following the derivation of Barends [22] but adapting it to half-wave resonators, the coupling quality factor Q_c can be derived in terms of S-parameters. To derive Q_c of an in-line resonator as in Fig. 4.1 the first step is to analyse a single coupler, treating coupler 2 as an open. In this case the power leaking out trough the coupler each cycle is given by

$$P_{loss} = N f E_{stored} |S_{21,c}|^2 \tag{5.3}$$

where f is the frequency, $|S_{21,c}|^2$ is the power leaking out of the resonator trough the coupler and N is the number of times the coupler is encountered per cycle. For a half wave resonator $N = 1/n$ where n is the mode number of the half wave resonator (Fig. 4.2). Combining (5.1) and (5.3) this results in

$$Q_{c1} = \frac{2n\pi}{|S_{21,c}|^2}. \tag{5.4}$$

Including the second coupler the total coupling Q-factor of the resonator is given by

$$\frac{1}{Q_c} = \frac{1}{Q_{c1}} + \frac{1}{Q_{c2}}. \tag{5.5}$$

Assuming $Q_{c1} = Q_{2c}$ this results in

$$Q_c = \frac{n\pi}{|S_{21,c}|^2}. \tag{5.6}$$

5.2. Dissipative losses $\mathbf{Q_i}$

The losses intrinsic to the resonator are given by the intrinsic quality factor Q_i. There are multiple loss mechanism which contribute to Q_i, for this design the following are taken into account:

- $\mathbf{Q_{i,rad}}$: Transmission lines can suffer from radiation losses. For the CPW configuration, if the propogation velocity of the guided signal is faster than the electromagnetic propagation velocity in the substrate, the guided signal loses enery in the form of an electromagnetic shock wave [33] -[36] which is launched into the substrate at an angle

  $$\cos(\psi) = \frac{\sqrt{\varepsilon_{eff}(f)}}{\sqrt{\varepsilon_r}}. \tag{5.7}$$

  If $\varepsilon_{eff} > \varepsilon_r$, i.e. the propgation velocity of the line guided signal is slower than the velocity in the substrate, $\psi = 0$ which eliminates the shock wave. In this case the radiation loss of the CPW is negligible.

  Furthermore the CPW line supports a common mode, see Fig. 3.3, which is not a propagating mode but a leaky wave current distribution which radiates power in a few wavelengths. This mode generally arises when the ground plane of the CPW is disturbed, e.g. when a structure, such as a coupler, interacts with the CPW creating a discontinuity in the line. At these discontinuities the field distribution on the line changes and thus the intrinsic impedance Z_0 of the line changes resulting in reflection and the excitation of the common mode in the CPW line.

- $\mathbf{Q_{i,die}}$: Dielectric materials have intrinsic dissipative losses. The dielectric losses depend on the loss tangent of the dielectric material as

  $$Q_i = \frac{1}{\tan\delta} = \frac{\beta}{2\alpha}. \tag{5.8}$$

  where α and β are the real and imaginary part of the complex propagation constant γ

  $$\gamma = \alpha + j\beta. \tag{5.9}$$

- $\mathbf{Q_{i,R}}$: The resistive losses in a superconductor are the result of thermally excited quasiparticles. Since the number of quasi particles decreases exponentially with temperatures the resistive losses are negligible for temperatures well below T_c as given in (2.2) and Fig. 2.2.

- $\mathbf{Q_{i,rad,coupler}}$: The couplers required for the Fabry-Pérot interferometer are discontinuities in the line and thus result in radiation losses, see radiation losses above. Although the full properties of the radiation losses within the coupler are unknown, qualitative simulations show that the radiation losses scale with mode number and depend on the coupler shape. The radiation losses in the coupler can be handled as an unknown change in the coupler quality factor Q_c

  $$\frac{1}{Q_c} = \frac{1}{Q_c'} + \frac{1}{Q_{i,rad,coupler}} \tag{5.10}$$

  where both Q_c', see (5.6), and $Q_{i,rad,coupler}$ scale with mode number n.

- $\mathbf{Q_{i,sub}}$: The wafer, or substrate, consists of a crystalline material for which dielectric losses will be negligible ($\tan(\delta) \approx 0,\ Q_i \to \infty$).

These contributions combine into a net loss

$$Q_i = \left(\frac{1}{Q_{i,rad}} + \frac{1}{Q_{i,die}} + \frac{1}{Q_{i,R}} + \frac{1}{Q_{i,sub}}\right)^{-1}. \tag{5.11}$$

At temperatures below T_c the ohmic losses of the conductors will drop to zero, see section 2.1. In this case the main loss contributions of the line are the radiative and dielectric losses. The radiative losses of a microstrip are negligible and thus Q_i is dominated by $Q_{i,dielectric}$.

For a superconducting CPW line radiative losses are negligible as long as the phase velocity of the line is slow compared to the phase velocity in the substrate ($\epsilon_{eff} > \epsilon_r$). If this condition is not met radiation is the dominant loss mechanism [13]. If the CPW geometry contains a dielectric layer, i.e. a CPW covered with a thin dielectric layer, $Q_{i,die}$ will contribute to Q_i.

5.2.1. Fill fraction

Since only a part of the electric field surrounding the line is concentrated in the dielectric layer, see Fig. 3.2 and 3.3, the loss tangent of the line is not equal to the loss tangent of the dielectric. This is described by the fill fraction (FF) which is defined as the fraction of the total field in the dielectric material. The dielectric losses in the line are then given by

$$\tan\delta_{line} = FF \cdot \tan\delta_{dielectric} \tag{5.12}$$

and Q_i of the line

$$Q_{i,line} = \left(\frac{1}{FF}\right) Q_{i,dielectric}, \tag{5.13}$$

where

$$FF \leq 1. \tag{5.14}$$

The fill fraction depends on the line geometry and the dielectric constant of the dielectric material. The fill fraction can be found from simulations using

$$\frac{P_o}{P_{in}} = e^{-2\alpha l} \tag{5.15}$$

in which l is the length of the line and P_o/P_{in} is the loss factor which gives the relation between input and output power of a transmission line. The loss factor P_o/P_{in} of a line can be obtained with commercial solvers. By simulating a section of line with length l and with a dielectric layer with a certain dielectric loss $Q_{i,loss}$, the loss factor is obtained. Using (5.8) and (5.15) the losses of the line $Q_{i,line}$ can be calculated from this loss factor. The difference between the losses of the dielectric $Q_{i,dielectric}$ and the losses of the line $Q_{i,line}$ gives the fill fraction (5.13) .

As an example, for a 2-2-2 CPW line covered by a 1 micron polyimide dielectric a fill fraction of 15% is obtained. A microstrip with a width of 2 micron on the same polyimide dielectric has a fill fraction of 60%.

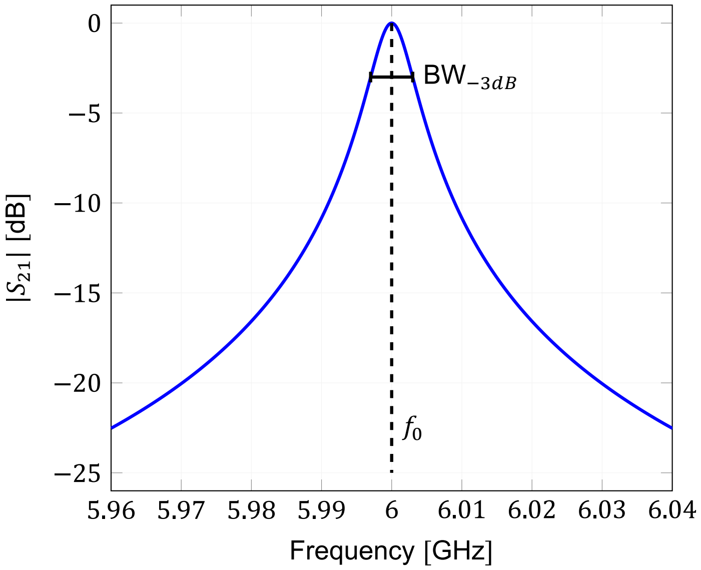

Fig. 5.1: Each of the resonance peaks in the transmission curve of an in-line resonator has a lorentzian shape. The lorentzian shape is defined by the resonance frequency f_0 and the $3dB$ bandwidth BW_{-3dB}. The loaded Q factor Q_l of the resonator is then given by f_0/BW_{-3dB}.

5.3. Describing resonators by Q-factors

The S_{21} curve obtained through (4.4) and (4.7) and given in Fig. 4.3 gives information about the Quality factors of the resonator circuit. The loaded Quality factor Q_l of the resonator can be obtained from the resonance peaks. Each of the resonance peaks has a lorentzian shape (Fig. 5.1) for which the loaded quality factor Q_l is given by the resonance frequency and the -3dB bandwidth, relative to the peak height, as

$$Q_l = \frac{f_0}{BW_{-3dB}}. \tag{5.16}$$

Since Q_l depends on Q_i and Q_c it is impossible to determine Q_i from this measurement alone assuming that Q_c is not accurately known. Even though Q_c is given by the design of the coupler (Eq. 5.6) the final realised Q_c on the manufactured chips can differ from the designed Q_c due to fabrication tolerances. Measuring the resonance frequency and -3dB bandwidth is thus not enough to determine Q_i with high accuracy.

The peak height $|S_{21,max}|$ is given by

$$|S_{21,max}| = \frac{Q_l}{Q_c}. \tag{5.17}$$

Since Q_l is obtained from the lorentzian shape of the peak, Q_c can be obtained from the peak height $|S_{21,max}|$ and shape. Unfortunately $|S_{21,max}|$ cannot be measured directly in a FP chip, due to uncertainties in the power coupling between source and MKID, and thus (5.17) can not be used to directly determine Q_c. The coupling quality factor Q_c can however be determined from the full transmission curve since not only the peak height $|S_{21,max}|$ depends on Q_c, but the dip depth $|S_{21,min}|$ as well. For a certain Q_l the relative height of the FP peaks $|S_{21,min}| - |S_{21,max}|$ thus depends on the Q_c of the resonator. If the full transmission curve $|S_{21}|$ can be measured, Q_l can be obtained from the peak shape (5.16) and Q_c can be determined from the relative FP peak height. Combining Q_l and Q_c, Q_i can be obtained from (5.2).

A detailed overview of the approaches that can be used to obtain Q_i from the resonator curve measurements is given in section 7.5.

6

Microwave Kinetic Inductance Detector (MKID)

An MKID is a superconducting quarter-wave resonator designed to accurately measure the change in complex surface impedance due to absorbed power [37], [38], [39].

The superconducting resonator is coupled to a readout line, see Fig. 6.1. The quarter-wave resonator can be probed by sending a signal trough the readout line, when the frequency of the signal on the readout line does not match to the resonance frequency the signal is not affected by the resonator. In this case unity transmission, $S_{21} = 0dB$, is obtained. When the frequency of the signal does match to the resonance frequency, the signal is reflected back at the input port of the resonator resulting in a transmission dip in $|S_{21}|$.

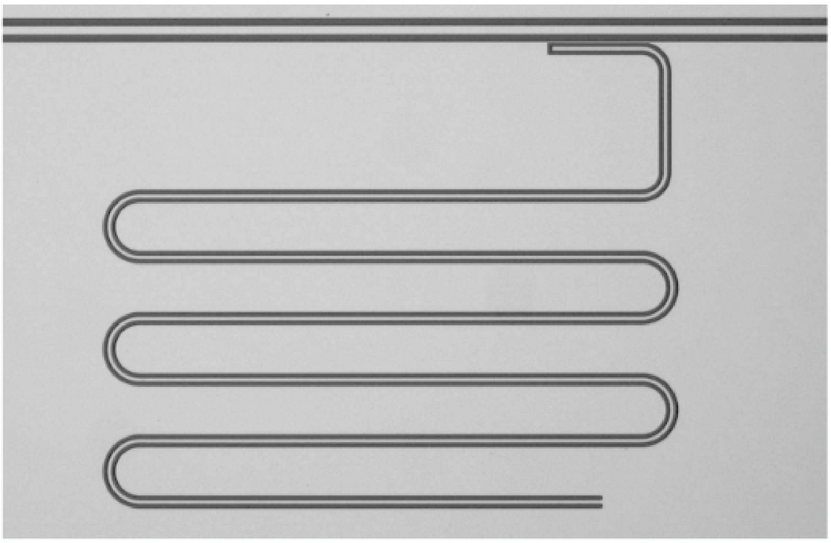

Fig. 6.1: A quarter wave resonator coupled to the readout line (top). In this case the resonator and readout line are created using CPW lines.

Using the quarter-wave resonators KIDs can be multiplexed by ensuring a resonance frequency spacing of the different KID resonators. In this case each KID can be probed by a signal, or tone, corresponding to it's resonance frequency since this tone is not affected by the other KIDs.

6.1. Response

In a dark environment, no photon absorption, the superconducting resonator has a certain resonance frequency f_0 and a loaded quality factor Q_l. If the superconductor absorbs a photon with energy higher than the bonding energy of a Cooper pair,

$$F_{2\Delta} = 2 \cdot \Delta/h = 2 \cdot 1.76 k_B T_c/h \approx 73.6 \cdot T_c \quad (GHz) \tag{6.1}$$

it can break a Cooper pair creating two quasi particles. Since the complex conductivity (2.4) depends on the number of Cooper pairs and quasi particles the absorbed photon will cause a change in the complex conductivity (2.4) of the superconductor. The change in σ_1 and σ_2 due to a change in quasiparticle density is given by [21],[23]

$$\frac{d\sigma_1}{dn_{qp}} \simeq \sigma_N \frac{1}{N_0 \hbar\omega} \sqrt{\frac{2\Delta_0}{\pi k_B T}} \sinh\left(\frac{\hbar\omega}{2k_B T}\right) K_0\left(\frac{\hbar\omega}{2k_B T}\right), \tag{6.2}$$

$$\frac{d\sigma_2}{dn_{qp}} \simeq \sigma_N \frac{-\pi}{2N_0 \hbar\omega} \left[1 + 2\sqrt{\frac{2\Delta_0}{\pi k_B T}} \exp\left(\frac{-\hbar\omega}{2k_B T}\right) I_0\left(\frac{\hbar\omega}{2k_B T}\right)\right]. \tag{6.3}$$

Note that the change in quasiparticle density is expressed as a change in temperature, where the relation between temperature and n_{qp} is given by (2.2). The change in complex conductivity causes a shift in resonance frequency δf_0 which is given by

$$\frac{\delta f_0}{f_0} = \frac{\alpha_k \beta}{4} \frac{\delta\sigma_2}{\sigma_2}, \tag{6.4}$$

with α_k the kinetic inductance fraction from (3.31) and $\beta = 1 + \frac{2d/\lambda}{sinh(2d/\lambda)}$ with λ the penetration depth of the superconductor (2.9).

The change in complex surface impedance also causes a decrease in the intrinsic quality factor Q_i of the resonator given by

$$\delta\left(\frac{1}{Q_i}\right) = \frac{\alpha_k \beta}{2} \frac{\delta\sigma_1}{\sigma_2}. \tag{6.5}$$

Fig. 6.2 demonstrates the changing resonator behaviour due to an increase in quasiparticle density (n_{qp}). With increasing quasiparticle density the resonance frequency shifts to lower frequencies and the transmission dip depth decreases.

Although the magnitude of transmission $|S_{21}|$ gives a good indication of the resonators response to a change in n_{qp} it is more convenient to use the resonance circle in the complex plane for readout. In this case the response due to a changing quasiparticle density is given by [39] a change in amplitude

$$\frac{dA}{dN_{qp}} = -\frac{\alpha_k \beta Q}{|\sigma| V} \frac{d\sigma_1}{dn_{qp}} \tag{6.6}$$

and a change in phase

$$\frac{d\theta}{dN_{qp}} = -\frac{\alpha_k \beta Q}{|\sigma| V} \frac{d\sigma_2}{dn_{qp}}. \tag{6.7}$$

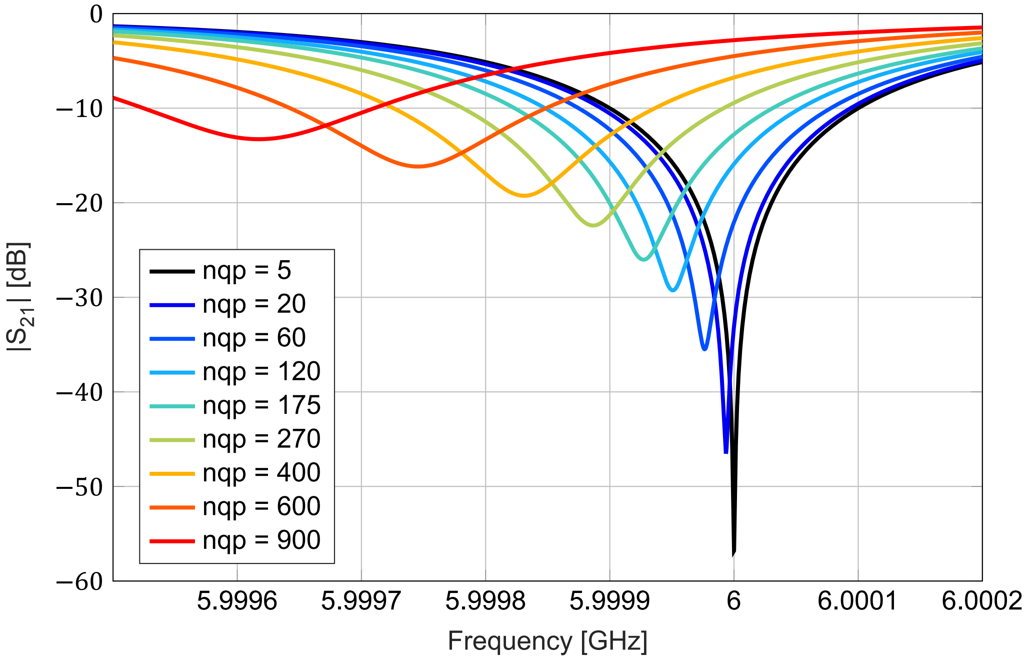

Fig. 6.2: The MKIDs response to different quasiparticle densities n_{qp}. For higher quasiparticle densities the resonance frequency ω_0 shifts to lower frequencies and the dip depth $|S_{21,min}|$ decreases.

6.2. Hybrid MKID

The hybrid MKID consists of two sections, a narrow aluminium section and a wide NbTiN section [40].

Making the aluminium section narrow decreases the volume which increases the detector sensitivity (2.3). Aluminium is chosen because of the following properties:

- Favourable energy gap frequency of roughly 80 GHz (6.1). The gap frequency of the superconductor determines the frequencies to which the detector is sensitive. The MKID is designed for the far infrared frequency range, 300 GHz and up, which requires a gap frequency lower than 300 GHz.
- Aluminium based MKIDs have been proven experimentally to be extremely sensitive [41].

The MKID's sensitivity to quasiparticle changes is maximum at the shorted end of the resonator, at which the current is maximum, which is therefore made from aluminium (Fig. 6.3).

Unfortunately a narrow aluminium section suffers from two-level system (TLS) noise. To decrease the TLS noise of the MKID the second section is made wider [42] and from NbTiN (Fig. 6.3). NbTiN suffers less from TLS noise and increasing the width of the CPW further decreases TLS noise. This section is placed at the coupled open end of the resonator where the electric field is strongest and the TLS noise would thus be maximum.

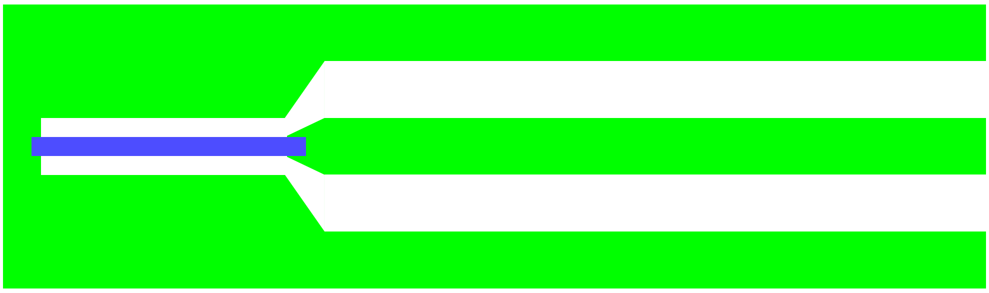

Fig. 6.3: Hybrid MKID with in blue aluminium and in green NbTiN. The thin aluminium section is shorted at one end and connects to the wide NbTiN section at the other end.

II

Experimental overview

7

Experiment description

This chapter explains the basic concept of the experiment and measurement set-up. The in depth design of a polyimide chip and amorphous chip is discussed in section 8.3 and 8.4 respectively.

7.1. Dielectric loss tangent experiments

The goal of this experiment is to determine the loss tangent of dielectric materials at sub-K temperatures and in the terahertz frequency range (300 GHz - 1 THz).

The experiment is set up such that it is applicable for any dielectric material of interest, this thesis provides an toolbox which in principle can be used for any dielectric material. For this thesis research two dielectrics of interest are selected: Polyimide (PI) and amorphous silicon (a-Si). Polyimide is used to construct bridges connecting the ground planes of the CPW lines. The loss tangent of polyimide is required to fully characterize the CPW lines used in e.g., the DESHIMA chip. The detailed design of the polyimide chip is discussed in section 8.3.

Amorphous silicon is a candidate dielectric material for the construction of microstrip lines used in filters for DESHIMA 2.0 and array feeding networks for MOSAIC. It is important that the losses in these lines due to the dielectric are low which requires a high Q_i dielectric. The detailed design of the a-Si chip is discussed in section 8.4.

Table 7.1 gives an overview of the expected Q_i values and the frequencies for which chips are designed. The expected Q_i values are based on the assumption that the Q_i value of a material is frequency independent and might increase at sub-K temperatures. The Polyimide chip acts as a proof of concept experiment and is therefore measured at one frequency. For the full a-Si experiment three frequencies in the terahertz range (300 GHz - 1 THz) are selected.

Table 7.1: Overview of the expected dielectric Q_i factors and the measurement frequencies.

	Polyimide (PI)	**Amorphous silicon (a-Si)**
Expected Q_i range	100 - 1000 [15]	10^3 - 10^5 [16]-[18]
Measurement freq. f_1	350 GHz	350 GHz
Measurement freq. f_2	-	650 GHz
Measurement freq. f_3	-	850 GHz

7.2. Experimental concept

Section 5.3 explains how information on the dielectric losses (Q_i) can be obtained from the transmission curve of a half wave resonator. To measure this transmission curve the resonator is coupled to an antenna on one side and to an MKID (Chapter 6) on the other side. A signal coupled to the antenna will be transmitted trough te resonator to the MKID. The power transmitted through the FP resonator, given by the $|S_{21}|$ curve, is absorbed in the MKID. The response of the MKID thus gives a measurement of the resonator transmission curve $|S_{21}|$.

The set-up for this experiment consists of a THz source, providing a single frequency signal tunable from 100 GHz to 1 THz, the resonator chip, and the cryostat used to cool the chip to temperatures below 1 K. A graphical representation of the set-up is given in Fig. 7.1.

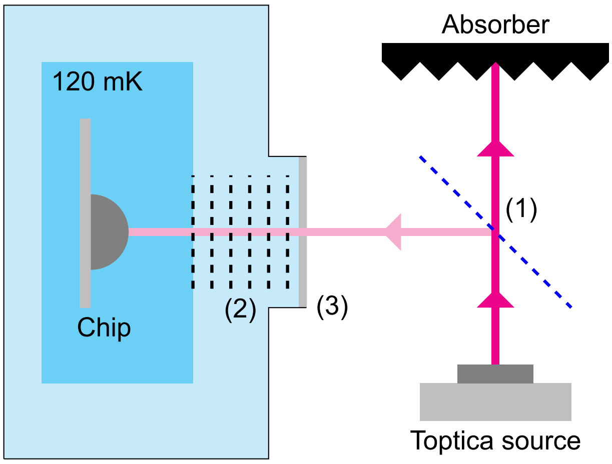

Fig. 7.1: Simplified view of the experimental set-up. Power from the toptica source is coupled to the antenna of the chip trough a beam splitter, the filter stack, and the polariser grid to the chip inside the cryostat. The beam splitter **(1)** reduces the power transmitted into the cryostat, the power not transmitted into the cryostat is absorbed in the absorber. The filter stack **(2)** at the opening of the cryostat creates a bandpass filter. The polariser grid **(3)**, located at the outside of the vacuum window, allows transmission of one polarisation and rejects the other polarisation. The chip is placed in the 120 mK stage of the cryostat.

7.2.1. Terahertz source

The source used for this experiment is the commercial Toptica photomixer [43] with a frequency range from 100 GHz up to 1 THz with a limited frequency resolution of >10 MHz. The source is commercially available and is referred to as the Toptica source.

7.2.2. Beam splitter

A beam splitter is placed between the Toptica source and the opening of the cryostat to reduce the power transmitted into the cryostat. Even at the lowest power setting the signal from the Toptica source would saturate the KIDs at the FP peaks when transmitted directly into the cryostat.

7.2.3. Cryostat

The cryostat used for this experiment is a commercial pulse-tube based He4-He3 cooler and allows for base temperatures below $300mK$.

The chip, when placed in the cryostat, is optically accessible trough a window which contains a bandpass filter stack with three possible bands at 350, 650, and 850 GHz centre frequency. A detailed description of the cryostat set-up can be found in [44].

7.2.4. Chip

An simplified overview of the chip is given in Fig. 7.2. The chip has 4 antennas that pick-up the signal from the toptica source, send it into a transmission line coupled to a Fabry-pérot resonator. The signal transmitted through the FP is measured with MKID detectors. These components will be discussed in more detail in the following subsections. The chip is mounted in a metal sample holder, which in turn is mounted in a magnetic shield. The holder has an opening for the antenna array and place for the 2 coax connectors connected to the bond pads of the chip.

7.2.5. Lens antenna

The antennas used for this chip are twin slot antennas [45]. The section of the chip where the antennas are placed is closed off from the rest of the chip by the chip holder (Fig. 7.2) in order to reduce stray light travelling from the antenna side of the chip to the detector side of the chip, reducing the spurious response (section 7.3).

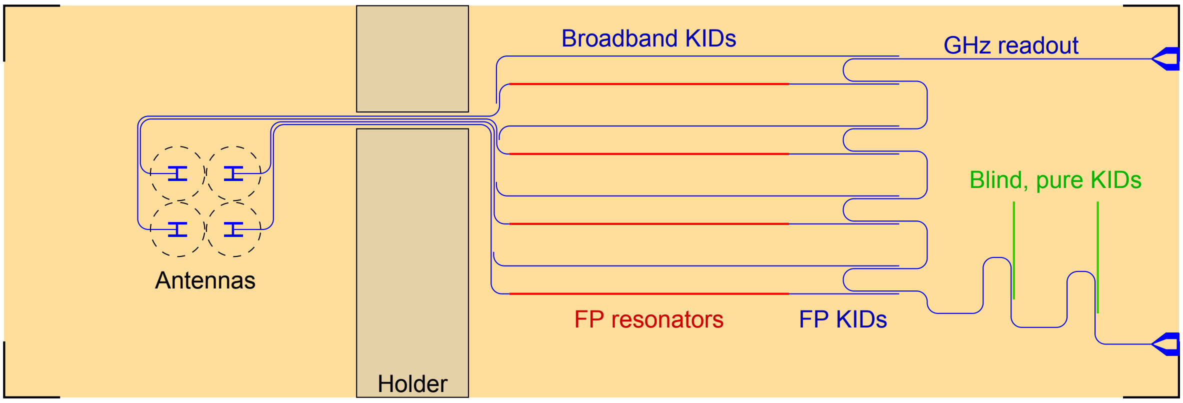

Fig. 7.2: Simplified version of the resonator chip. The grey area indicate the contact area with the chip holder. The dotted lines indicate the lenses placed on the twin slot antennas. The broadband KIDs are not shown in this figure but would be positioned on the blue terahertz line just before the start of the FP resonator.

7.2.6. Polariser grid

The rotatable polariser grid, located at the outside of the vacuum window, allows transmission of one polarisation and rejects the other polarisation in the order of -40dB. The grid consists of thin parallel metallic wires supported by a plastic window. The twin-slot antenna accepts a single polarisation, by matching the polarisation transmitted trough the polariser to the antenna the spurious response can be reduced relative to the FP transmission. The polarisation not coupled to the antenna can end up as a stray light signal in the chip which can be coupled to the KIDs themselves, see section 7.3. This contribution to the spurious response, which does not contribute to the signal transmitted trough the Fabry-Pérot, can be removed with the polariser grid.

7.2.7. Resonator

The chip will contain multiple half wave resonators (chapter 4) each connected to a separate antenna and readout KID. Each resonator can be designed for different Q_c values and resonator lengths. The length of the resonators can be increased by meandering the resonator line back and forth. At the end of the resonator the line is coupled directly to the KID.

7.2.8. KIDs

The chip contains multiple KIDs which can be grouped into the following types:

- **FP KIDs** On the readout side of the chip the FP resonators are coupled to a hybrid KID. The response of this KID depends on the transmission trough the FP resonator and thus traces the $|S_{21}|$ curve of the FP resonator.
- **Blind KIDs** An MKID that is not coupled to a resonator,referred to as a blind MKID, can be used to measure the spurious response (section 7.3). Assuming the spurious response is common in the the blind KIDs and the FP KIDs the blind KID can be used to correct for the spurious response present in the MKIDs.
- **Broadband KIDs** Each FP resonator is, before the first FP coupler, coupled to a broadband KID. These KIDs thus measure the signal which arrives at the FP resonator and can be used to probe the power reaching the FP resonator.
- **Pure KIDs** The chip contains pure NbTiN KIDs which can be used to check the material properties at microwave (GHz) frequencies. These KIDs do not absorb power so the response depends only on the material properties of the resonator.

7.3. Spurious response

Part of the signal power absorbed in the aluminium strip of the MKID located behind the Fabry-Pérot resonator is coupled indirectly: This stray light does not couple to the MKID via the antenna and the FP, but is coupled via the holder or the chip directly as sketched in Fig. 7.3. The power absorbed in the MKID can be described by

$$P_{FP} = P_{top}(f)\eta_{QO}(f)\eta_{opt}(f)\eta_{FP}(f) + P_{top}(f)\eta_{QO}(f)\eta_{stray}(f) \tag{7.1}$$

with P_{FP} the power absorbed in the FP KID, P_{top} is the power in the transmitted toptica signal, η_{QO} is the quasi optical efficiency from toptica source to the chip level in the cryostat, η_{opt} is the coupling efficiency to the lens antenna, and η_{stray} describe how well the stray light signal originating from the toptica source couples directly to the KID line. The in-line Fabry Perot resonator introduces the η_{FP} term which describes the amount of power transmitted through the resonator, which is given by $|S_{21}|$ as described in chapter 4 and Fig. 4.3. The first term in (7.1) is referred to as the direct response and the second as the spurious response.

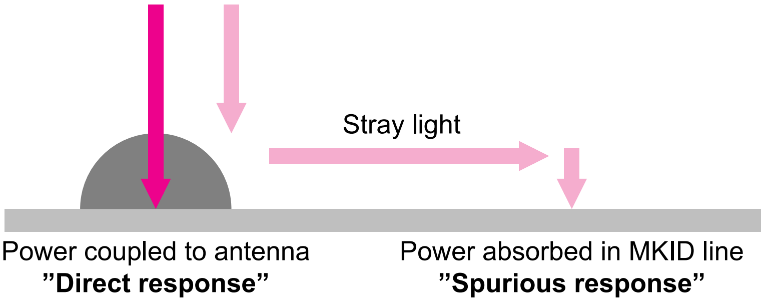

Fig. 7.3: Graphical representation of the spurious response contribution. Part of the power arriving at the chip is not coupled to the antenna but travels along the chip as stray light which can be absorbed in the MKID line giving rise to the spurious response of the MKID.

7.4. Two lens set-up

The ratio between the direct response and spurious response is mainly determined by (section 7.3)

$$\frac{\text{direct response}}{\text{spurious response}} = \frac{\eta_{opt}}{\eta_{stray}}. \tag{7.2}$$

This ratio can be improved by reducing the stray light coupling, i.e. through the 'maze' as in Fig. 7.2, or by improving the optical coupling to the chip. The optical coupling, η_{stray}, can be improved by matching the beams from the toptica source and the lens antenna with a two lens set-up. A graphical representation of the set-up is given in Fig. 7.4. Matching the two beams with the lens set-up not only increases the optical coupling η_{opt}, but decreases the stray light coupling η_{stray} as well. The stray light coupling η_{stray} decreases since one of the origins of the stray light is a mismatch between the incoming radiation and the lens antenna,due to which the power is reflected instead of coupled to the antenna.

The opening angle θ_o of the cryostat set-up can be changed by changing the size of the aperture at the 50K stage. The opening angle θ_o should match the beam size of the lens antenna. There are two options to match the opening angle θ_o to the beam of the leans antenna, place θ_o at the first null of the beam pattern or at a certain level from the maximum of the pattern i.e. the $-3dB$ level of the pattern. The farfield beam pattern of the 350 GHz and the 650 GHz lens antenna are given in Fig. 7.5 The antennas for both frequencies use identical dielectric lenses. The pattern for the 650 GHz is more directive since the size of the lens is, in terms of wavelengths, larger for this frequency compared to 350 GHz. The 50K aperture sizes corresponding θ_o matching the first null of the pattern or the $-3dB$ level are given in Table 7.2.

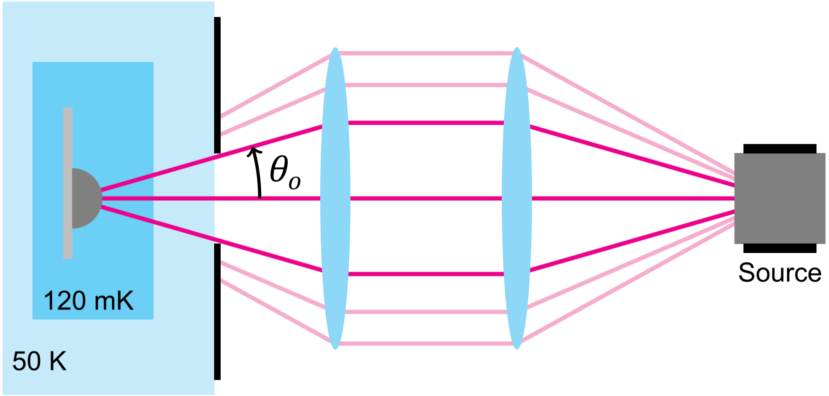

Fig. 7.4: Simplified view of the two lens set-up. The opening angle of the cryostat θ_o is determined by the size of the aperture at the 50K stage. The two lenses create a collimated beam increasing the coupling efficiency between the toptica source and the twin slot lens antenna on the chip.

Table 7.2: Aperture sizes for the first null and the $-3dB$ point of the lens antenna pattern. The angle θ is with respect to 0, see Fig. 7.4 and 7.5. d is the diameter of the required aperture in mm.

	θ_{null}	d_{null}	θ_{-3dB}	d_{-3dB}
350 GHz	30°	78.6 mm	13°	31.4 mm
650 GHz	17°	41.6 mm	7°	16.7 mm

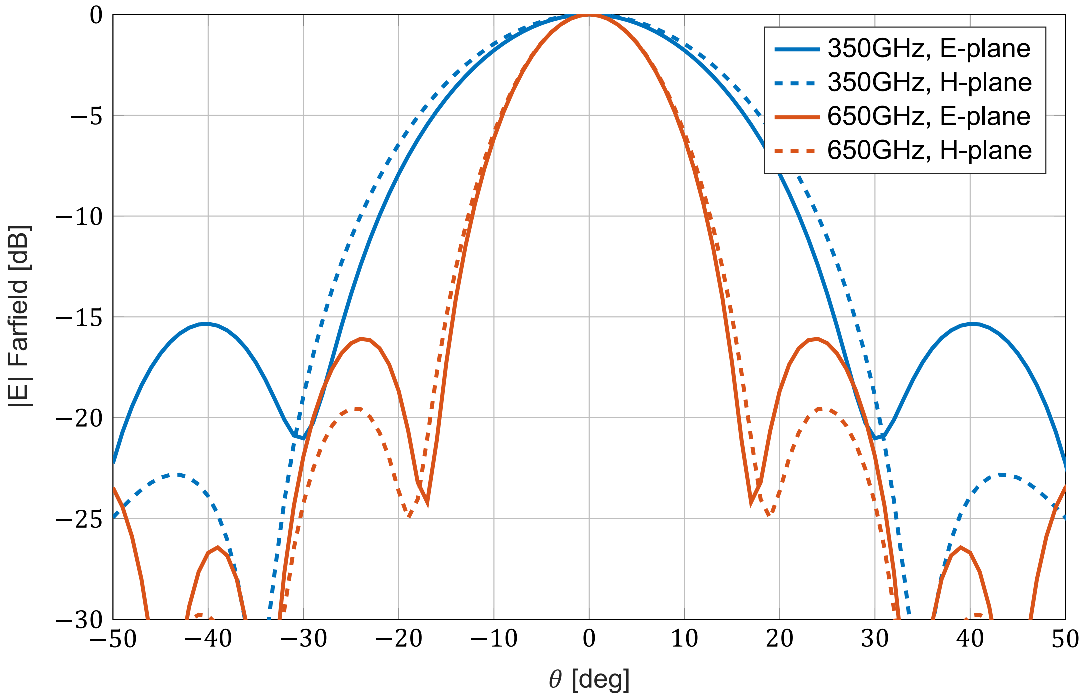

Fig. 7.5: The farfield patterns in E-plane and H-plane for the twin slot lens antenna configuration. The pattern is given for the 350GHz and the 650 GHz design. The pattern is given in the farfield of the lens-antenna system.

7.5. Measuring Q_i

This section discusses three approaches which can be used to measure the Q_i value of a FP resonator.

7.5.1. Q_i limited approach

The first approach is to design the FP resonators to be Q_i limited. When $Q_c >> Q_i$ the loaded quality factor Q_l of the resonator is limited by Q_i.

The advantage of this method is the simple analysis. The loaded quality factor Q_l, which is approximately the intrinsic loss Q_i in this case, is found with a Lorentzian fit of the resonance peaks, see Fig. 5.1 and (5.16)

$$Q_l = \frac{f_0}{BW_{-3dB}} \approx Q_i. \tag{7.3}$$

The disadvantage of this method is that it requires extremely high Q_c couplers to measure high Q_i values, e.g., for a-Si dielectrics. This gives rise to multiple problems:

- Limited frequency resolution of the source used for the experiment. The current experimental set-up cannot sample, due to the resolution of the source, resonator peaks with a Q_l over 30.000. This makes the Q_i limited approach unsuitable for dielectrics with an high expected Q_i e.g., a-Si with an expected Q_i ranging from 10^3 to 10^5.
- Since $|S_{21,max}|$ is given by Q_l/Q_c the relative transmission peak height becomes small when Q_c is large compared to Q_i (Fig. 7.6). It is difficult to measure transmission peaks with small relative peak heights as they will be lost in the different noise sources in the system.

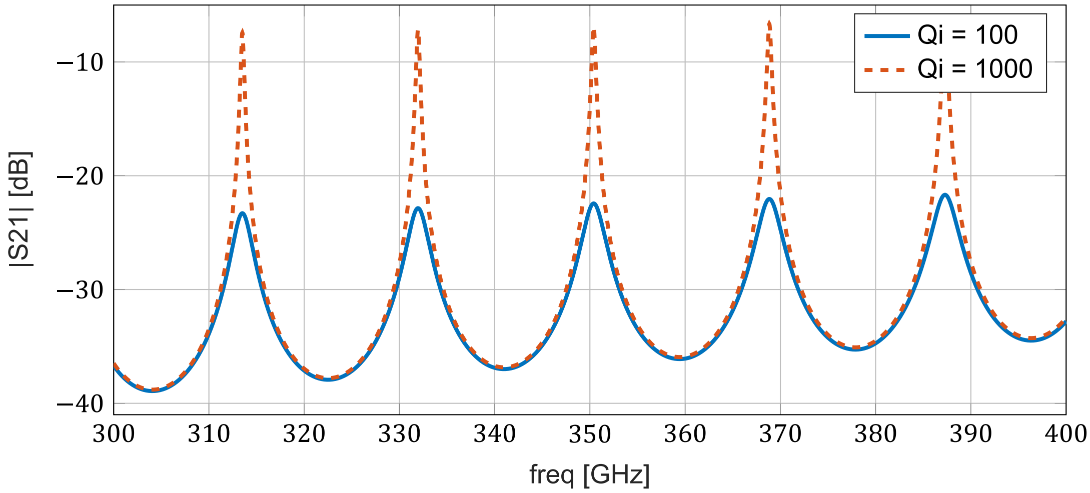

Fig. 7.6: Polyimide microstrip resonator (7 mm) with $Q_c = 2000$ couplers.

- Uncertainty in the realised Q_c. Due to fabrication tolerances the realised Q_c will differ from the designed Q_c. The decrease in Q_c is large for small fabrication errors e.g., a misalignment error which changes the overlap by 1 μm changes the Q_c of the coupler by a factor two. At a certain point (7.3) no longer holds due to the decrease in Q_c. It is possible to eliminate the issue with Q_c uncertainties by going to a region where $Q_c \gg Q_i$. In this case a change in Q_c will no longer effect the measured Q_l as illustrated in Fig. 7.7 by the line for $Q_i = 10^3$.

7.5.2. Ql(Qc,Qi) curve approach

A second approach to find Q_i is to probe the Q_l vs. Q_c curve obtained with (5.2). Each Q_i value will give a different curve resulting in the continuous change visible in Fig. 7.7.

The curves in Fig 7.7 can be probed using multiple FP resonators with different Q_c values. Each FP resonator will give a different point on the curve from which the complete curve can be extrapolated. Since this curve is specific for a value of Q_i this approach can be used to measure Q_i of the dielectric material. This approach however requires the Q_c of the realised FP resonators to be known.

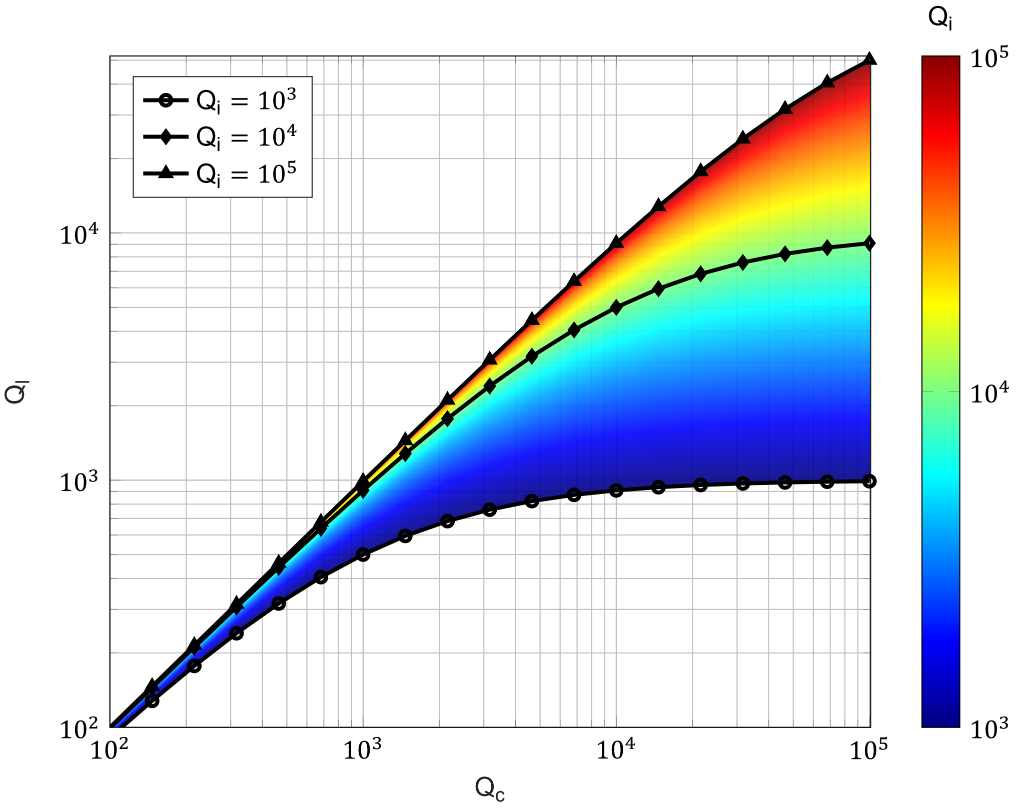

Fig. 7.7: Q_l vs. Q_c for different values of Q_i. Three curves are shown for $Q_i = 10^3$, $Q_i = 10^4$ and $Q_i = 10^5$. note that, for $Q_i = 10^3$, $Q_l \approx Q_i$ for high values of Q_c i.e. $Q_c \gg Q_i$.

7.5.3. Full $|S_{21}|$ curve approach

Although $|S_{21,max}|$ cannot be measured directly in a FP chip, due to uncertainties in the power coupling between source and MKID, the relative peak height of the resonator peaks can be used to measure Q_c (section 5.3). This approach is limited by the spurious response of the MKID, see section 7.3, which introduces a spurious response floor.

Below the spurious response floor the response of the MKID will be dominated by the spurious power absorbed in the MKID. This means that the part of the resonator curve that lies below the spurious response floor is not measurable (Fig. 7.8). From a previous experiment [46], designed to measure the radiation loss in a CPW line, the spurious response floor is estimated at -30dB.

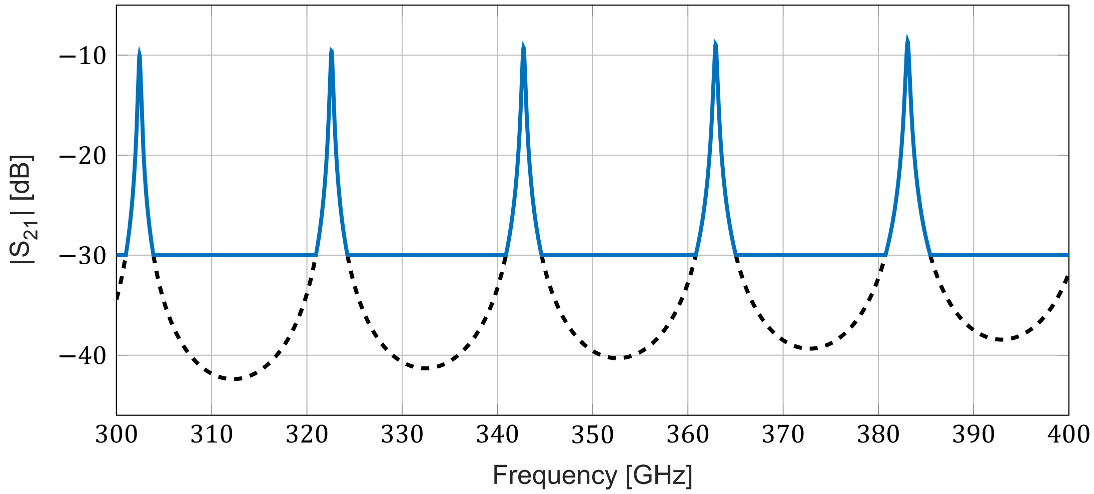

Fig. 7.8: Example of the spurious response dominated resonator curve. The spurious response limit is estimated around at $-30dB$. As the resonance peaks drop below $-30dB$ the response of the kid is dominated by the spurious response in the system instead of the direct response from the FP resonator.

To obtain the full curve each resonator has to be direct response dominated over the entire curve (Fig. 7.8). This means that the entire transmission curve of the resonator, $|S_{21}|$, has to lie above the spurious response floor.

Ignoring the losses, $\alpha = 0$ in (4.4), (4.5) becomes

$$\begin{bmatrix} A & B \\ C & D \end{bmatrix} = \begin{bmatrix} 1 & \frac{1}{j\omega C_k} \\ 0 & 1 \end{bmatrix} \begin{bmatrix} \cos(\beta l) & jZ_0 \sin(\beta l) \\ jY_0 \sin(\beta l) & \cos(\beta l) \end{bmatrix} \begin{bmatrix} 1 & \frac{1}{j\omega C_k} \\ 0 & 1 \end{bmatrix}. \tag{7.4}$$

At resonance $l = \frac{n\lambda}{2}$, with n the mode number. Off resonance, in the resonance dip, $l = \frac{(2n-1)\lambda}{4}$. The ABCD matrix for minimum transmission, sampled at the mode number n, is then given as

$$\begin{bmatrix} A & B \\ C & D \end{bmatrix} = \begin{bmatrix} 1 & \frac{1}{j\omega_n C_k} \\ 0 & 1 \end{bmatrix} \begin{bmatrix} \cos(-\frac{1}{2}\pi + n\pi) & jZ_0 \sin(-\frac{1}{2}\pi + n\pi) \\ jY_0 \sin(-\frac{1}{2}\pi + n\pi) & \cos(-\frac{1}{2}\pi + n\pi) \end{bmatrix} \begin{bmatrix} 1 & \frac{1}{j\omega_n C_k} \\ 0 & 1 \end{bmatrix} \tag{7.5}$$

where $\omega_n = 2\pi f_n = 2\pi n f_0$. The cos term is always 0, independent of the mode number n, and the sin term will be either 1 or -1 depending on the mode number.

$$\begin{bmatrix} A & B \\ C & D \end{bmatrix} = \begin{bmatrix} 1 & \frac{1}{j\omega_n C_k} \\ 0 & 1 \end{bmatrix} \begin{bmatrix} 0 & (-1)^n jZ_0 \\ (-1)^n jY_0 & 0 \end{bmatrix} \begin{bmatrix} 1 & \frac{1}{j\omega_n C_k} \\ 0 & 1 \end{bmatrix}. \tag{7.6}$$

with n the mode number and $\omega_n = 2n\pi f_0$ the resonance frequency of the peak corresponding to that mode number. Note that n in (7.6) gives the points at which the minimum transmission curve $|S_{21,min}|$ is sampled (ω_n) but does not influence the minimum transmission curve $|S_{21,min}|$. The term $(-1)^n$ in (7.6) does not influence the magnitude of transmission $|S_{21}|$. This means that the minimum transmission $|S_{21,min}|$ at a certain frequency f depends only on C_k and Z_0 and not on the length of the resonator.

Just looking at the magnitude of transmission $|S_{21}|$, (7.6) can thus be written as

$$\begin{bmatrix} A & B \\ C & D \end{bmatrix} = \begin{bmatrix} 1 & \frac{1}{j\omega C_k} \\ 0 & 1 \end{bmatrix} \begin{bmatrix} 0 & jZ_0 \\ jY_0 & 0 \end{bmatrix} \begin{bmatrix} 1 & \frac{1}{j\omega C_k} \\ 0 & 1 \end{bmatrix}. \tag{7.7}$$

which is now given for all ω and not just sampled at ω_n. In Fig. 7.9 the transmission curve $|S_{21}|$ obtained from (4.4) is plotted together with the minimum transmission curve $|S_{21,min}|$ from (7.7).

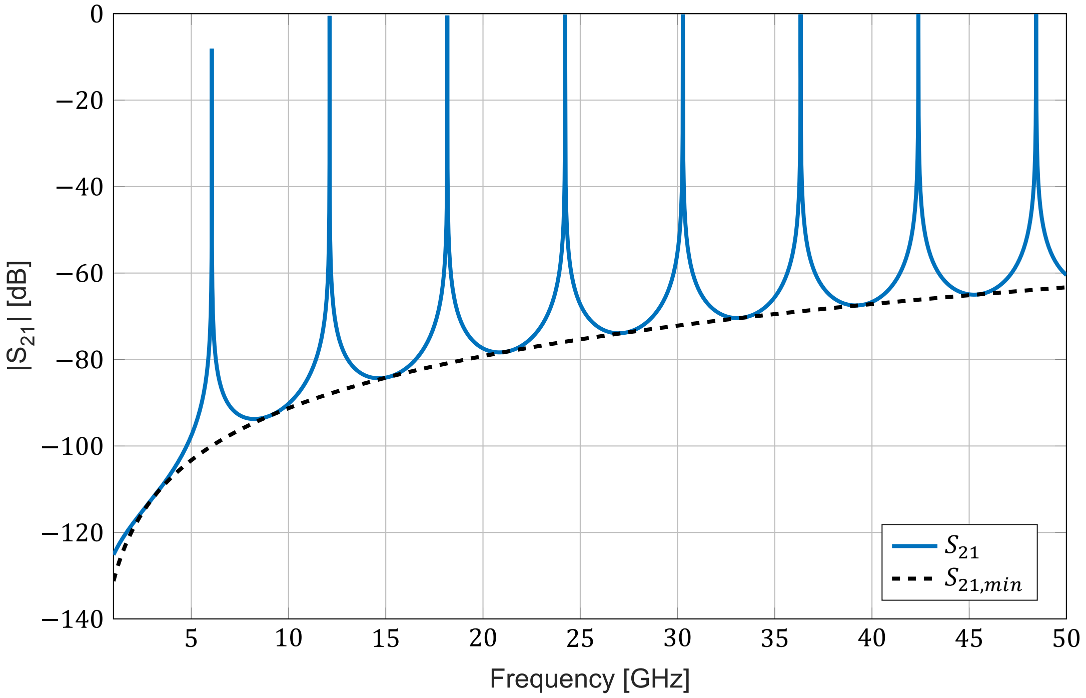

Fig. 7.9: $|S_{21}|$ resonator curve using the model of Fig. 4.1, and (4.4) together with $|S_{21,min}|$ from (7.7).

Obtaining a sufficiently high Q_c value requires a low coupling strength C_k which decreases the minimum transmission $S_{21,min}$ of the resonator. The other option to increase Q_c is to increase the length of the resonator which increases the mode number of the visible peaks as shown by (5.6)

$$Q_c = \frac{n\pi}{|S_{21,C_k}|^2}.$$

Combining (7.5) and (5.6), C_k can be selected such that desired minimum transmission $|S_{21,min}|$ is obtained. The desired Q_c value can than be reached by changing the length of the resonator. In this case all the couplers for a certain frequency band will be identical and the change in Q_c between resonators is made by changing the length of the resonator. An example of the effect of different resonator lengths for the same Q_c is given in Fig. 7.10.

Using the full $|S_{21}|$ curve the coupling quality factor Q_c of the resonator can be independently measured. Using the fitted Q_l of the lorenztian peaks and the measured Q_c of the full curve, Q_i can be determined from (5.5).

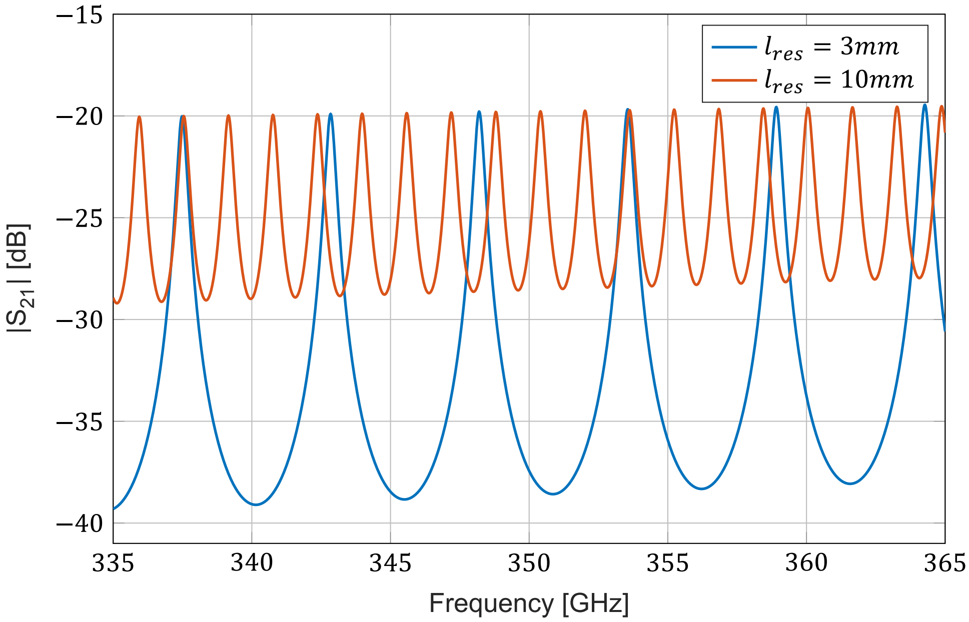

Fig. 7.10: Two different resonators with different resonator lengths l_{res} but equal Q_c. The shorter resonator, $l_{res} = 3mm$, requires a lower C_k to obtain the same Q_c since the mode numbers of the peaks are lower compared to the longer resonator (5.6). The lower C_k results in a lower minimum transmission $S_{21,min}$ (7.5).

8

Detailed design

The first section of this chapter summarizes the important results of chapter 7. It gives an overview of the different design parameters that are used for the design of the polyimide and a-Si chips given in this chapter.

8.1. Design space

The different resonators are mainly characterized by the coupling quality factor Q_c of their couplers. The coupling quality factor for an in-line resonator is given by (5.6).

$$Q_c = \frac{n\pi}{|S_{21,c}|^2}.$$

where n is the mode number and $S_{21,c}$ is the transmission trough the coupler. The mode number of a resonance peak at a certain frequency depends on the frequency spacing between the resonator peaks

$$n = \frac{f_n}{f_0} \tag{8.1}$$

where f_n is the frequency of the peak and f_0 is the frequency spacing between peaks. The frequency spacing between the peak f_0 depends on the length of the resonator

$$f_0 = \frac{c_0}{2l\sqrt{\epsilon_{eff}}} \tag{8.2}$$

It is clear that the coupling quality factor Q_c of the resonator can be changed by changing the length of the resonator l_{res} which shifts the frequency spacing f_0 and thus changes the mode number of the peaks in the measured frequency range. This is illustrated in Fig. 8.1.

The second parameter which influences Q_c is the capacitance of the coupler C_k. Changing the capacitance of the coupler C_k changes the transmission trough the coupler $S_{21,c}$, which in turn changes Q_c. The capacitance of the coupler not only changes Q_c, but also affects the minimal transmission level $|S_{21,min}|$ of the resonator (7.7). The change in minimum transmission is illustrated in Fig. 8.1 where Q_c is changed by changing the coupler capacitance C_k while keeping the resonator length constant.

The length of the resonator l_{length} and the capacitance of the coupler C_k are thus the two design parameters which can be used to change the coupler Q factor Q_c of the resonators. Table 8.1 summarizes the effect of both design parameters.

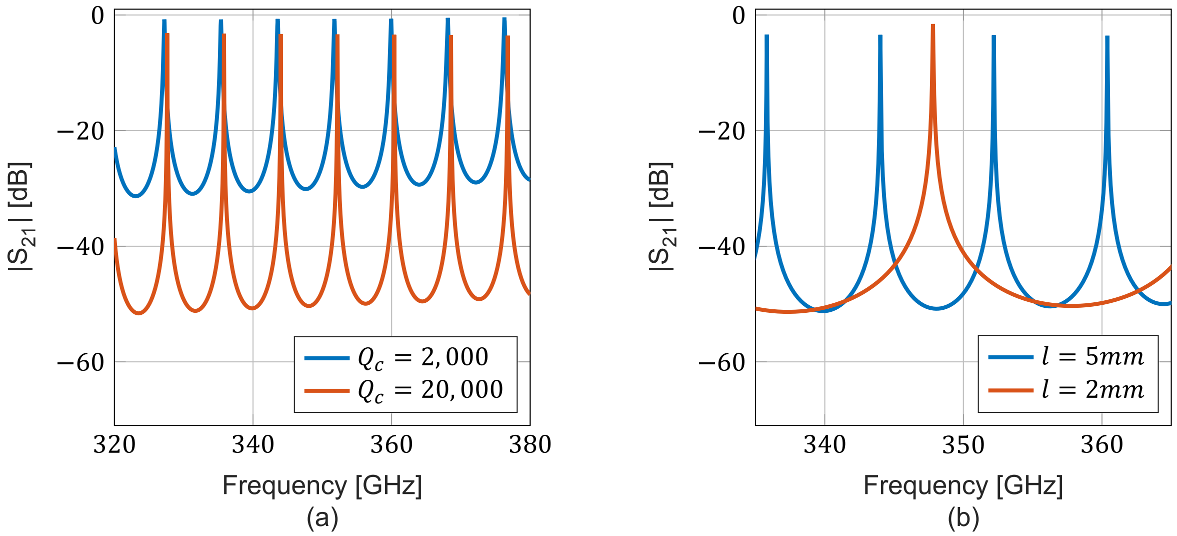

Fig. 8.1: Example of the change in $|S_{21}|$. **(a)** Increase in Q_c by decreasing the capacitance in the model of Fig. 4.1. The decrease in Q_c decreases $|S_{21,max}|$ and, since C_k decreases, $|S_{21,min}|$ **(b)** As the length of the resonator decreases the frequency spacing of the peaks f_0 increases. As discussed in table 8.1 this decreases Q_c which is visible in the slightly wider peak for the $l = 2mm$ resonator.

Table 8.1: Design space. The coupling quality factor Q_c can be changed by changing the mode number trough the resonator length l_{res}, or by changing the capacitance of the coupler C_k.

Parameter	**Effect**
C_k	The capacitance of the coupler C_k determines the frequency dependent transmission $|S_{21}|$ trough the coupler. Furthermore the capacitance of the coupler directly sets the minimum transmission level $|S_{21,min}|$ of the resonator (7.5).
l_{res}	The resonator length l_{res} changes the resonance peak spacing f_n. A change in f_0 changes the number of resonance peaks in the observed frequency range e.g., 300 GHz - 400 GHz, and thus changes the mode number n of the peaks within this range. Since the Q_c of a resonance peak depends on the mode number n of the peak (5.6), a change in resonator length changes the Q_c of the resonance peaks within the observed frequency range.

8.2. Couplers

The couplers need to be able to couple two CPW lines and to couple a microstrip line to a CPW line. An important constraint in the coupler design is that the Fabry-Pérot is coupled to a hybrid MKID. The MKID must be shorted at its narrow end, which is coupled to the Fabry-Pérot. This constraint has led to the two coupler design below:

The CPW to CPW coupler is realised by widening the central line of one of the CPWs such that it encloses the second CPW as in Fig. 8.2.

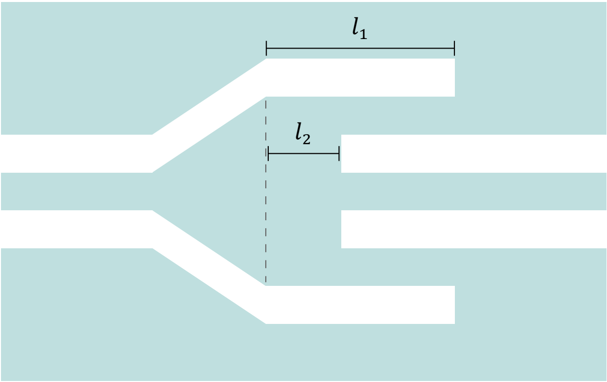

Fig. 8.2: CPW to CPW coupler. Metal is indicated in blue. The coupling strength can be varied by changing l_1 and l_2.

The coupling strength can be adjusted by increasing or decreasing the overlap of the two CPW lines.

The microstrip to CPW coupler is a 3D structure in which the microstrip is extended unto a shorted CPW line, which creates a capacitive coupler between the microstrip and the centre line of the CPW. A top- and side view of the coupler structure is given in Fig. 8.3.

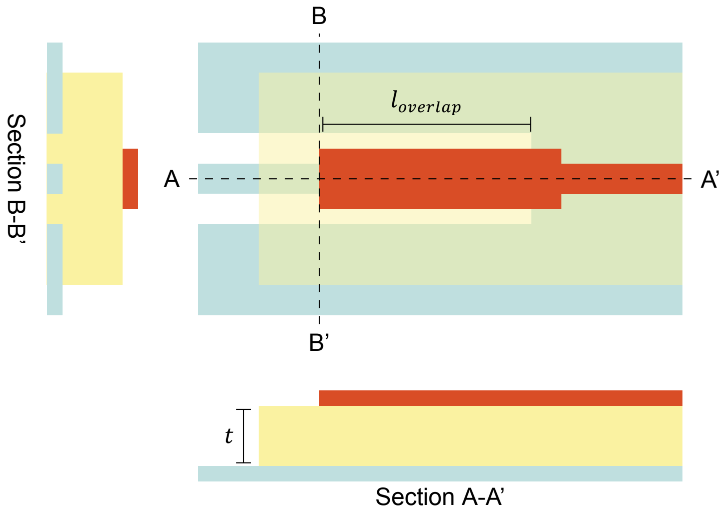

Fig. 8.3: microstrip coupler. CPW layer is indicated in blue, microstrip layer in red and dielectric layer in yellow. The coupling strength can be varied by changing the overlap between the two lines ($l_overlap$).

If, during the etching step of the manufacturing process, the overlapping microstrip section becomes wider or thinner than designed the coupling strength will change.

If the microstrip line would be as wide as the central line of the CPW a decrease in the microstrip width decreases the overlap area decreasing the coupling strength. overlapping the microstrip unto the CPW ground plane creates additional parallel plate capacitors which allow for energy to be coupled into the CPW ground plane decreasing the coupling strength between the lines.

A relatively stable coupling strength is obtained when the microstrip extends halfway unto the gaps of the CPW, Fig. 8.4. In this case the width of the microstrip can deviate from the designed value, up to a certain limit, without strongly decreasing the capacitive coupling between the microstrip and CPW central line or overlapping the microstrip unto the CPW ground planes.

Furthermore this geometry provides stability against misalignment errors in the lateral direction. As long as the lateral misalignment error is not greater than half the width of the CPW gap (G) the microstrip will still completely overlap width the central line of the CPW and will not overlap with the ground plane of the cpw.

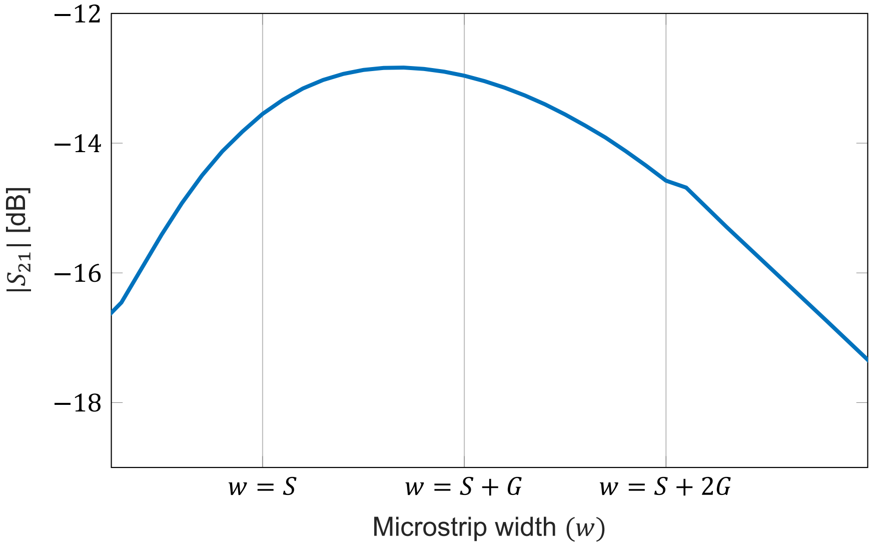

Fig. 8.4: Effect of the microstrip width on $|S_{21}|$. w is the width of th overlapping micorstrip, S the width of the CPW central line and G the width of the CPW gaps. At $s = W$ the microstrip and the CPW central line have the same width, for $w = S + G$ the microstrip extends halfway unto the gaps of the CPW and for $w > S + 2G$ the microstrip extend unto the ground planes of the CPW. The figure shown is for 350 GHz, $S = 2\mu m$, $G = 2\mu m$ and a $1\mu m$ thick dielectric

The couplers are designed using Sonnet EM [30], in which the transmission trough the coupler S_{21} is calculated as a function of the coupler geometry. Using (5.6), Q_c is obtained from $|S_{21}|$ of the coupler and the estimated mode number. The coupler are designed for the central frequency of the frequency bands e.g., 350 GHz for the 300-400 GHz band.

8.2.1. Designed vs. fabricated coupler

The fabricated coupler will deviate from the designed coupler due to:

- A difference in coupler geometry. The fabricated coupler won't have the exact same geometry as the designed coupler due to the limited accuracy of the etching steps, e.g. the width of the realised microstrip line will differ from the designed width.
- A difference in film properties. The properties of the superconducting films, the critical temperature T_c and the sheet resistance R_s, used for the design steps are approximations of the values for the deposited films. The values for the deposited films will differ, especially in the presence of the deposited dielectrics, from the approximated values.

The difference in geometry can be measured with a scanning electron microscope (SEM) with which the dimension of the fabricated coupler can be accurately measured. The difference in film properties can be measured with a DC chip which is included on the wafer in each production run. Using the DC chip the critical temperature T_c and the sheet resistance of the film can be measured. Using these measurements as inputs the fabricated coupler can be simulated, giving a better estimation of the realised Q_c value. This is still an estimation since the radiation loss in the coupler (section 5.2) and the uniformity of the films are unknown.

8.3. Design of the polyimide chip

The polyimide (PI) chip is a proof of concept for the on-chip Fabry-Pérot experiment. Polyimide, in contrast with a-Si, can be deposited in-house The loss tangent for polyimide is specified as $1/200$ at a few GHz and at room temperature [15]. Assuming that the dielectric loss tangent might improve at sub-K temperatures and is constant over frequency the expected Q_i range is set as $100 - 1000$.

This proof of concept chip is designed to demonstrate the correct working of the FP experiment including the designed couplers. The CPW-CPW coupler has been used before [46] but the CPW-MS coupler is a new structure. For this reason the chip consists of 2 CPW resonators and 2 microstrip resonators. The line parameters are given in Table 8.2.

Table 8.2: Selected resonator lengths for all three resonator types: the Bare CPW, the CPW covered with a polyimide dielectric layer and the microstrip with a polyimide dielectric.

	Bare CPW	**Covered CPW (PI)**	**Microstrip**
Z_0	$91\ \Omega$	$87\ \Omega$	$107\ \Omega$
$\varepsilon_{eff,s}$	14.0	15.3	7.3
l_{line}	5 mm	5 mm	7 mm
f_0	8.0 GHz	7.7 GHz	7.9 GHz

For this experiment two Q_c are selected, $2,000$ and $20,000$. All of the couplers on a single chip have the same Q_c value, resulting in a $Q_c = 2,000$ and a $Q_c = 20,000$ chip. The Q_c of $2,000$ is selected to test the full curve approach (section 7.5) for which the entire curve lies above to spurious response floor. The other Q_c value, $Q_c = 20,000$, is selected such that $Q_c \gg Q_i$ in order to perform a Q_i limited measurement (section 7.5). The Q_i limited approach is used as a reference for the new full curve approach. Tables 8.3 and 8.4 give the resonator and coupler geometries of the CPW and microstrip lines. The design of the $Q_c = 20,000$ chip is given in appendix D.1.

For the $Q_c = 2,000$ chip one of the microstrip resonators is shorter, 3 mm instead of 7 mm, to increase the dynamic range in case of a low Q_i (Fig. 8.5). Using the shorter resonator, which increases the mode number of the visible peaks, a lower C_k can be used while still obtaining the desired Q_c. The lower C_k results in a lower minimum transmission $|S_{21,min}|$ which increases the dynamic range of the resonator transmission curve (section 8.1). This however means that the minimum transmission of this resonator will likely drop below the spurious response floor.

Table 8.3: Overview of the CPW FP and coupler parameters for the bare CPW and the CPW covered with a ployimide (PI) layer. Coupler dimensions are given as in Fig. 8.2.

	$\mathbf{l_{resonator}}$	$\mathbf{f_0}$	$\mathbf{l_1}$	$\mathbf{l_2}$
Bare $Q_c = 2.000$	5 mm	8.0 GHz	9.1 µm	0.0 µm
PI $Q_c = 2.000$	5 mm	7.7 GHz	8.5 µm	0.0 µm

Table 8.4: Overview of the CPW to microstrip coupler geometries. Coupler dimensions are given as in Fig. 8.3.

	$\mathbf{l_{resonator}}$	$\mathbf{f_0}$	$\mathbf{l_{overlap}}$
$Q_c = 2.000$	7 mm	7.9 GHz	39.3 µm
$Q_c = 2.000$	3 mm	18.5 GHz	28.4 µm

Using the model described in chapter 4 the expected resonance curves are given in Fig. 8.5 for a Q_i of 200 and 1000.

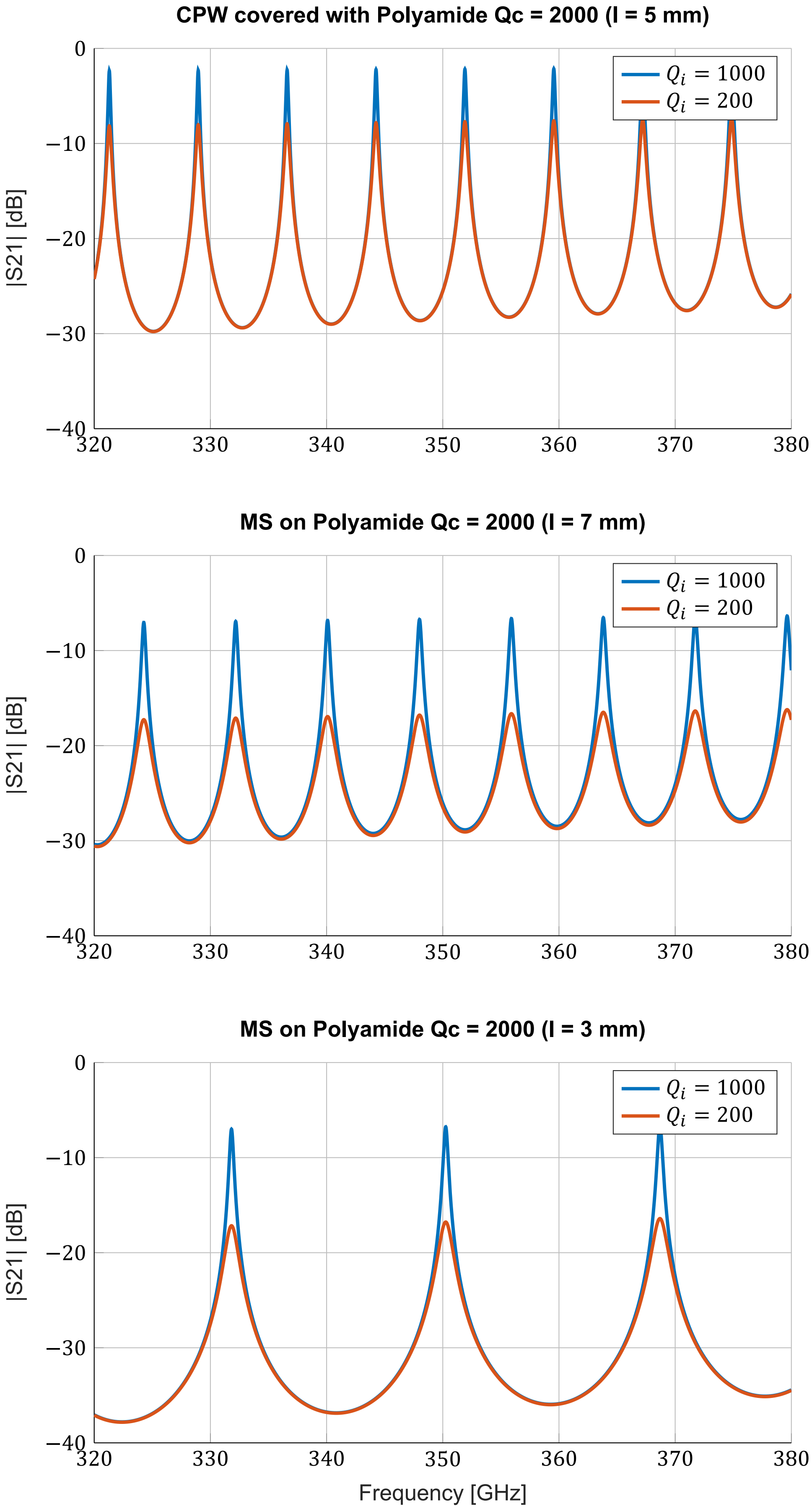

Fig. 8.5: Expected Resonance curves for the 300-400 GHz polyimide FP resonators. Note that the pure CPW line, which does not include any polyimide in the line geometry, is excluded in this figure since the Q_i of this resonator is not determined by the dielectric losses.

8.4. Design of the amorphous silicon chip

Table 8.5: Overview of the expected a-Si dielectric Q_i factor and the measurement frequencies.

	Amorphous silicon (a-Si)
Expected Q_i range	10^3 - 10^5 [16]-[18]
Measurement freq. f_1	350 GHz
Measurement freq. f_2	650 GHz
Measurement freq. f_3	850 GHz

The a-Si chip is designed for the frequencies and expected Q_i range given in Table 8.5. For each frequency the measurement is performed in a 100 GHz band centred around the specified frequency. This experiment will consist of multiple microstrip resonator chips, each for one of the different frequency bands.

Each of the chips will contain 4 microstrip FP resonators created on amorphous silicon. The coupler capacitance C_k of all the couplers for a chip are designed such that the entire resonance curve lies above the spurious response floor (7.5). This means that all the couplers in a chip will be identical. The length of each resonator l_{res} is then selected to obtain the desired Q_c values.

Due to the limited frequency resolution of the toptica source (>10 MHz section 7.2) peaks with a $Q_l > 30.000$ cannot be resolved. Using the highest expected Q_i value, 10^5, this results in a maximum Q_c value of 40.000. The minimum Q_c is selected such that the difference between the different $Ql(Q_c, Q_i)$ curves (section 7.5) is resolvable. This results in the selected Q_c values for the resonators given in Fig. 8.6.

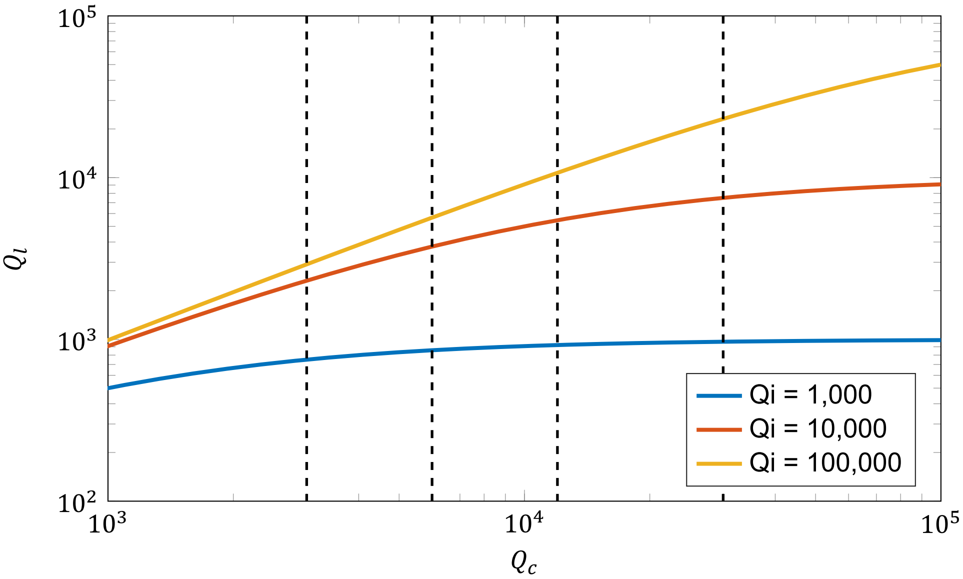

Fig. 8.6: The selected Q_c values for the microstrip resonators. The lowest Q_c value is selected such that the difference between the curves can be resolved. The highest Q_c is selected as 30.000

As a back-up the experiment contains CPW chip designed for 350 GHz. Two of the CPW resonators are deposited on a a-Si layer and two are deposited directly on the wafer. The wafer can be considered losless so the dielectric losses are only present in the two a-Si CPW lines. All four of the resonators will have identical couplers which, since the dielectric constant of a-Si is close to that of the wafer, will result in equal Q_c values. For the resonators without a-Si $Q_i >> Q_c$ and thus the loaded quality factor will be limited to Q_c, $Q_l \approx Q_c$. The lorentzian shape of the resonance peaks thus gives a measurement of the coupling quality factor of the resonators. Since the couplers for all four resonators are identical this measurement also holds for the a-Si couplers. Using the measured Q_c and the measured Q_l of the a-Si resonators Q_i can be determined.

Although the CPW chip gives a measurement of Q_i of the a-Si layer, the goal of the experiment is to measure Q_i of a-Si in a microstrip configuration. In the microstrip configuration the dielectric is deposited on top of a metal layer, and in turn a metal layer is deposited and etched on top of the a-Si layer. Both processes might affect the losses in the a-Si layer, it is thus key to measure the losses in the exact microstrip geometries which matches the eventual use case: the filters for DESHIMA and the feeding network for MOSAIC. This is why the CPW chip is used as a backup, and possibly to check the differences in the losses between a CPW geometry and a microstrip geometry.

The transmission line parameters for all lines, the CPWs and microstrip, are given in Table 8.6.

Table 8.6: Overview of the a-Si FP resonator transmission line properties. The a-Si layer is 250 nm thick, the micorstrip is 2 μm wide and the CPW is 2-2-2 μm.

	Microstrip	**CPW**	**CPW on a-Si**
Z_0	24.2Ω	93.0Ω	94.6Ω
ε_{eff}	46.84	13.7	13.2

The design of the microstrip FP resonators for each frequency band is given in Table. D.3. Note that the shortest resonator, with the largest frequency spacing f_n, still has at least 5 resonance peaks within the 100 GHz frequency band.

Table 8.7 gives an overview of the microstrip resonators designed for the 350 GHz chip. The design for the 650 GHz and 850 GHz chips is given in appendix D.2. The overlap of all the couplers in a single frequency band is identical to obtain the desired coupler capacity C_k, the desired Q_c is obtained by changing the length of the resonators (section 8.1).

Table 8.7: Overview of the microstrip FP resonator design for the a-Si experiment. Each frequency band f is a different chip with four resonators. Coupler dimensions are given as in Fig. 8.3.

$\mathbf{f}$	$\mathbf{Q_c}$	$\mathbf{l_{resonator}}$	$\mathbf{f_0}$	$\mathbf{l_{overlap}}$
300 - 400	$3,000$	4.0 mm	5.48 GHz	15.0 μm
	$6,000$	8.0 mm	2.74 GHz	15.0 μm
	$12,000$	16.0 mm	1.37 GHz	15.0 μm
	30.000	40.0 mm	0.55 GHz	15.0 μm

Using the methods described in chapter 4 the complete resonance curve $|S_{21}|$ of the FP resonators as given in Table 8.7 is modelled. The result is given in Fig. 8.7 for a 10 GHz range centred around the centre frequency of each band. The resonance curves for the 650 GHz and 850 GHz chips are given in appendix D.2.

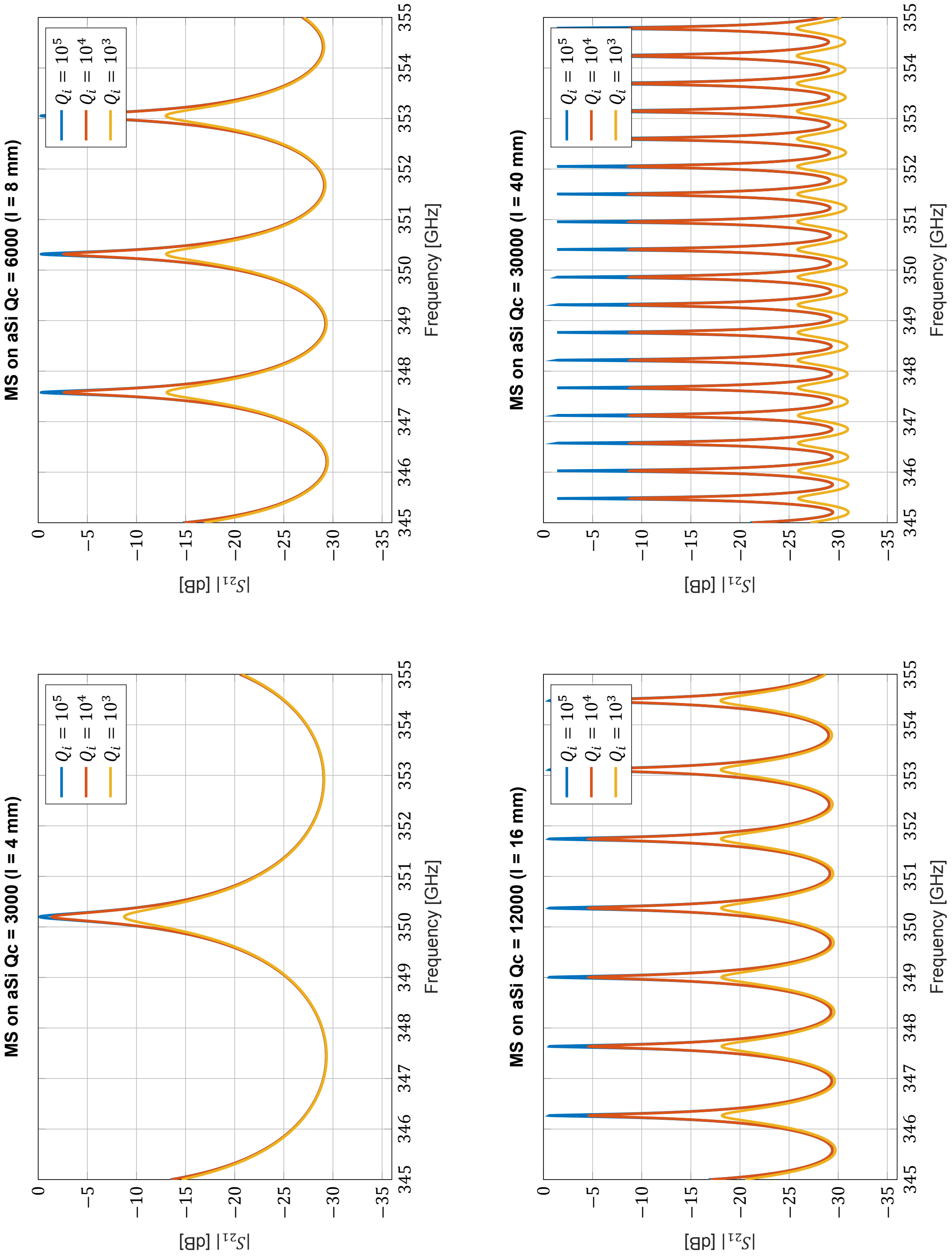

Fig. 8.7: Resonance curves for the 300-400 GHz microstrip FP resonator.

8.5. Fabrication

For the fabrication of the chips used in this experiment two fabrication flows can be defined. The first, referred to as the ”normal” approach, is illustrated in Fig. 8.8. In this process flow the ground plane is deposited in the wafer/substrate. The dielectric layer is then deposited on top of the ground plane and the microstrip is deposited on top of the dielectric. In this flow the antennas, THz lines, and MKIDs are etched into the groundplane, these structures are thus present, and exposed, when the microstrip is etched. To protect the ground plane layer during this etching step a resist layer is applied.

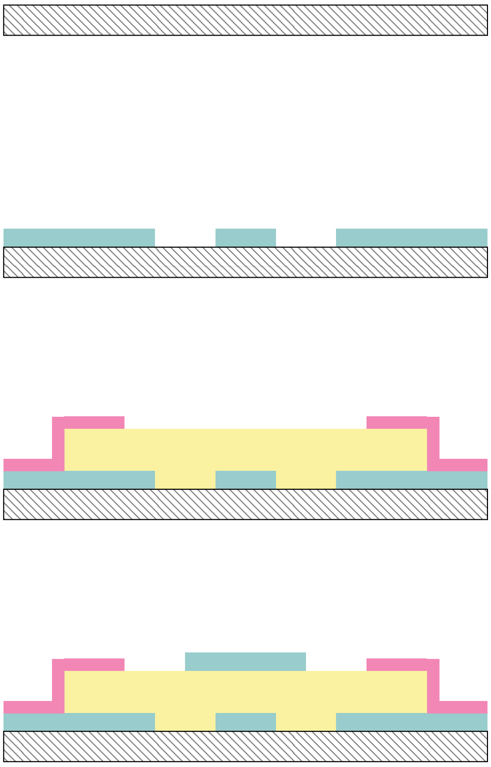

Start with sillicon wafer.

Deposit and etch NbTiN (layer: NbTiN bottom) into CPW geometrie.

Deposit and etch dielectric material. On top of the dielectric deposit and etch a resist protection layer. This layer protects the NbTiN layer during the following etching step.

Deposit and etch the NbTiN (layer: NbTiN top) microstrip line. The protection later protects the dielectric and NbTiN bottom layer during this etch step. The protection layer is removed after this step.

Fig. 8.8: Fabrication process referred to as the ”normal” approach. In this fabrication process the NbTiN microstrip line is deposited on top of the a-Si layer. A protection layer is used to protect the NbTiN ground plane during the NbTiN line etching step. This fabrication process is similar to the current process plan for the DESHIMA 2.0 chips, one of the project which requires the high Q_i dielectrics.

The second process flow is referred to as the ”inverted” microstrip. In this process flow the microstrip layer is deposited directly on the wafer. The dielectric layer is then deposited on the microstrip. The ground plane layer, containing the antennas, THz lines, and MKIDs, is then deposited on top. In this flow the ground plane layer is not subjected to the microstrip etching step, which is now one of the first etching steps, and the protection layer is thus not required. A graphical overview of the process flow is given in Fig. 8.9.

Unfortunately the ”inverted” microstrip process flow is not applicable for dielectric with a low dielectric constant e.g., polyimide with a dielectric constant of $\varepsilon_r = 2.9$ for which resonances inside the coupler are observed in the SONNET simulations. The polyimide chip is therefore fabricated using the ”normal” process flow. This problem does not arise for the a-Si layer of 250 nm.

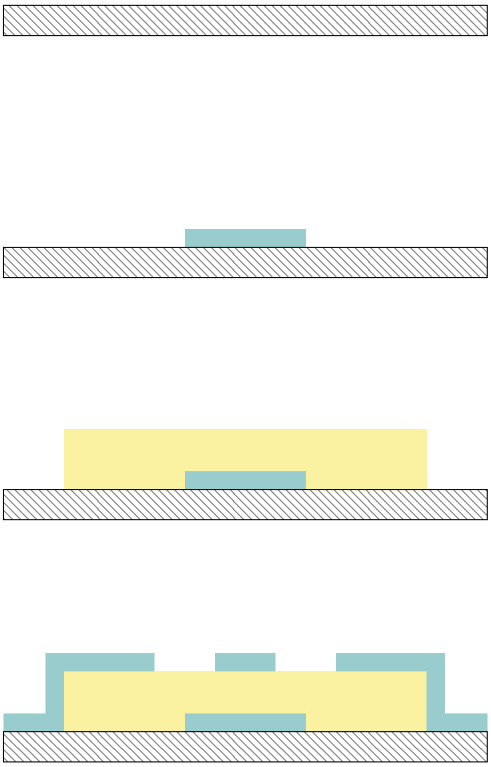

Start with sillicon wafer.

Deposit and etch the NbTiN (layer: NbTiN bottom) microstrip line.

Deposit and etch dielectric layer.

Deposit and etch the NbTiN (layer: NbTiN top) layer. This layer contains the CPW lines, the antenna, and the MKIDs.

Fig. 8.9: Fabrication process referred to as the ”inverted” approach. In this case the NbTiN microstrip line is buried beneath the a-Si dielectric layer and the NbTiN ground plane is deposited on top of the a-Si layer. This process flow removes the need for a protection layer during the last NbTiN etching step since the microstrip line is completely covered by the dielectric layer.

III

Measurements

9

Polyimide proof of concept measurements

9.1. Chip overview

The polyimide chip used for this measurement is described in section 8.3 and manufactured using the procedure described in Fig. 8.8. The chip contains four FP resonator KIDs each with a different resonator line configuration. The measured chip is a $Q_c = 2,000$ chip. An overview of the FP resonator lines is given in Table 9.1.

Table 9.1: Overview of the FP resonators on the $Q_c = 2000$ polyimide chip. Together with these 4 FP KIDs the chip contains 4 broadband KIDs, a blind KID and a pure NbTiN KID. Fill factor is as defined in section 5.2

KID ID	**Description**	$\mathbf{l_{resonator}}$	$\mathbf{f_0}$	**fill fraction**
FP 1	Bare CPW	5 mm	8.0 GHz	-
FP 2	CPW covered with polyimide layer	5 mm	7.7 GHz	15%
FP 3	Long polyimide microstrip	7 mm	7.9 GHz	60%
FP 4	Short polyimide microstrip	3 mm	18.5 GHz	60%

The expected resonance curves are given in Fig. 8.5 for a Q_i of 200 and 1000 [15]. Note that the pure CPW line, which does not include any polyimide in the line geometry, is excluded in this figure since the Q_i of this resonator is not dependent on the dielectric losses.

9.2. Data

After cooling the chip down to below the T_c of aluminium, $T = 240mK$, in the He3/He4 cryostat the response of the KIDs to a frequency sweep of the toptica source is measured. The result is given in the top panel of Fig. 9.1. In the top panel of Fig. 9.1 the frequency dependent transmission of the bandpass filter, centred around 350 GHz, is clearly visible. The response of the FP KIDs can be corrected with the blind KID,

$$Response_{corrected}(f) = \frac{Response_{FP}(f)}{Response_{Blind}(f)}, \tag{9.1}$$

of which the response follows the same bandpass behaviour and frequency dependency of the toptica source but doesn't include the FP resonator peaks. The result of the correction is given in the bottom panel of Fig. 9.1.

The frequency spacing of the FP peak visible in the response of FP 1 and FP 2 is roughly equal which matches the prediction from Table 9.1. The response of FP 3 doesn't show a clear FP resonator behaviour, there are some peaks visible but it's hard to discern them from additional peaks in the response. These secondary peaks are discussed in more detail in the next section. FP 4, the shorter MS line, shows a clearer FP resonator response with a larger frequency spacing compared to FP 1 and 2. Again this matches the prediction from Table 9.1.

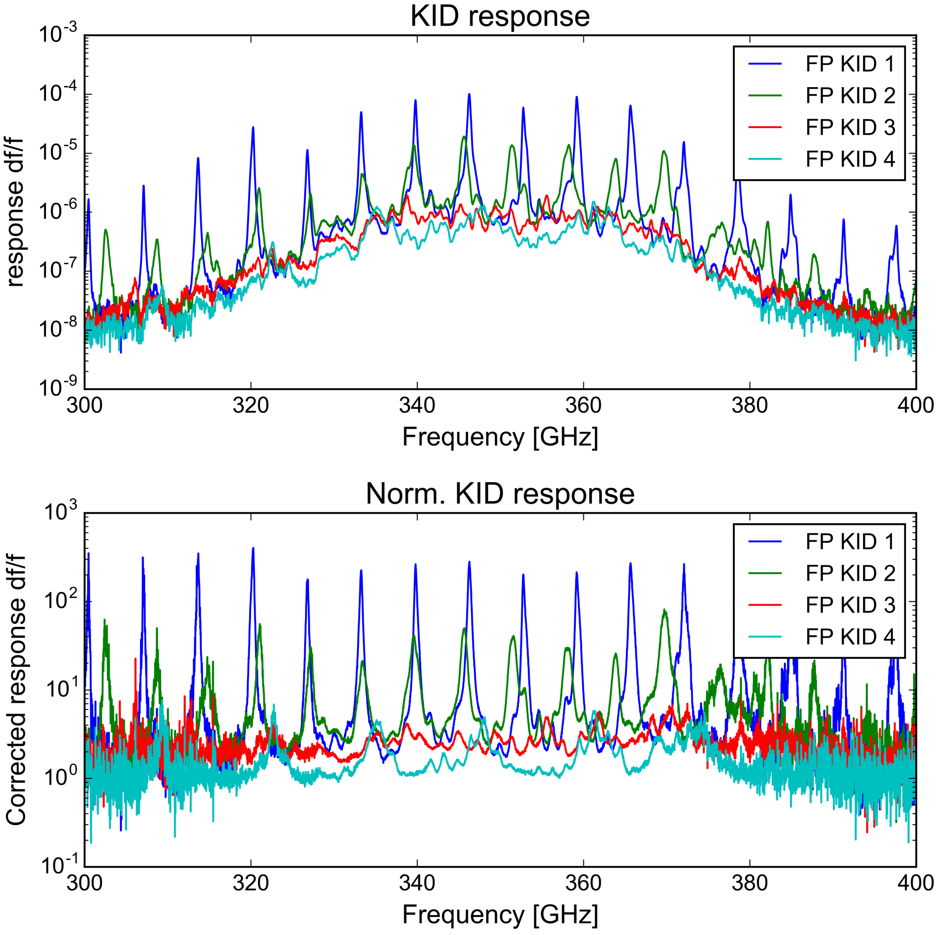

Fig. 9.1: Measured response for the $Q_c = 2000$ polyimide chip. **top)** The response for all four FP KIDs. **bottom)** The response normalised to the response of the blind KID. The numbering in the legend of this figure corresponds to the numbering in table 9.1.

The peak height of the FP peaks as a function of Q_c and Q_i is given by

$$S_{21,max} = \frac{Q_i}{Q_c + Q_i}. \tag{9.2}$$

For resonators with the same Q_c, the peak height will decrease with Q_i. The bare CPW resonator will have the highest Q_i since it doesn't suffer from dielectric losses, and should thus have the highest peak height. Due to the difference in fill fraction between the CPW and micro strip line the CPW resonator will have a higher Q_i than the microstrip resonators. The peak height should thus be highest for the bare CPW resonator (FP 1) and lowest for the microstrip resonators (FP KIDs 3 and 4) which is indeed observed in Fig. 9.1. The difference between FP KIDs 3 and 4 is the length of the resonator which changes the dynamic range of the resonance curve as shown in Fig. 8.5. This matches with the higher dynamic range observed in Fig. 9.1 for FP 4 compared to FP 3. It's thus reasonable to assume that the dominant peaks observed in the KID response originate from the FP resonators and that the measurement set-up is thus suitable for measurements and analysis of the FP peaks.

9.3. Analysis

The dielectric loss can be determined from the peaks in the response of FP KIDs 2, 3, and 4. The normalised response of these FP KIDs is given in Fig. 9.3 to Fig. 9.4 respectively. For all three resonators additional resonant peaks are visible on top of the expected FP transmission. While the amplitude associated with these peak is comparatively small, they clearly deform the FP resonance peaks. The frequency spacing of this additional resonance matches the length of the line from the lens-antenna to the first coupler of the FP. It is thus assumed that this second resonance arises due to, weaker, reflections between the lens-antenna system and the first FP coupler.

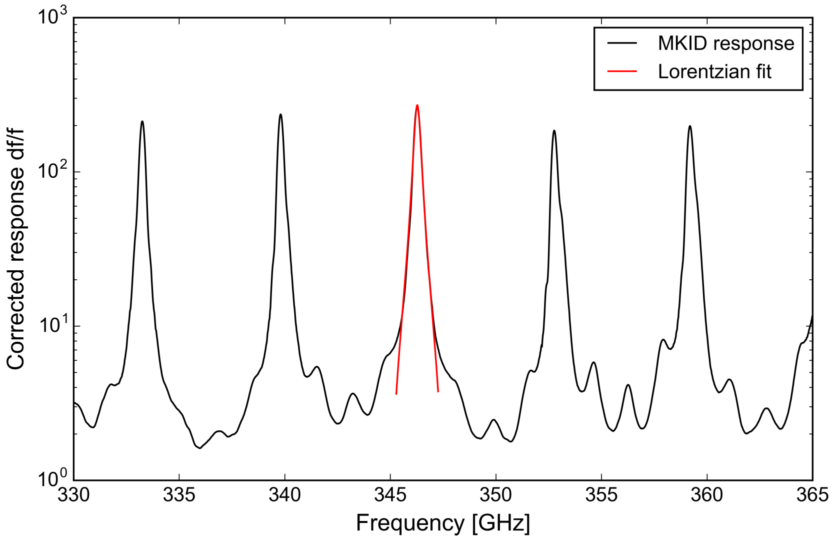

Fig. 9.2: Corrected response of FP KID 1. This KID is connected to the bare CPW FP resonator which does not contain any polyimide. The couplers for this chip are designed for $Q_c = 2000$.

The biggest problem that arises due to this additional resonance is that it can sharpen or broaden a FP resonance peak. This becomes a real problem when the resonance peaks are wide which corresponds to a low Q_i, such as the peaks for FP 4 (Fig. 9.4 and 8.5) where multiple of these secondary resonance lie within a single FP resonance peak. The distorted FP peak shapes cause an error in the lorentzian peak fitting leading to an error in the measured Q_l, as illustrated in Fig. 9.2 to 9.4.. The effect of the additional resonance is further explained in section 9.4

For FP 3, the 7mm long microstrip FP, the amplitude of the additional resonance is in the same order as the visible dynamic range of the FP resonance peaks. FP 3 is omitted in the analysis, instead the focus lies on FP 4 which is the same a-Si microstrip structure with clearer FP peaks in the KID response.

Regarding the spurious response floor, the dip depth of the normalised response of FP 2 lies at 2 in Fig. 9.3. The lowest response of the FP KID divided by the response of the blind KID results in a factor 2. This implies, since the blind KID is sensitive to the spurious response, that the lowest level of the resonance curve lies a factor 2 above the spurious response floor. It is however difficult to determine if the full FP resonance curve is captured due to the additional resonance present in the dip of the FP resonance curve.

The mean Q_l and frequency spacing f_0 for each FP resonator is obtained by fitting all FP peaks within the 330 to 365 GHz range. Examples of the fit used to obtain Q_l for each FP resonator are given in Fig. 9.2 to 9.4.

From the scanning electron microscope (SEM) and DC chip measurement (section 8.2) the superconductor properties, such as T_c, and the exact line dimensions are obtained. Using these as input the expected Q_c can be more accurately simulated since the deviation between designed and fabricated coupler is now partly known. Due to the non-uniformity of the films the film properties at the coupler will differ from the film properties measured at the DC chip. Furthermore the radiation losses inside the coupler (section 5.2) introduce an unknown deviation between the simulated and realised Q_c.

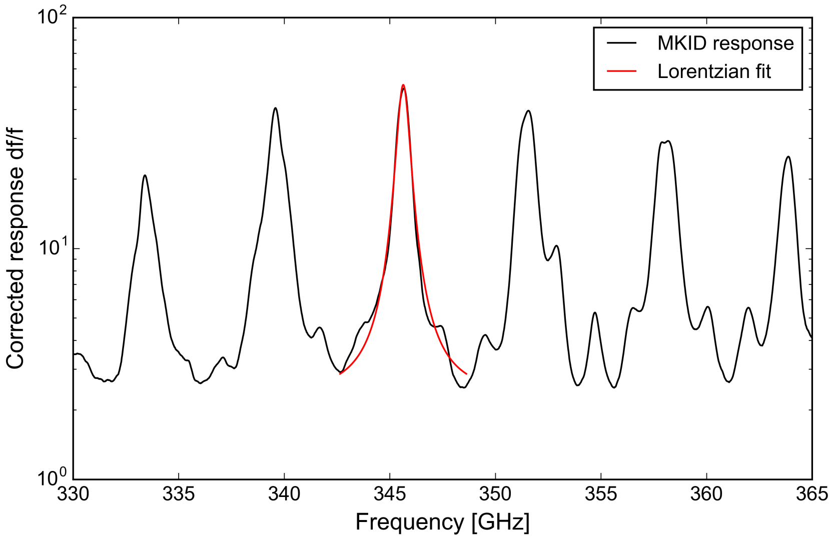

Fig. 9.3: Corrected response of FP KID 2. This KID is connected to the CPW covered with polyimide FP resonator. The couplers for this chip are designed for $Q_c = 2000$.

Combing the measured mean Q_l, simulated Q_c, and the fill factor using (5.2) and (5.13) results in Q_i for the dielectric

$$Q_{i,dielectric} = FF \times \frac{Q_c Q_l}{Q_c - Q_l}. \tag{9.3}$$

Table 9.2 gives the frequency spacing, mean Q_l, estimated Q_c, fill fraction, and the obtained Q_i.

The estimated Q_c value of the CPW-CPW coupler can be checked with FP 1. Since the resonator line is a pure NbTiN CPW without asi a $Q_i >> Q_c$ is expected. In this case $Q_l = Q_c$ and since there is small difference between the FP 1 and FP 2 couplers (Table 9.1) the measured Q_l of FP 1 should be in the same order as the expected Q_c of FP 2. Averaging over 5 FP peaks in the 330 GHz to 360 GHz range a mean Q_l of 1020 with standard deviation of 63 is obtained. With the assumption that $Q_c = Q_l$ this matches the simulated Q_c for FP 2.

Table 9.2: Overview of the results of polyimide chip. The Q_l and Q_i factors are given as a mean with a standard deviation, this mean is taken over the fitted Q_l of multiple peaks within the frequency window of 330 GHz to 365 GHz. The simulated Q_c uses the DC and SEM measurements to model the coupler as accurately as possible. The designed Q_c for this chip is 2000. The fill fraction (FF) is obtained as discussed in section 5.2.

KID ID	**Mean Q_l**	**f_0**	**Q_c**	**FF**	**$Q_{i,dielectric}$**
FP 1 bare CPW	1020 ± 63	6.3 GHz	-	-	-
FP 2 PI CPW	430 ± 66	6.1 GHz	1120	15%	108 ± 28
FP 4 PI MS	270 ± 106	13.0 GHz	2800	60%	182 ± 76

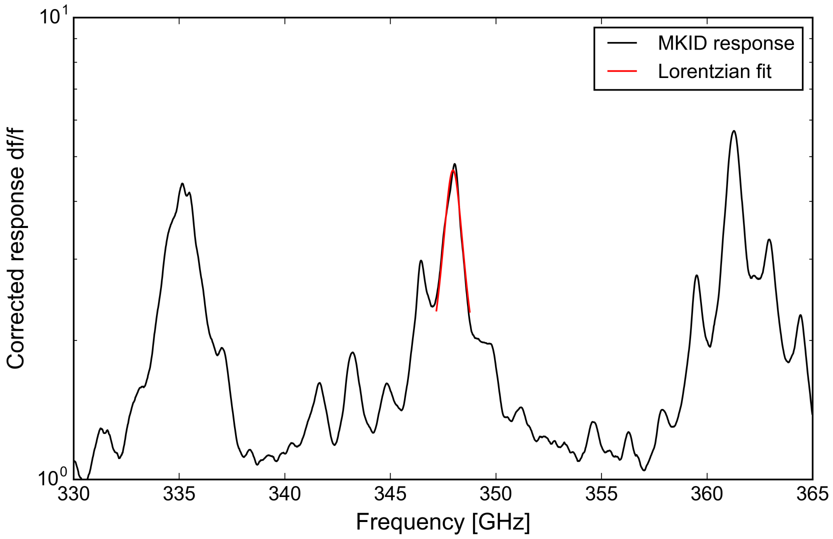

Fig. 9.4: Corrected response of FP 4. This KID is connected to a 3mm long microstrip FP resonator. The couplers for this chip are designed for $Q_c = 2000$. Note that the fit in this plot focusses on the primary peak in the presence of the additional response.

9.4. Secondary resonances

The effect of the secondary resonances visible in Fig. 9.3 can be modelled by including a section of transmission line, with a length longer than that of the FP resonator, before the first FP coupler in the ABCD matrix calculations. This results in

$$\begin{bmatrix} A & B \\ C & D \end{bmatrix} = \begin{bmatrix} \cosh(\gamma l_1) & Z_0 \sinh(\gamma l_1) \\ Y_0 \sinh(\gamma l_1) & \cosh(\gamma l_1) \end{bmatrix} \begin{bmatrix} 1 & \frac{1}{j\omega C_k} \\ 0 & 1 \end{bmatrix} \begin{bmatrix} \cosh(\gamma l_2) & Z_0 \sinh(\gamma l_2) \\ Y_0 \sinh(\gamma l_2) & \cosh(\gamma l_2) \end{bmatrix} \begin{bmatrix} 1 & \frac{1}{j\omega C_k} \\ 0 & 1 \end{bmatrix} \tag{9.4}$$

where l_1 is the length of the THz line, the line between the antenna and the first FP coupler, and l_2 is the length of the FP resonator. Transforming the resulting ABCD matrix into S_{21}, with a mismatched load at port 1, gives the modelled signal of Fig. 9.5a. The Q_l factor of the secondary resonance and the FP resonance will differ since the losses, Q_i, in the lines l_1 and l_2 will differ. Furthermore the secondary resonance arises due to reflections between a coupler and the lens antenna instead of reflection due to two coupler which means they will have a different Q_c, see section 5.1. Depending on their resonance spacings f_n and Q values multiple secondary resonances can fall within one FP peak affecting the shape of the FP peak, as in Fig. 9.5a. Alternatively multiple FP peaks can lie on a single secondary resonance in which case the relative peak height of the FP peaks will be affected and will follow the secondary resonance.

Using the modelled signal of Fig. 9.5a filtering techniques can be tested to see if it's possible to filter out the secondary resonance from the FP response. A simple method is to compare the spectrum, obtained trough the fourier transform of the signals, of the modelled signal to the spectrum of the FP signal and filter out the extra frequency components present in the modelled signal. Since the spectra of the FP response and the secondary response overlap, the peaks shapes are identical, suppressing or removing the extra frequency components inadvertently affect the FP response see Fig. 9.5b. Although the secondary resonance is suppressed the FP peaks in the filtered still differ, although less than for the unfiltered version, from the real FP peaks.

The filtering example, illustrated by Fig. 9.5, shows that the analysis can benefit from applying filtering techniques. The Q_l of the filtered peaks lies within 10% of the Q_l of the actual peak. The approach discussed in Fig. 9.5a is however not feasible since it requires a-priori knowledge on the exact shape, and thus Q values, of the resonator peaks. It requires a sufficient time investment to study the applicability and quality of different filtering techniques. This currently falls outside the scope of this thesis project so will be included in the recommendations at the end of this thesis. Furthermore the effect of the secondary resonance will likely be smaller for the a-Si chip due to the higher Q values of those FP peaks and the smaller frequency spacing f_0 (section 8.4).

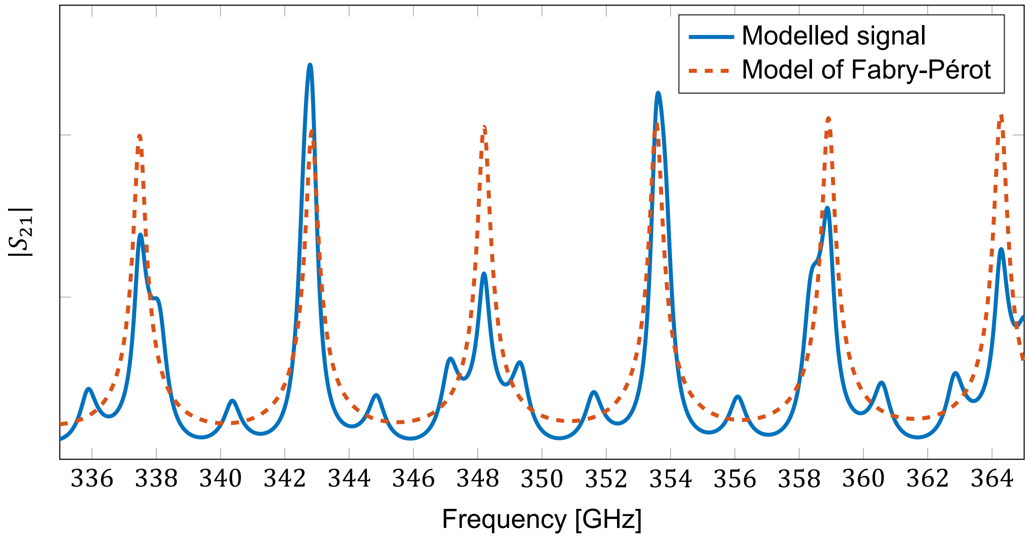

(a) Using the ABCD matrix method a section of transmission line can be added before the first FP coupler which models the secondary resonance present in the measured polyimide response. The modelled signal with the secondary resonance is plotted against the modelled FP response. It's clear that the secondary resonance deforms the FP resonance peaks.

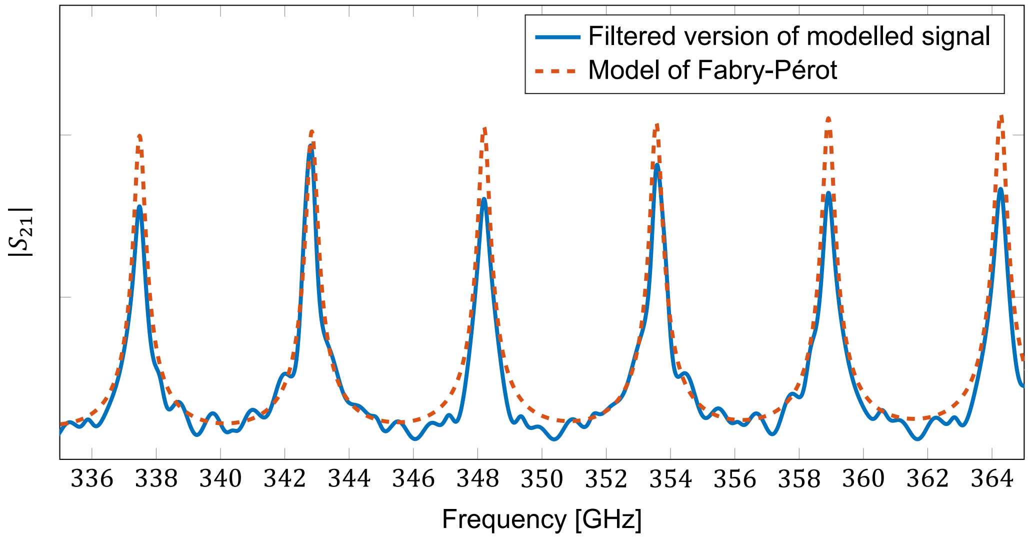

(b) The modelled signal can be filtered by comparing the spectrum of the modelled signal with the spectrum of the FP model and removing or suppressing the extra frequency components. Although the secondary resonance can be suppressed the exact shape of the FP peaks cannot be recovered and thus the fitted Q_l will differ from the actual Q_l of the resonator.

Fig. 9.5: The influence of the secondary resonance on the FP resonance peaks can be modelled trough the ABCD matrix approach by including an extra section of transmission line before the first FP Coupler, see 9.5a. Filtering the secondary resonance from the signal reduces the effect the secondary resonance has on the FP resonance peaks but the resulting peaks still differ from the real FP peaks, see Fig. 9.5b. Note that this approach is not a realistic approach since it requires a-priori knowledge on the exact FP curve.

9.5. Conclusion

The main objective of this polyimide chip was to proof the lab on a chip Fabry-Pérot concept. The results obtained with this chip, given in Fig. 9.3 and 9.4, clearly show peaks which can be attributed to the Fabry-Pérot resonator. The obtained Q_l and Q_i values are reasonably close to the $Q_i = 200$ value specified by the supplier of the polyimide for room temperature operation. Therefore it is concluded that the losses in polyimide do not improve when it is cooled down. It is thus concluded that the on chip Fabry-Pérot resonator works and can be used to measure the Q_i of dielectric materials.

One of the biggest concerns from the polyimide measurements is the large spread in fitted Q_l of the peaks. This spread is likely due to the FP peaks being deformed by the secondary resonances, resulting in FP peaks which cannot be fitted correctly. Finding a way to deal with the secondary resonances is thus required for accurate Q_i measurements. As mentioned in section 9.4 one option is to filter the measured signal to obtain the correct FP peaks. Implementing this filter requires a time investment which is not feasible within the scope of this thesis.

It might however be possible to largely circumvent the effect of the secondary resonance in the a-Si design as a-Si has much lower losses and therefore much sharper resonances. If the FP peaks are sharp compared to the secondary resonance peaks, e.g. have a higher Q, it’s impossible that multiple secondary resonances fall within one FP peak. In this case the peaks won’t be deformed as in Fig. 9.3 and 9.5a. Fortunately the design of the a-Si chip (section 8.4) involves higher Q resonators and it is thus likely that the a-Si chip will be less affected by these secondary resonances than the polyimide chip.

The response of FP 2, Fig. 9.3, likely lies just above the spurious response floor. It is however difficult to say this with absolute certainty since the dip of the FP response is invisible due to the secondary resonance.

10

a-Si measurements

10.1. Chip overview

The design of the a-Si is discussed in section 8.4. An overview of the relevant FP resonator design parameters is given in Table 10.1.

Table 10.1: Overview of the designed FP resonators for the a-Si chip as presented in section 8.4. The chip contains four identical microstrip FP resonators and a blind KID. The couplers used for all four FP resonators are identical, the only difference between the resonators is the length $l_{resonator}$

KID ID	$\mathbf{Q_c}$	$\mathbf{l_{resonator}}$	$\mathbf{f_0}$
FP 0	$3,000$	4.0 mm	5.48 GHz
FP 1	$6,000$	8.0 mm	2.74 GHz
FP 2	$12,000$	16.0 mm	1.37 GHz
FP 3	$30,000$	40.0 mm	0.55 GHz

Two versions of the a-Si were fabricated, one with the microstrip buried beneath the a-Si dielectric as in Fig. 8.9. During the fabrication process the a-Si dielectric layer was most likely subjected to stress from the substrate and the NbTiN layer covering the dielectric. The result was a chip with craters in the a-Si and NbTiN layer as in Fig. 10.1. The same process also affected the parts where the CPW KID readout is coupled to the pure microstrip resonators, where the a-Si is deposited on top of the SiN layer of the wafer and covered by the NbTiN layer of the CPW readout line. At these point the dielectric seemed to blister, creating breaks in the readout line. Due to the breaks in the readout line most chips in this process run are unusable.

As an alternative a second run is fabricated using the normal process of Fig. 8.8 where the microstrip line is deposited on top of the dielectric instead of being buried underneath the dielectric. Instead of using the protection layer as discussed in section 8.5 the NbTiN ground layer is made thicker to compensate for the over etch during the NbTiN etching step. The craters in the a-Si layer do no occur with this process flow. The measurements described in this section are performed with chips from the second process run where the microstrip line is deposited on top of the a-Si layer.

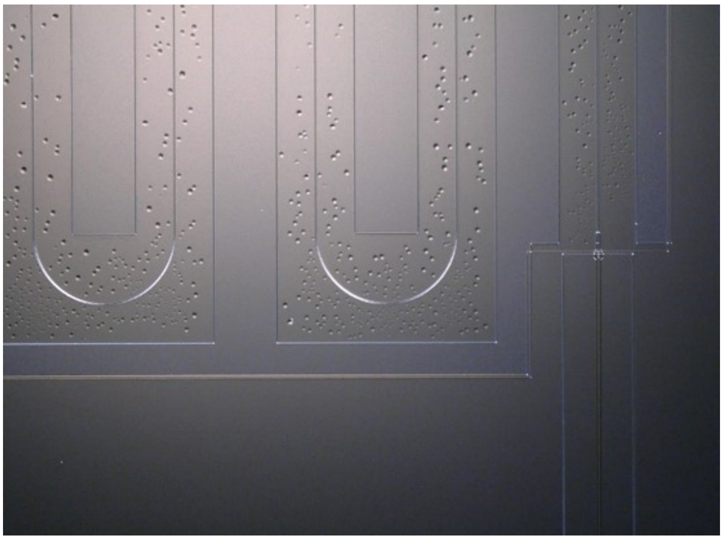

Fig. 10.1: Image from the a-Si chip fabricated using the inverted process from Fig. 8.9. Craters are clearly visible in the a-Si layer around the meandering NbTiN microstrip line.

10.1.1. DC chip

Each fabrication run contains a DC chip which used to measure the properties of the superconducting film. The measurements of the DC chip of the a-Si chip used for this experiment are given in Table 10.2. Using the sheet resistance R_s, critical temperature T_c, and thickness of the films the expected kinetic inductance L_k of the films is calculated. The expected kinetic inductance of the realised films is one of the inputs for the simulation of the realised, which likely differ from the designed, couplers.

The measured T_c of the NbTiN GND layer is much lower than expected. This indicates a film of poor quality which could introduces additional losses in the transmission line.

Table 10.2: Results of the a-Si DC chip. This chip contains several simple lines created in the different layers present on the chip. The superconducting properties of the different layers, such as the critical temperature T_c and the sheet resistance R_s can be measured. Using the measured film properties an accurate estimation of the kinetics inductance L_k can be made. The DC chips are measured in a adiabatic demagnetization refrigerator (ADR) cryostat at SRON Utrecht. The NbTiN GND (a-Si) layer has the a-Si layer on top and the NbTiN line layer (a-Si) has the a-Si layer below.

Layer	**t [nm]**	$\mathbf{T_c}$ **[K]**	$\mathbf{R_s}$ **[Ω]**	$\mathbf{L_k}$ **[μH]**
NbTiN GND	220	12.64	16.18	1.86
NbTiN GND (a-Si)	220	12.70	9.033	1.07
NbTiN line	150	14.99	11.42	1.12
NbTiN line (a-Si)	150	14.97	12.56	1.22

10.1.2. SEM results

Using a scanning electron microscope (SEM) accurate measurements of the coupler geometries on the chip are obtained. For the a-Si chip the following deviations from the designed geometries are observed:

- The CPW line has a line width of 1.49 µm and a gap of 2.67 µm on both sides instead of the designed 2 µm line and gap.
- The microstrip line has a width of 1.76 µm instead of the designed 2 µm.
- In the MS-CPW coupler geometry (section 8.2) the width of the overlapping microstrip section is 3.51 µm instead of 4.0 µm and the length is 15.97 µm instead of the designed 15 µm (Table D.3).

Using these dimensions the coupler is simulated, the resulting Q_c values are given in table 10.3.

10.1.3. Corrected overview

With the results from the DC chip and the SEM measurements the FP coupler is simulated again but with the geometry and kinetic inductance L_k corresponding to the fabricated coupler. This simulation results in corrected values for the expected Q_c and frequency spacing f_n, of which an overview is given in table 10.3.

Table 10.3: Corrected overview of the Q_c and frequency spacing f_n for the a-Si microstrip FP resonators and their corresponding KID ID. The given Q_c values are for the centre frequency of the band $f = 350GHz$.

KID ID	$\mathbf{Q_{c,designed}}$	$\mathbf{Q_{c,corrected}}$	$\mathbf{f_{0,corrected}}$
FP 0	$3,000$	$1,666$	4.67 GHz
FP 1	$6,000$	$3,332$	2.33 GHz
FP 2	$12,000$	$6,663$	1.17 GHz
FP 3	$30,000$	$16,660$	0.47 GHz

10.2. Analysis

For the a-Si experiment all measurements are performed with the two lens set-up of section 7.4. The analysis of the a-Si experiment is subdivided into multiple sections, each focussing on a particular step in the analysis path. The final result is an estimated Q_i value for the a-Si dielectric.

10.2.1. Raw response

Measurements were carried out at $T = 40mK$. The raw response of the four FP KIDs and the blind KID is given in Fig. 10.2.

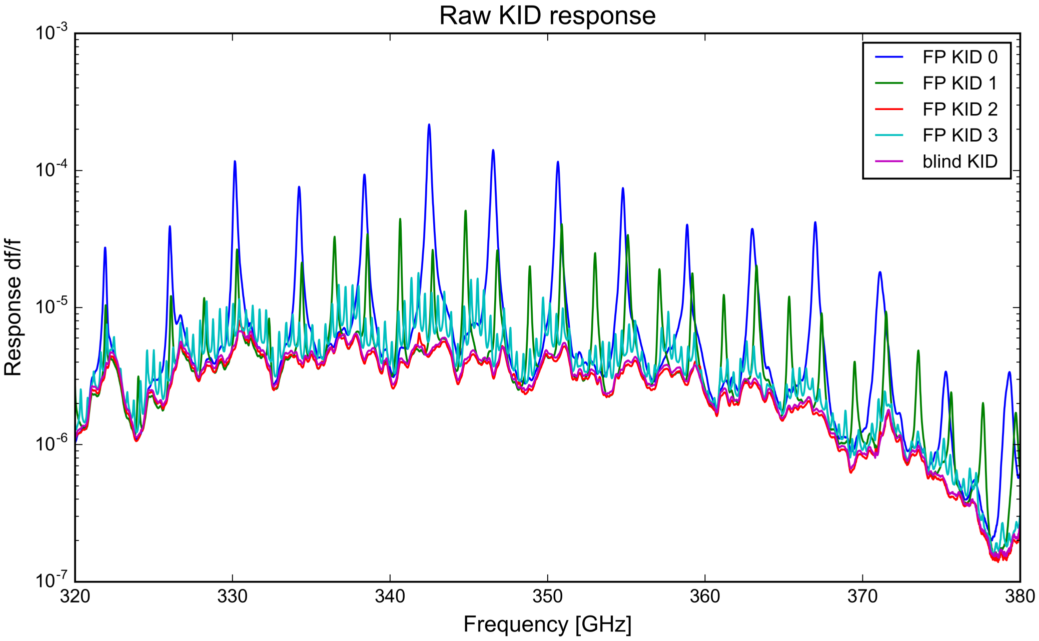

Fig. 10.2: The raw response of the four FP KIDs and the blind KID. For the a-Si experiment the measured frequency range is 320 GHz to 380 GHz with a resolution of 10 MHz. The chip is cooled to 40 mK.

10.2.2. Corrected response

The corrected response for all four kids,

$$Response_{corrected}(f) = \frac{Response_{FP}(f)}{Response_{Blind}(f)}, \tag{10.1}$$

is given in Fig. 10.3. Since the Q_c value increases from FP 1 to FP 3 (Table. 10.3) the relative peak height should decrease from FP 0 to FP 3 as in Fig. 8.7. This is indeed observed for FP 0, FP 1 and FP 3. FP 2, which is expected to show peak height between the height in FP 1 and FP 3, however shows significantly weaker peaks compared to the other FP KIDs. This vastly suppressed peak height is an indication of an additional loss mechanism present in the microstrip FP. As this is only observable in one FP, the most likely explanation is damage to the chip during fabrication. The response from FP 2 is therefore excluded from Q analysis to avoid any impact from unknown loss sources that are not due to the microstrip itself.

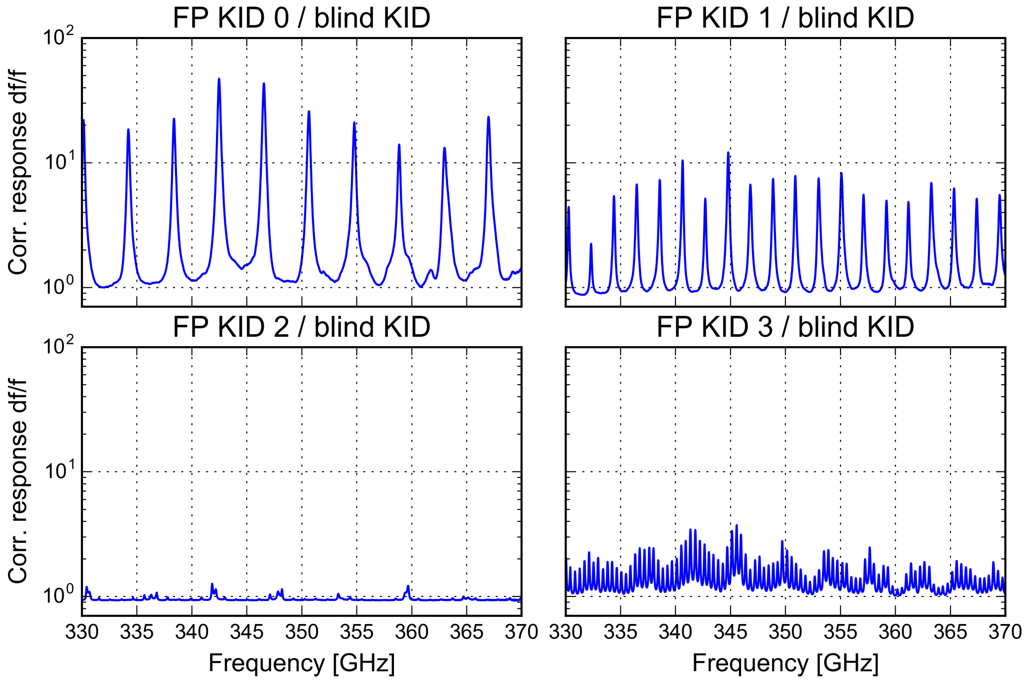

Fig. 10.3: Overview of the response of all four FP KIDs normalised to the response of the blind KID. The minimum and maximum mode number are given in table 10.4

Similar to the polyimide chip (chapter 9.3) there is an additional resonance visible on top of the FP response. A detailed discussion regarding this additional resonance is given in section 9.4. Due to the small frequency spacing f_n between the FP peaks in FP 3 it's response samples this additional resonance.

The expected frequency spacing $f_{corrected}$ is compared with the observed frequency spacing $f_{observed}$ of Fig. 10.3 in Table 10.4. The difference is roughly 10%.

Table 10.4: The corrected expected frequency spacing $f_{corrected}$ vs. the observed frequency spacing $f_{observed}$. The minimum n_{min} and maximum n_{mode} mode number of the peaks between 320 GHz and 380 GHz is given.

KID ID	$\mathbf{f_{0,corrected}}$	$\mathbf{f_{0,observed}}$	$\mathbf{n_{min}}$	$\mathbf{n_{max}}$
FP 0	4.67 GHz	4.10 GHz	78	92
FP 1	2.33 GHz	2.15 GHz	155	183
FP 3	0.47 GHz	0.42 GHz	765	902

10.2.3. Individual peaks

In Fig. 10.4 a single FP peak in the response if FP 0 is plotted for seven different measurement runs with identical measurement settings. There is a slight deviation in the observed peak over the different measurements in peak height and in peak resonance frequency f_n, which can be attributed to fluctuations in toptica output power and frequency stability. Averaging over all peaks, the difference in f_n between measurement runs is $\approx 5MHz$, which is lower than the $10MHz$ relative frequency accuracy guaranteed by the manufacturer. These deviations in peak shape due to the source behaviour lead to a statistical scatter in the fitted Ql across multiple measurements.

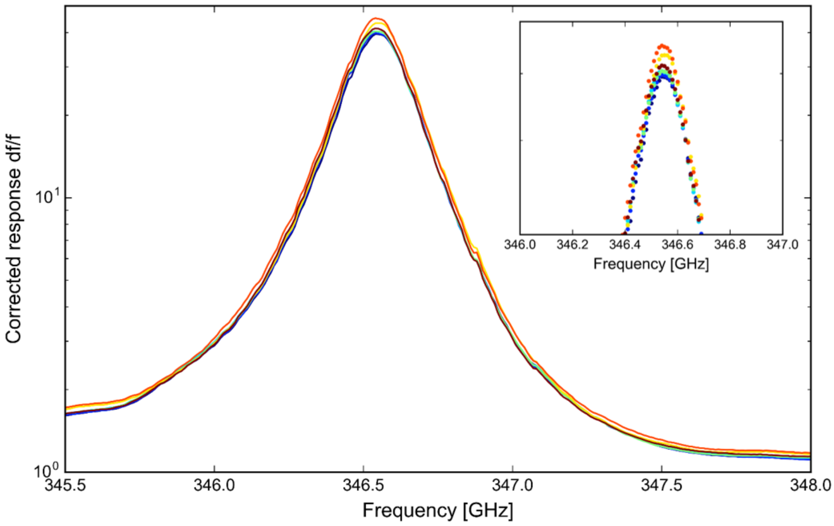

Fig. 10.4: A single FP resonance peak in the response of FP 0 analysed over seven measurement runs with identical measurement settings. The peaks show small deviations between the different measurements.

An overview of the peak fitting to individual peaks is given in Fig. 10.5. Almost all FP peaks in the response of the three FP KIDs can be correctly fitted with a lorentzian peak. The dominant effect which results in wrong fits is the asymmetrical shape of some peaks as seen in Fig. 10.5b, which can be attributed to the impact of the secondary resonance on the FP transmission curve. Due to the asymmetric shape of the peak the fitted lorentzian peak is broadened, resulting in a lower Q_l. FP 0 is affected by this the most, as is expected due to the wider peaks from the lower designed Q_c value (Table 10.3). For FP 0, 4 out of 15 fitted peaks have an asymmetrical shape. For FP 1, 2 out of 26 fitted peaks show a slight asymmetrical shape and for FP 3 none of the 47 fitted peaks show an asymmetrical shape.

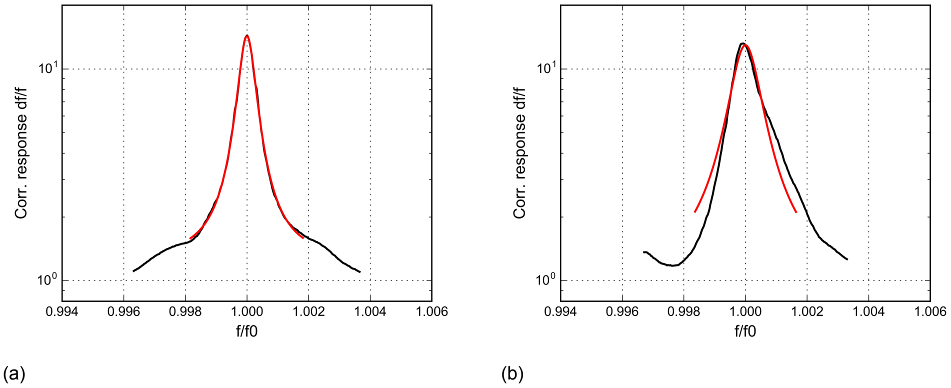

(a) (b)

Fig. 10.5: An overview of Lorentzian fits of the FP peaks in the response of the FP KIDS. FP naming is consistent with table 10.3. **(a)** Good Lorentzian fit of FP 0. **(b)** Bad lorentzian fit of FP 0 due to the asymmetrical nature of the FP peak.

10.2.4. Q values

In Fig. 10.6 the averaged fitted Q_l of all peaks, between 320 GHz to 380 GHz, of seven measurements is plotted. The averaged Q_l for each peak over multiple measurement runs is given as

$$\langle Q_l(f_n) \rangle = \frac{\sum_{m=1}^{M} Q_l(f_n)}{M} \tag{10.2}$$

where M is the total number of measurements. The larger scatter in Q_l for FP 3 is likely due to the small peak width, 200 MHz, which makes the peaks more sensitive to the frequency scatter caused by the frequency uncertainty of the toptica source.

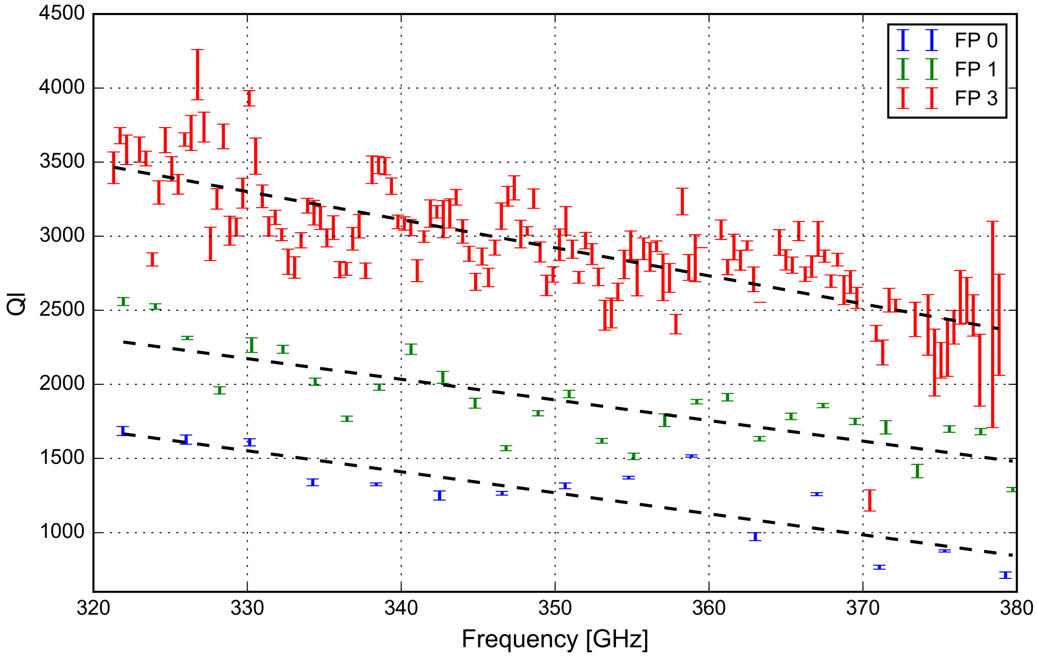

Fig. 10.6: Mean fitted $Q_l(f)$ with standard deviation over seven measurement for each peak. The values of Q_l are plotted against the resonance frequency f_n of the corresponding peaks. A linear fit through Q_l is plotted to show the trend in Q_l vs. frequency. As expected from the simulated Q_c of the coupler and assuming a Q_i constant over frequency, Q_l of the peaks decreases with frequency. The linear fit of Q_l is a first order check and does not represent an assumption on the actual frequency behaviour of Q_l.

Fig. 10.7 shows the fitted Q_l values for the peaks in the response of FP 3. There is a clear relation between the fitted Q_l value and the oscillation in peak height due to the additional resonance. The fitted Q_l value strongly follows the peak height of the FP peaks, i.e. the fitted Q_l decreases when the peak height increases, introducing a similar oscillation in the fitted Q_l Even with this oscillation in Q_l there is a visible trend of decreasing Q_l over frequency.

Using the DC chip and SEM measurements the fabricated couplers can be simulated. The obtained frequency dependent Q_c of the resonators is given in Fig. 10.8. The difference in Q_c values between the FP resonators is due to the difference in frequency spacing f_n and thus mode number between the FP resonators. To obtain the frequency dependent Q_c values of Fig. 10.8 the observed frequency spacing f_n of each resonator is used to calculate the mode number of the peaks (Table 10.4).

With the frequency dependent measured Q_l of Fig. 10.6 and the simulated Q_c of the coupler, the frequency dependent $Q_i(f)$ can be determined as

$$Q_i(f) = FF \frac{Q_c(f) Q_l(f)}{Q_c(f) - Q_l(f)} \tag{10.3}$$

where FF is the fill factor as defined in section 5.2. For the 2 µm wide microstrip on 250 nm of a-Si the fill factor is 67.7%. The obtained $Q_i(f)$ is given in Fig. 10.9.

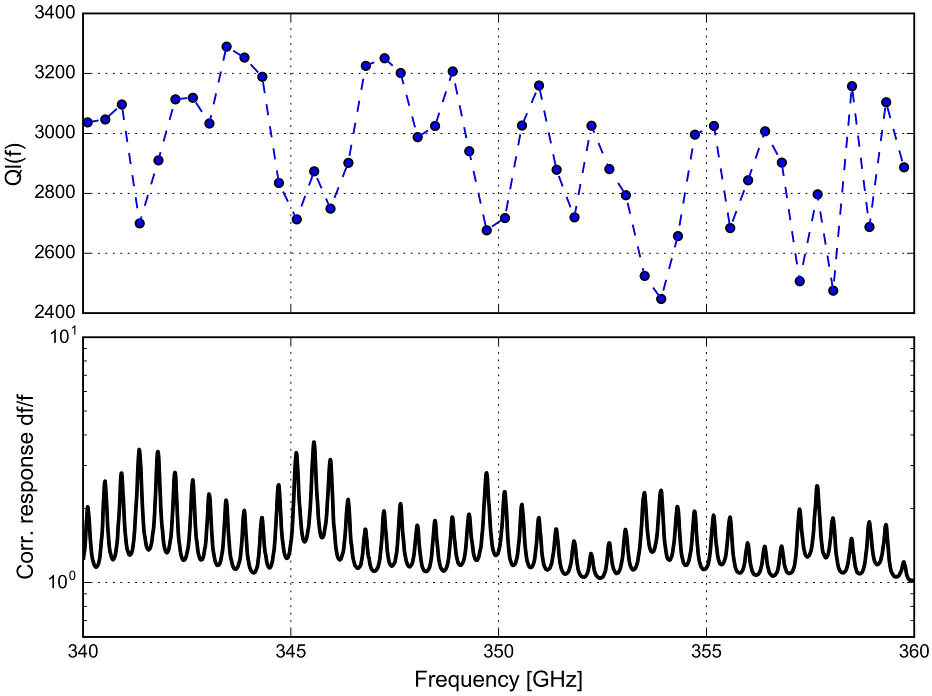

Fig. 10.7: The fitted Q_l values for the FP peaks in the response of FP 3. There is a clear correlation between the change in peak height and the change in fitted Q_l value, i.e. when the peak height peaks the fitted Q_l values of that peak drops. This indicated that the additional resonance, the source of the change in peak height, affects the fitted Q_l values. The dotted line is plotted to make the frequency behaviour of the fitted Q_l clearer.

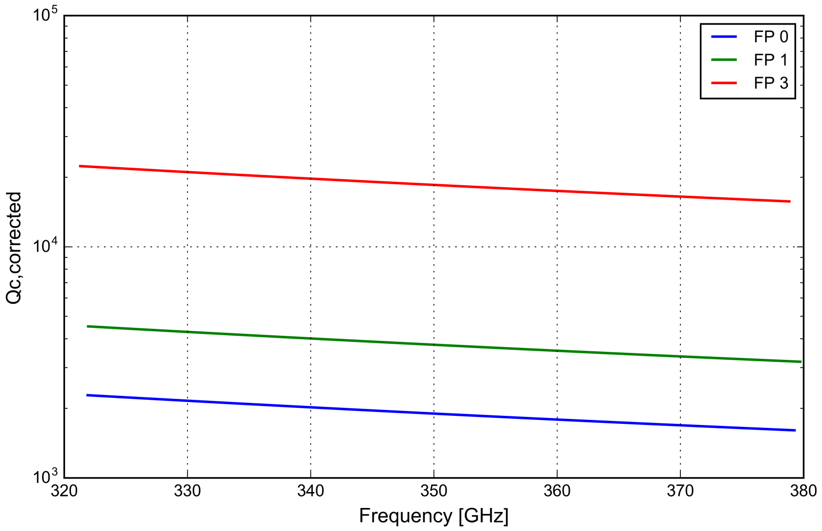

Fig. 10.8: Using the simulated S_{21} of the couplers and the mode number of the FP peaks of each resonator, the frequency dependent $Q_c(f)$ of each FP resonator can be estimated. The difference in Q_c between the different FP resonators is due to the difference in frequency spacing f_n and thus mode numbers of each FP resonator. The $Q_c(f)$ value is an estimate since the radiation losses of the coupler (section 5.2) and the exact film parameters at the coupler are unknown.

For the design of both the a-Si and polyimide chip a constant Q_i over frequency is assumed, however the resulting Q_i is clearly decreasing with frequency. The linear fit of Q_i in Fig. 10.9 is a first order check and does not represent an assumption on the actual frequency behaviour of Q_i. The slope of the linear fit is not consistent across FP KIDs, the slope dQ/df in GHz^{-1} is -43.16 for FP 0, -22.47 for FP 1, and -15.23 for FP 3. This can mean that something is wrong in the analysis, something is wrong with the KID, or the frequency oscillations are hiding the true trend of FP 0.

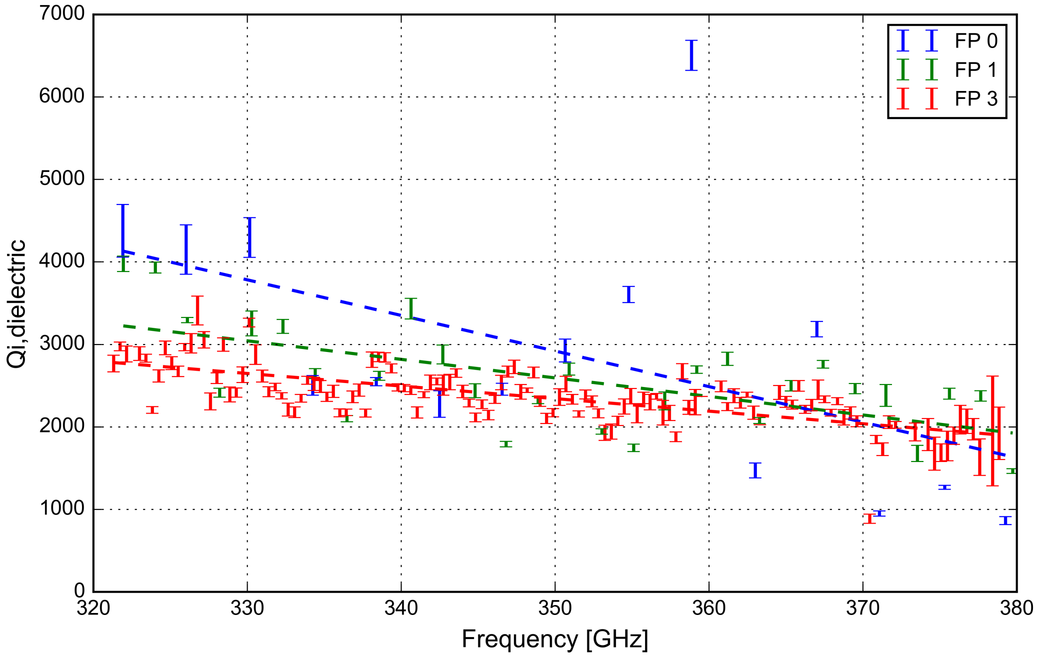

Fig. 10.9: Mean $Q_i(f)$ calculated from the fitted $Q_l(f)$ values of Fig. 10.6 and the corrected Q_c 10.8 for all three FP resonators. The given Q_i values include the fill factor and are thus the Q_i values of the dielectric material and not of the transmission line (section 5.2). The linear fit of Q_i is a first order check and does not represent an assumption on the actual frequency behaviour of Q_i.

10.2.5. Averaged Q_i values

Table 10.5 gives the average Q_i values assuming a frequency constant behaviour. To obtain this value all Q_i of Fig. 10.9 for each FP are averaged using the error bar as the weight.

Table 10.5: The weighted average Q_i, first for each FP assuming constant frequency behaviour (Fig. 10.9) and second over all three FP KIDs. The average is weighted with the error bars of Fig. 10.9

KID ID	**Weighted average Q_i**
FP 0	1535 ± 854
FP 1	2328 ± 608
FP 3	2370 ± 303
Average	2355 ± 101

10.2.6. $Q_l(Q_c,Q_i)$ curve

In Fig. 10.10 the averaged Q_l value for each peak is plotted against the expected Q_c value of that peak. Three lines for different frequency independent Q_i values are plotted using the estimated Q_i of Fig. 10.9. Due to the oscillation in Q_l and the frequency dependency of the measured Q_i the points don't follow the slope of the plotted Q_i lines. Fig. 10.10 does show that the difference in fitted Q_l between FP 0, FP 1, and FP 3 is consistent with the difference in expected Q_c of the FP KIDs for the measured Q_i range.

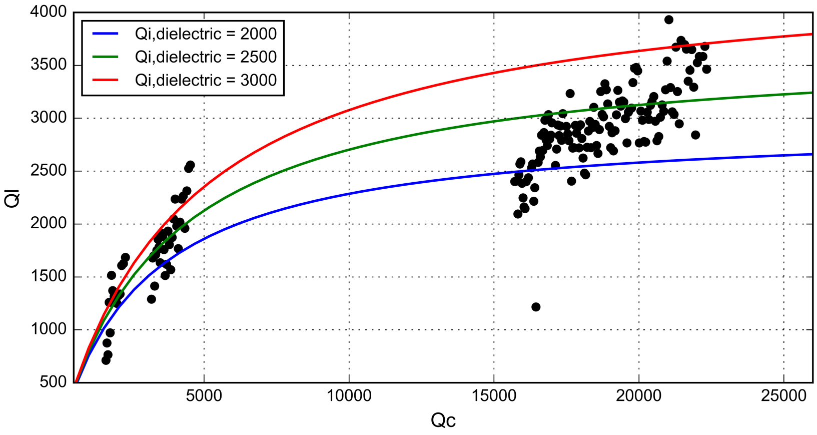

Fig. 10.10: Plotted Q_l vs. Q_c for different values of Q_i. For each resonator the averaged fitted Q_l of each peak averaged over multiple measurements is plotted against the expected Q_c value of that peak. The averaged Q_l is taken over the peaks in the frequency range from 320 GHz to 380 GHz for FP 0 and FP 1 and 320 GHz to 380 GHz for FP 3. Note that the given Q_i is of the dielectric, taking the fill factor of the microstrip geometry, 67.7%, into account.

10.2.7. Full curve

Fig. 10.11 shows a comparison between the modelled curve, using the expected Q_c value (Table 10.3) and estimated $Q_i \approx 2355$ (Table 10.5), and the response of FP 0. The curve is modelled with the ABCD matrix approach (chapter 4) using the two FP couplers, and therefore does not reproduce the oscillations due to the secondary resonance.

The modelled FP response shows that, for these Q values, the expected relative peak height $|S_{21,min}| - |S_{21,max}|$ is higher than the relative peak height observed in the KID response. The difference in relative peak height is likely due to the spurious response, due to which the full curve cannot be measured. This suggest that lowest FP response lies roughly -5dB below the spurious response floor (Fig. 7.8). The peak height oscillation visible in the response of FP 0 is also in the order 5dB. Determining the absolute peak height oscillation and comparing it to a full model of the additional resonance is an interesting avenue to pursue for future analysis, but out of scope for this thesis project.

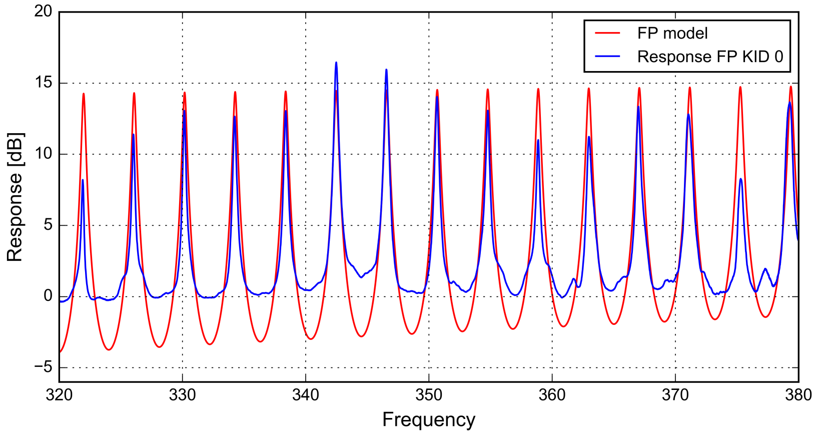

Fig. 10.11: The response of KID 0 together with the modelled FP response. The FP response is modelled for the expected Q_c of 1660 at 350 GHz and the averaged Q_i of 2355.

10.3. Results and discussion

Even without including the secondary resonance in the FP model there is a good match between the modelled FP response, using the measured Q values, and the response of the KIDs. This indicates that the ABCD approach used to model the FP response (chapter 4) is in agreement with the fabricated on-chip FP resonators.

From [16]-[18] a Q_i of $10,000$ is expected for the PECVD deposited a-Si dielectric. Using the a-Si chip a Q_i of approximately $2,000$ to $3,000$ is measured. The difference in expected and measured Q_i can be caused by:

- Poor quality of the NbTiN film. The measured T_c of the NbTiN GND layer is much lower than expected. This indicates a film of poor quality which could introduces additional losses in the transmission line. The measured Q_i might thus be a combination of the losses in the a-Si dielectric and the losses due to the NbTiN film. The losses introduced by the poor NbTiN are frequency dependent, and might explain the frequency dependency of Q_i found in Fig. 10.9. To fully exclude the effect of the poor NbTiN film a new set of chips has to be fabricated with better NbTiN film quality.

- Effect of the deposition and etching steps on the a-Si layer. The a-Si layer might degrade during the deposition and etching of NbTiN on top of the a-Si, which is required to create the microstrip line. Since the CPW line does not include these chips it can be useful to compare the measured Q_i values for a CPW line to those of a microstrip line.

- Deposition of the a-Si layer. It could be that this specific deposited film has inherently high losses. The effects of the deposition method on the losses in the a-Si layer are not fully known. A separate project aimed to study this effect started in parallel to this project. Using the lab-on-chip proposed in this thesis dielectric layers deposited under different deposition conditions will be studied.

The current analysis method is affected by the oscillation in fitted Q_l due to the additional resonant, and by the spurious response floor which makes it impossible to measure the full FP curve. The first makes it difficult to analyse the real frequency behaviour of Q_l, and thus the frequency behaviour of Q_i. The second makes it impossible to fully apply the full curve approach of section 7.5. Through the full curve approach the realised Q_c can be measured instead of being estimated from the realised coupler geometry. The measured Q_c will increase the accuracy of the measured Q_i since the estimated Q_c includes uncertainties on the radiation loss of the coupler and the exact NbTiN film parameters at the coupler. Suggestions on how to reduces the oscillation in Q_c, and how to measure the full curve are included in the recommendation section at the end of this thesis.

11

Conclusion

This thesis gives an overview of the developed design tools for a novel lab-on-chip technique to measure the losses of superconducting microstrip lines at mm-wave frequencies and sub-K temperatures. Using these design tools, two chip sets for measurements of a polyimide and a-Si dielectric have been designed. The measurements and analysis of both designs have been presented, which has proven that the proposed lab-on-chip measurement technique works very well. There is a good match between the measured FP response and the modelled FP response and the measured response follows the expected dependencies on the design parameters, Q_c and the resonator length. In detail, the following requirements were defined:

- The dielectric loss should be measurable at frequencies ranging from 300 GHz to 1.1 THz.
- Dielectrics with an intrinsic loss quality factor ranging from 100 to 10^5. These values originate from the sparse data that exist for polyimide and amorphous silicon. The data that is available for these dielectrics is either measured at room temperature, low frequencies or under specific device conditions [15]-[18].
- The dielectric loss should be measured at sub-K temperatures. DESHIMA and MOSAIC are superconducting detectors which operate at sub-K temperatures, therefore data regarding the dielectric losses are required at sub-K temperatures.
- Suitable for different dielectric materials with different thicknesses and different dielectric constants ε_r.

During the project an attempt was made to measure one of the 650 GHz a-Si chips, however the response of the KIDs did not show a FP behaviour for any of the four FP KIDs. A likely cause for the failure of this chip is the poor quality of one of the NbTiN layers which might cause additional losses in the transmission lines. These losses are frequency dependent which might explain why the chip was not measurable. The 850 GHz a-Si chip was not measured during this project. A new fabrication run and full measurements of the 650 GHz and 850 GHz are required before the performance of the on-chip FP can be analysed at frequencies higher than 350 GHz.

With the polyimide chip a $Q_i \approx 150$ is measured and with the a-Si chip a $Q_i \approx 2355$ is measured. For higher Q_i values the small width of the resulting FP resonance peaks with respect to the Toptica source's frequency uncertainty will introduce a large scatter in the fitted Q_l as for the a-Si chip. Using a different source, with a higher frequency resolution, in the experiment set-up might mitigate this scatter in fitted Q_l. Other than this scatter in fitted Q_l there is currently nothing that suggest a Q_i up to 10^5 cannot be measured with the current on-chip FP and measurement set-up.

The dielectric constant ε_r of polyimide is 2.9 and the layer used for the experiment had a thickness if 1 µm. For the a-Si dielectric this is 10 and 250 nm respectively. Both experiments resulted in measured Q_i values without problems that can be attributed to the dielectric constant or the thickness of the dielectric material. It is thus concluded that the on-chip FP experiment works for dielectric with different dielectric constants and thicknesses. The only problem that was encountered is that the inverted process (section 8.5), where the microstrip line is buried beneath the dielectric layer, does not work for the polyimide dielectric due to resonances inside the coupler. These resonance likely occur due to the lower dielectric constant ε_r of polyimide compared to a-Si.

12

Recommendations

To improve the quality of the on-chip FP experiment the following recommendations, divided per topic, are made:

12.1. Oscillation in FP peak height

The oscillation in FP peak height causes an oscillation in fitted Q_l. Due to this oscillation it is difficult to find the exact frequency dependency of Q_l and Q_i. Reducing the oscillation or the effect of the oscillation thus improves the quality of the experiment:

- The oscillation in FP peak height, observed for both the polyimide and a-Si chip, is likely due to the additional resonance originating from reflections between the antenna-lens system and the first FP coupler. The reflections at the antenna-lens system can be reduced by applying a matching layer on the lenses. Reducing the reflections at the antenna-lens system should decrease the magnitude of the additional resonance and thus the oscillation in FP peak height.
- It is possible that the effect of the additional layer can be removed or reduces by applying appropriate filtering techniques. Investigating these techniques however lies outside the scope of this thesis project. If deemed feasible, it recommended to investigate this option in a separate project.
- Make an attempt to fully model the secondary resonance by including the full antenna-lens system in the ABCD matrix model of the FP and match it with measured data.

12.2. Spurious response floor

Even with the two lens system (section 7.4) the spurious response negatively influenced the a-Si measurements (chapter 10). The measurements can be improved by:

- Applying a matching layer to the lenses of the lens-antenna system will increase the optical efficiency of the measurement set-up and will thus increase the FP response with respect to the spurious response floor (section 7.3).
- An improved two lens system where one of the lenses is placed inside the cryostat close the the FP chip, and the aperture size (section 7.4) is correctly matched to the beam pattern of the lens antenna. This improvement requires significant design and fabrication efforts and could not be completed within the time frame of this thesis.

12.3. Chip improvements

The following improvements to the FP chip can be made:

- Analysis of the pure microstrip KIDs which were present on the a-Si chip. The pure microstrip give a measurement of the dielectric losses at microwave frequencies ($\approx 4 - 7GHz$) which can be compared to the losses measured at THz frequencies with the FP resonators. The microstrip resonators on the a-Si chip however couldn't be measured and this comparison was thus unavailable. It is recommended that the reason the microstrip resonators on the a-Si chip failed is analysed and that the number of pure microstrip resonators on future FP chips is increase.

- The current chips contain a pure NbTiN KID in only one of the two NbTiN layers, and the losses of only one of the NbTiN layers is thus measurable. It is recommended to place a pure NbTiN KID in both NbTiN layers for future FP chips.
- A KID directly coupled to the lens-antenna can be placed to measure and analyse the power coupled from the Toptica source to antenna-lens system.

References

[1] "An illustration of herschel's 40-foot reflecting telescope from charles hutton's a philosophical and mathematical dictionary, 1815." https://www.sciencehistory.org/distillations/a-giant-of-astronomy, accesed: 4-6-2019.

[2] "Karl jansky and his merry-go-round radio telescope," https://public.nrao.edu/gallery/karl-jansky-and-his-merrygoround/, accesed: 4-6-2019.

[3] "Grote reber and his radio telescope," https://www.nrao.edu/whatisra/hist_reber.shtml#gtel, accesed: 4-6-2019.

[4] F. Lacasa, "Non-gaussianity and extragalactic foregrounds to the cosmic microwave background," *arXiv preprint arXiv:1406.0441*, 2014.

[5] "Andromeda galaxy," http://herschel.cf.ac.uk/results/andromeda-galaxy, accesed: 15-5-2019.

[6] "Super star clusters in dust-enshrouded galaxy," http://hubblesite.org/image/1940/news_release/2006-26, accesed: 15-5-2019.

[7] "The 2df galaxy redshift survey," http://www.2dfgrs.net/Public/Survey/index.html, accesed: 15-5-2019.

[8] J. Baselmans, "Multi object spectrometer with an array of superconducting integrated circuits (mosaic)," European Research Council, Research proposal [Part B1]. ERC Consolidator Grant, 2014.

[9] C. A. Balanis, "Measurements of dielectric constants and loss tangents at e-band using a fabry-perot interferometer," January 1970.

[10] A. Endo, P. vanÂ der Werf, R. M. J. Janssen, P. J. de Visser, T. M. Klapwijk, J. J. A. Baselmans, L. Ferrari, A. M. Baryshev, and S. J. C. Yates, "Design of an integrated filterbank for deshima: On-chip submillimeter imaging spectrograph based on superconducting resonators," *Journal of Low Temperature Physics*, vol. 167, no. 3, pp. 341–346, May 2012.

[11] A. Endo, K. Karatsu, Y. Tamura, T. Oshima, A. Taniguchi, T. Takekoshi, S. Asayama, T. J. L. C. Bakx, S. Bosma, J. Bueno, K. W. Chin, Y. Fujii, K. Fujita, R. Huiting, S. Ikarashi, T. Ishida, S. Ishii, R. Kawabe, T. M. Klapwijk, K. Kohno, A. Kouchi, N. Llombart, J. Maekawa, V. Murugesan, S. Nakatsubo, M. Naruse, K. Ohtawara, A. P. Laguna, J. Suzuki, K. Suzuki, D. J. Thoen, T. Tsukagoshi, T. Ueda, P. J. d. Visser, P. P. v. d. Werf, S. J. C. Yates, Y. Yoshimura, O. Yurduseven, and J. J. A. Baselmans, "First light demonstration of the integrated superconducting spectrometer," *Nature Astronomy*, pp. 1–8, 8 2019. [Online]. Available: https://doi.org/10.1038/s41550-019-0850-8

[12] M. Naruse, "Design for high-q filters with narrow cpw lines." Unpublished.

[13] S. Hähnle. In process, 2019.

[14] J. Gao, A. Vayonakis, O. Noroozian, J. Zmuidzinas, P. Day, and H. Leduc, "Measurement of loss in superconducting microstrip at millimeter-wave frequencies," vol. 1185, 12 2009.

[15] *Electric characterization LTC 9300/9500 series*, Fujifilm Electronic Materials, 9 2017.

[16] B. A. Mazin, D. Sank, S. McHugh, E. A. Lucero, A. Merrill, J. Gao, D. Pappas, D. Moore, and J. Zmuidzinas, "Thin film dielectric microstrip kinetic inductance detectors," *Applied Physics Letters*, vol. 96, no. 10, p. 102504, 2010. [Online]. Available: https://doi.org/10.1063/1.3314281

[17] A. Bruno, S. Skacel, C. Kaiser, S. Wuensch, M. Siegel, A. Ustinov, and M. Lisitskiy, “Investigation of dielectric losses in hydrogenated amorphoussilicon (a-si:h) thin films using superconducting microwave resonators,” *Physics Procedia*, vol. 36, pp. 245–249, 12 2012.

[18] A. D. O’Connell, M. Ansmann, R. C. Bialczak, M. Hofheinz, N. Katz, E. Lucero, C. McKenney, M. Neeley, H. Wang, E. M. Weig, A. N. Cleland, and J. M. Martinis, “Microwave dielectric loss at single photon energies and millikelvin temperatures,” *Applied Physics Letters*, vol. 92, no. 11, p. 112903, 2008. [Online]. Available: https://doi.org/10.1063/1.2898887

[19] J. Bardeen, L. N. Cooper, and J. R. Schrieffer, “Theory of superconductivity,” *Phys. Rev.*, vol. 108, pp. 1175–1204, Dec 1957. [Online]. Available: https://link.aps.org/doi/10.1103/PhysRev.108.1175

[20] D. C. Mattis and J. Bardeen, “Theory of the anomalous skin effect in normal and superconducting metals,” *Phys. Rev.*, vol. 111, pp. 412–417, Jul 1958. [Online]. Available: https://link.aps.org/doi/10.1103/PhysRev.111.412

[21] P. J. de Visser, “Quasiparticle dynamics in aluminium superconducting microwave resonators,” Ph.D. dissertation, Technische Universiteit Delft, the Netherlands, 2014.

[22] R. Barends, “Photon-detecting superconducting resonators,” Ph.D. dissertation, Technische Universiteit Delft, the Netherlands, 2009.

[23] J. Gao, J. Zmuidzinas, A. Vayonakis, P. Day, B. Mazin, and H. Leduc, “Equivalence of the effects on the complex conductivity of superconductor due to temperature change and external pair breaking,” *Journal of Low Temperature Physics*, vol. 151, no. 1, pp. 557–563, Apr 2008. [Online]. Available: https://doi.org/10.1007/s10909-007-9688-z

[24] W. Henkels and C. Kircher, “Penetration depth measurements on type ii superconducting films,” *IEEE Transactions on Magnetics*, vol. 13, no. 1, pp. 63–66, January 1977.

[25] R. L. Kautz, “Picosecond pulses on superconducting striplines,” *Journal of Applied Physics*, vol. 49, no. 1, pp. 308–314, 1978. [Online]. Available: https://doi.org/10.1063/1.324387

[26] H. G. Leduc, B. Bumble, P. K. Day, B. H. Eom, J. Gao, S. Golwala, B. A. Mazin, S. McHugh, A. Merrill, D. C. Moore, O. Noroozian, A. D. Turner, and J. Zmuidzinas, “Titanium nitride films for ultrasensitive microresonator detectors,” *Applied Physics Letters*, vol. 97, no. 10, p. 102509, 2010. [Online]. Available: https://doi.org/10.1063/1.3480420

[27] D. Pozar, *Microwave Engineering*. Wiley, 2004, pp. 147–152. [Online]. Available: https://books.google.nl/books?id=4wzpQwAACAAJ

[28] G. Yassin and S. Withington, “Electromagnetic models for superconducting millimetre-wave and sub-millimetre-wave microstrip transmission lines,” *Journal of Physics D: Applied Physics*, vol. 28, no. 9, p. 1983, 1995. [Online]. Available: http://stacks.iop.org/0022-3727/28/i=9/a=028

[29] F. Assadourian and E. Rimai, “Simplified theory of microstrip transmission systems,” *Proceedings of the IRE*, vol. 40, pp. 1651–1657, 1952.

[30] “Sonnet electromagnetic simulation software.” [Online]. Available: http://www.sonnetsoftware.com/

[31] J. Goa, “The physics of superconducting microwave resonators,” Ph.D. dissertation, California Institute of Technology, Pasadena, California, 2008.

[32] D. Pozar, *Microwave Engineering*. Wiley, 2004, pp. 188–193. [Online]. Available: https://books.google.nl/books?id=4wzpQwAACAAJ

[33] M. Y. Frankel, S. Gupta, J. A. Valdmanis, and G. A. Mourou, “Terahertz attenuation and dispersion characteristics of coplanar transmission lines,” *IEEE Transactions on Microwave Theory and Techniques*, vol. 39, no. 6, pp. 910–916, June 1991.

[34] G. Hasnain, A. Dienes, and J. R. Whinnery, “Dispersion of picosecond pulses in coplanar transmission lines,” *IEEE Transactions on Microwave Theory and Techniques*, vol. 34, no. 6, pp. 738–741, Jun 1986.

[35] D. S. Phatak and A. P. Defonzo, “Dispersion characteristics of optically excited coplanar striplines: pulse propagation,” *IEEE Transactions on Microwave Theory and Techniques*, vol. 38, no. 5, pp. 654–661, May 1990.

[36] D. Grischkowsky, I. N. Duling III, J. C. Chen, and C. C. Chi, “Electromagnetic shock waves from transmission lines,” *Phys. Rev. Lett.*, vol. 59, pp. 1663–1666, Oct 1987. [Online]. Available: https://link.aps.org/doi/10.1103/PhysRevLett.59.1663

[37] J. Baselmans, “Kinetic inductance detectors,” *Journal of Low Temperature Physics*, vol. 167, no. 3-4, pp. 292–304, 2012.

[38] B. A. Mazin, “Microwave kinetic inductance detectors: The first decade,” *AIP Conference Proceedings*, vol. 1185, no. 1, pp. 135–142, 2009. [Online]. Available: https://aip.scitation.org/doi/abs/10.1063/1.3292300

[39] B. Mazin, “Microwave kinetic inductance detectors,” Ph.D. dissertation, California Institute of Technology, Pasadena,California, 2004.

[40] R. M. J. Janssen, J. J. A. Baselmans, A. Endo, L. Ferrari, S. J. C. Yates, A. M. Baryshev, and T. M. Klapwijk, “High optical efficiency and photon noise limited sensitivity of microwave kinetic inductance detectors using phase readout,” *Applied Physics Letters*, vol. 103, no. 20, p. 203503, 2013. [Online]. Available: https://doi.org/10.1063/1.4829657

[41] R. Janssen, J. Baselmans, A. Endo, L. Ferrari, S. Yates, A. Baryshev, and T. Klapwijk, “High optical efficiency and photon noise limited sensitivity of microwave kinetic inductance detectors using phase readout,” *Applied Physics Letters*, vol. 103, 11 2013.

[42] J. Gao, M. Daal, J. M. Martinis, A. Vayonakis, J. Zmuidzinas, B. Sadoulet, B. A. Mazin, P. K. Day, and H. G. Leduc, “A semiempirical model for two-level system noise in superconducting microresonators,” *Applied Physics Letters*, vol. 92, no. 21, p. 212504, 2008. [Online]. Available: https://doi.org/10.1063/1.2937855

[43] M. Yahyapour, N. Vieweg, A. Roggenbuck, F. Rettich, O. Cojocari, and A. Deninger, “A flexible phase-insensitive system for broadband cw-terahertz spectroscopy and imaging,” *IEEE Transactions on Terahertz Science and Technology*, vol. 6, no. 5, pp. 670–673, Sep. 2016.

[44] S. Hähnle, J. Bueno, R. Huiting, S. J. C. Yates, and J. J. A. Baselmans, “Large angle optical access in a sub-kelvin cryostat,” *Journal of Low Temperature Physics*, vol. 193, no. 5, pp. 833–840, Dec 2018. [Online]. Available: https://doi.org/10.1007/s10909-018-1940-1

[45] L. Ferrari, O. Yurduseven, N. Llombart, S. J. C. Yates, J. Bueno, V. Murugesan, D. J. Thoen, A. Endo, A. M. Baryshev, and J. J. A. Baselmans, “Antenna coupled mkid performance verification at 850 ghz for large format astrophysics arrays,” *IEEE Transactions on Terahertz Science and Technology*, vol. 8, no. 1, pp. 127–139, Jan 2018.

[46] N. van Marrewijk, “Suppression of radiation loss from superconducting cpws using kinetic inductance.” Unpublished, 2018.

Appendices

A

The scattering (S) matrix

For a N-port network the scattering matrix is given by

$$\begin{bmatrix} V_1^- \\ V_2^- \\ \vdots \\ V_N^- \end{bmatrix} = \begin{bmatrix} S_{11} & S_{12} & \dots & S_{1N} \\ S_{21} & S_{22} & \dots & S_{2N} \\ \vdots & \vdots & \ddots & \vdots \\ S_{N1} & S_{N2} & \dots & S_{NN} \end{bmatrix} \begin{bmatrix} V_1^+ \\ V_2^+ \\ \vdots \\ V_N^+ \end{bmatrix} \tag{A.1}$$

in which the scattering (S) parameters give the relation between the incident (V^+) and reflected (V^-) voltage waves at the ports of the network.

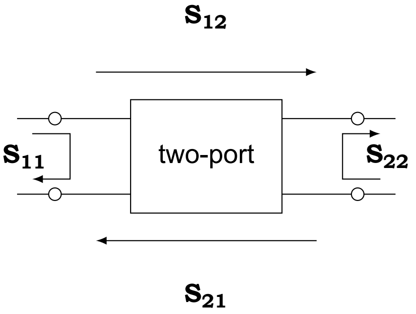

Fig. A.1: Representation of the scattering parameters.

For the two port of Fig. A.1 the scattering matrix is

$$\begin{bmatrix} V_1^- \\ V_2^- \end{bmatrix} = \begin{bmatrix} S_{11} & S_{12} \\ S_{21} & S_{22} \end{bmatrix} \begin{bmatrix} V_1^+ \\ V_2^+ \end{bmatrix} \tag{A.2}$$

where, as an example, S_{11} gives the ratio between the incident and reflected wave at port 1. S_{21} gives the transmission from port 1 to port 2.

For a reciprocal two-port

$$S_{12} = S_{21}. \tag{A.3}$$

The reflected and transmitted power ratios are given by the modulus square of the S parameters, i.e. the fraction of reflected power at port 1 is given by $|S_{11}|^2$.

If the network has an external power input, i.e. an amplifier, it's referred to as an active network. A network without any external power input is referred to as passive. For a passive and lossless two-port the power is either reflected at the input port or transmitted trough the two port and thus

$$|S_{11}|^2 + |S_{12}|^2 = 1 \tag{A.4}$$

and

$$|S_{22}|^2 + |S_{21}|^2 = 1. \tag{A.5}$$

B

The transmission (ABCD) matrix

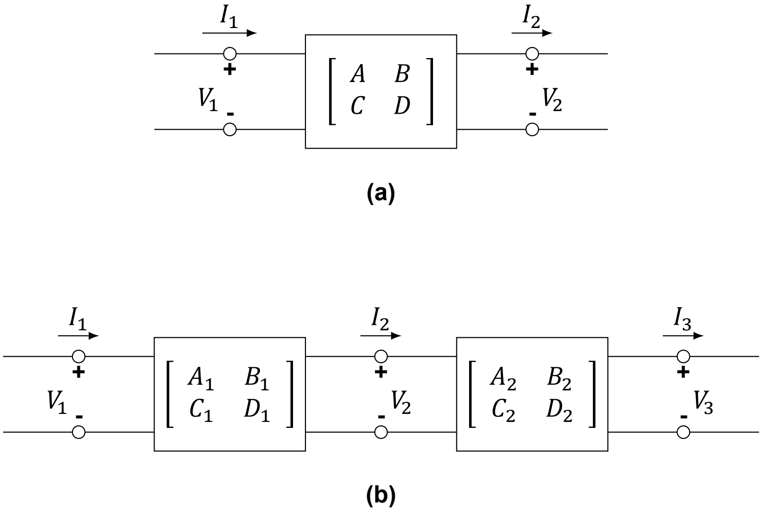
I_1
I_2
V_1
V_2
$\begin{bmatrix} A & B \\ C & D \end{bmatrix}$
(a)
I_1
I_2
I_3
V_1
V_2
V_3
$\begin{bmatrix} A_1 & B_1 \\ C_1 & D_1 \end{bmatrix}$
$\begin{bmatrix} A_2 & B_2 \\ C_2 & D_2 \end{bmatrix}$
(b)

Fig. B.1: **a)** A two-port network. **b)** A cascade connection of two-port networks.

The transmission, or ABCD, matrix defines the relation between voltage and current at the input and output ports defined as in Fig. B.1a

$$\begin{aligned} V_1 &= AV_2 + BI_2 \\ I_1 &= CV_2 + DI_2 \end{aligned} \tag{B.1}$$

The ABCD parameters are typically given in matrix form

$$\begin{bmatrix} V_1 \\ I_1 \end{bmatrix} = \begin{bmatrix} A & B \\ C & D \end{bmatrix} \begin{bmatrix} V_2 \\ I_2 \end{bmatrix} \tag{B.2}$$

The advantage of using ABCD matrices to describe networks is that the ABCD matrix of a cascade of two-port networks is given by the product of the ABCD matrices of the individual two-port networks. The ABCD matrix of the cascade given in Fig. B.1b is then

$$\begin{bmatrix} V_1 \\ I_1 \end{bmatrix} = \begin{bmatrix} A_1 & B_1 \\ C_1 & D_1 \end{bmatrix} \begin{bmatrix} A_2 & B_2 \\ C_2 & D_2 \end{bmatrix} \begin{bmatrix} V_3 \\ I_3 \end{bmatrix} \tag{B.3}$$

The ABCD parameters of a two port can be evaluated as

$$\begin{array}{ll} A = \left.\dfrac{V_1}{V_2}\right|_{I_2=0} & B = \left.\dfrac{V_1}{I_2}\right|_{V_2=0} \\ C = \left.\dfrac{I_1}{V_2}\right|_{I_2=0} & D = \left.\dfrac{I_1}{I_2}\right|_{V_2=0} \end{array} \tag{B.4}$$

where $I_2 = 0$ is equivalent to an open port and $V_2 = 0$ to a shorted port. The ABCD parameters of some commonly used two-port networks are given in Table. B.1.

Table B.1: ABCD of commonly used two-port circuits. $\gamma = \alpha + j\beta$

Circuit	**ABCD Parameters**	
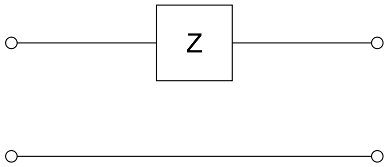	$A = 1$ $C = 0$	$B = Z$ $D = 1$
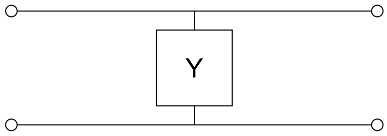	$A = 1$ $C = Y$	$B = 0$ $D = 1$
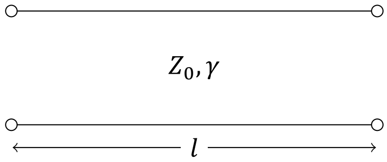	$A = \cosh(\gamma l)$ $C = Y_0 \sinh(\gamma l)$	$B = Z_0 \sinh(\gamma l)$ $D = \cosh(\gamma l)$

C

Conversion between S and ABCD parameters

Table C.1: Conversion between ABCD and S parameters. $\mathbf{Z_{01}}$ is the impedance of the source. $\mathbf{Z_{02}}$ is the impedance of the load.

ABCD to S
$S_{11} = \frac{AZ_{02}+B-CZ_{01}^{*}Z_{02}-DZ_{01}^{*}}{AZ_{02}+B+CZ_{01}Z_{02}+DZ_{01}}$
$S_{12} = \frac{2(AD-BC)(R_{01}R_{02})^{1/2}}{AZ_{02}+B+CZ_{01}Z_{02}+DZ_{01}}$
$S_{21} = \frac{2(R_{01}R_{02})^{1/2})}{AZ_{02}+B+CZ_{01}Z_{02}+DZ_{01}}$
$S_{22} = \frac{-AZ_{02}^{*}+B-CZ_{01}Z_{02}^{*}+DZ_{01}^{*}}{AZ_{02}+B+CZ_{01}Z_{02}+DZ_{01}}$

S to ABCD
$A = \frac{(Z_{01}^{*}+S_{11}Z_{01})(1-S_{22})+S_{12}S_{21}Z_{01}}{2S_{21}(R_{01}R_{02})^{1/2}}$
$B = \frac{(Z_{01}^{*}+S_{11}Z_{01})(Z_{02}^{*}+S_{22}Z_{02})-S_{12}S_{21}Z_{01}Z_{02}}{2S_{21}(R_{01}R_{02})^{1/2}}$
$C = \frac{(1-S_{11})(1-S_{22})-S_{12}S_{21}}{2S_{21}(R_{01}R_{02})^{1/2}}$
$D = \frac{(1-S_{11})(Z_{02}^{*}+S_{22}Z_{02})-S_{12}S_{21}Z_{02}}{2S_{21}(R_{01}R_{02})^{1/2}}$

D

Unmeasured devices

D.1. PI chip design for Q_c = 20,000

Table D.1: Overview of the CPW FP and coupler parameters for the bare CPW and the CPW covered with a ployimide (PI) layer. Coupler dimensions are given as in Fig. 8.2.

	$\mathbf{l_{resonator}}$	$\mathbf{f_0}$	$\mathbf{l_1}$	$\mathbf{l_2}$
Bare $Q_c = 20.000$	5 mm	8.0 GHz	6.0 µm	6.0 µm
PI $Q_c = 20.000$	5 mm	7.7 GHz	6.0 µm	6.0 µm

Table D.2: Overview of the CPW to microstrip coupler geometries . Coupler dimensions are given as in Fig. 8.3.

	$\mathbf{l_{resonator}}$	$\mathbf{f_0}$	$\mathbf{l_{overlap}}$
$Q_c = 20.000$	7 mm	7.9 GHz	17.7 µm

D.2. Amorphous silicon chip design for 650 and 850 GHz

Table D.3: Overview of the microstrip FP resonator design for the a-Si experiment. Each frequency band f is a different chip with four resonators. Coupler dimensions are given as in Fig. 8.3.

$\mathbf{f}$	$\mathbf{Q_c}$	$\mathbf{l_{resonator}}$	$\mathbf{f_n}$	$\mathbf{l_{overlap}}$
600 - 700	3.000	2.0 mm	10.96 GHz	8.0 µm
	$6,000$	4.0 mm	5.48 GHz	8.0 µm
	$12,000$	8.0 mm	2.74 GHz	8.0 µm
	$30,000$	20.0 mm	1.10 GHz	8.0 µm
800 - 900	$3,000$	1.5 mm	14.61 GHz	5.0 µm
	$6,000$	3.0 mm	7.31 GHz	5.0 µm
	$12,000$	6.0 mm	3.65 GHz	5.0 µm
	$30,000$	15.0 mm	1.46 GHz	5.0 µm

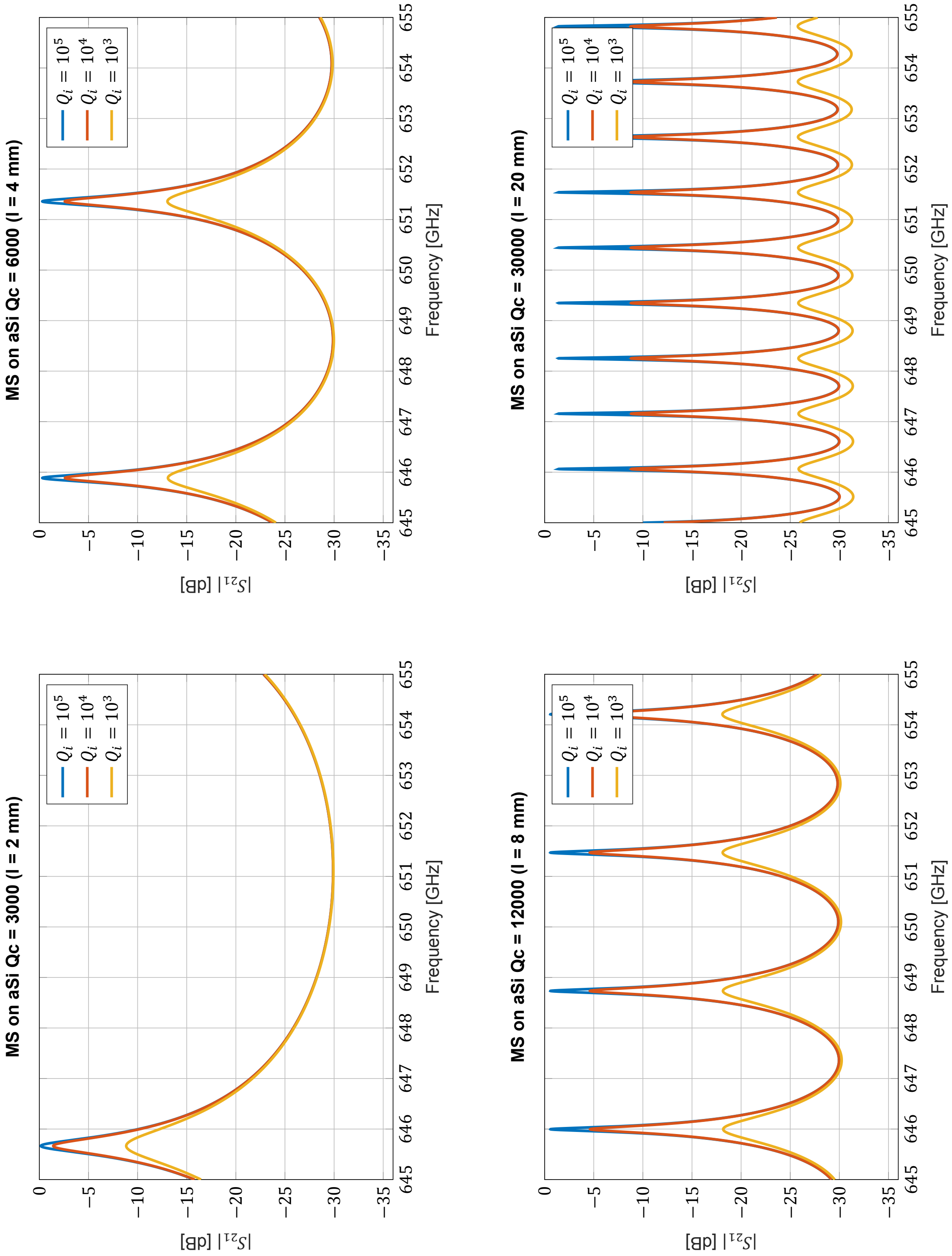

Fig. D.1: Resonance curves for the 600-700 GHz microstrip FP resonator.

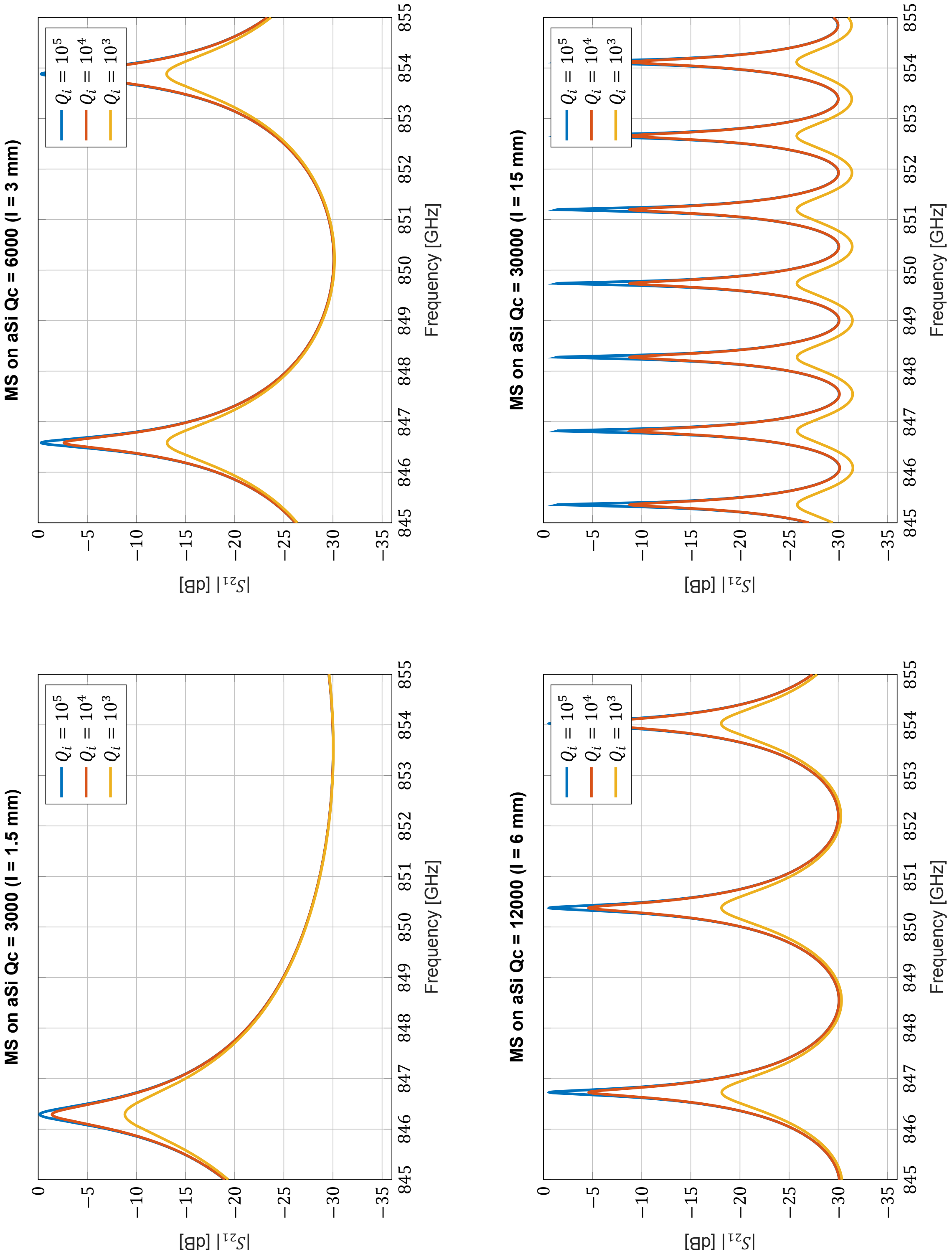

Fig. D.2: Resonance curves for the 800-900 GHz microstrip FP resonator.